

Movements of Molecular Motors: Diffusion and Directed Walks

Dissertation

zur Erlangung des akademischen Grades
Doktor der Naturwissenschaften (Dr. rer. nat.)
in der Wissenschaftsdisziplin Theoretische Physik

eingereicht an der
Mathematisch-Naturwissenschaftlichen Fakultät der Universität Potsdam

angefertigt am
Max-Planck-Institut für Kolloid- und Grenzflächenforschung in Golm

von

Stefan Klumpp

geboren am 29. September 1973 in Waiblingen

Potsdam, im April 2003

Zusammenfassung

Bewegungen von prozessiven molekularen Motoren des Zytoskeletts sind durch ein Wechselspiel von gerichteter Bewegung entlang von Filamenten und Diffusion in der umgebenden Lösung gekennzeichnet. Diese eigentümlichen Bewegungen werden in der vorliegenden Arbeit untersucht, indem sie als Random Walks auf einem Gitter modelliert werden. Ein weiterer Gegenstand der Untersuchung sind Effekte von Wechselwirkungen zwischen den Motoren auf diese Bewegungen.

Im einzelnen werden vier Transportphänomene untersucht: (i) Random Walks von einzelnen Motoren in Kompartimenten verschiedener Geometrien, (ii) stationäre Konzentrationsprofile, die sich in geschlossenen Kompartimenten infolge dieser Bewegungen einstellen, (iii) randinduzierte Phasenübergänge in offenen röhrenartigen Kompartimenten, die an Motorenreservoirs gekoppelt sind, und (iv) der Einfluß von kooperativen Effekten bei der Motor-Filament-Bindung auf die Bewegung. Alle diese Phänomene sind experimentell zugänglich, und mögliche experimentelle Realisierungen werden diskutiert.

Abstract

Movements of processive cytoskeletal motors are characterized by an interplay between directed motion along filament and diffusion in the surrounding solution. In the present work, these peculiar movements are studied by modeling them as random walks on a lattice. An additional subject of our studies is the effect of motor-motor interactions on these movements.

In detail, four transport phenomena are studied: (i) Random walks of single motors in compartments of various geometries, (ii) stationary concentration profiles which build up as a result of these movements in closed compartments, (iii) boundary-induced phase transitions in open tube-like compartments coupled to reservoirs of motors, and (iv) the influence of cooperative effects in motor-filament binding on the movements. All these phenomena are experimentally accessible and possible experimental realizations are discussed.

Contents

1	Introduction	1
1.1	Brownian Motion	1
1.2	Molecular motors	3
1.2.1	Recent experimental developments	5
1.2.2	Modeling — separation of scales	5
1.2.3	Bound and unbound movements	7
1.3	Overview	8
2	Lattice models for the walks of molecular motors	9
2.1	Lattice models	9
2.1.1	Basic lattice model	10
2.1.2	Master equations	11
2.1.3	Mapping parameters of motion to the hopping rates	12
2.1.4	Modified lattice model	12
2.2	General features of the models	14
2.3	Interacting motors	15
2.4	Continuum equations	16
2.5	Two-state approximation	17
2.6	Summary	18
3	Random walks of single motors in open compartments	19
3.1	Anomalous drift: Scaling arguments and simulations	19
3.2	Analytical solution in two and three dimensions	22
3.2.1	The two-dimensional case	23
3.2.2	The three-dimensional case	27
3.2.3	Sticking probability	28
3.3	Return to the filament and asymptotic displacement	30
3.4	Continuum model and open compartments	31
3.4.1	The two-dimensional case	31
3.4.2	The three-dimensional case	32
3.4.3	Open compartments	33
3.5	Effective diffusion coefficient	37
3.6	Arrays of parallel filaments	37
3.7	Summary	38

4	Concentration profiles in closed compartments	39
4.1	Density profile in a closed tube	39
4.2	Two-state approximation	43
4.2.1	Continuous two-state equations	43
4.2.2	Discrete model	47
4.3	Depletion layer	49
4.4	Some modifications of the model	51
4.5	Density profiles in asters	53
4.5.1	Two-state equations	53
4.5.2	Numerical results	55
4.6	Summary	56
5	Motor traffic through open tube-like compartments	59
5.1	Open tube systems	59
5.2	Periodic boundary conditions	61
5.3	Open boundaries with radial equilibrium	63
5.3.1	Phase diagram	63
5.3.2	Density profiles	66
5.4	Diffusive injection and extraction of motors	72
5.4.1	Diffusive bottlenecks	72
5.4.2	Phase diagrams with and without maximal current phase	73
5.4.3	Active versus thermal unbinding from the 'last' filament site	75
5.5	Summary	76
6	Motors with attractive interactions	77
6.1	Interactions of motors	77
6.2	Attractive interactions	78
6.3	Two species of motors	80
6.3.1	Two kinds of phase transitions	81
6.3.2	Mean field theory	85
6.3.3	General remarks and extensions	88
6.4	Summary	89
7	Conclusions and outlook	91
	Appendix	95
A	Details of the computer simulations	97
B	Theory of random walks	99
B.1	Random walks on homogeneous cubic lattices	99
B.2	Return to the origin	100
B.3	Tauberian theorems	101
B.4	Integrals for the random walks of molecular motors	102
C	Several motors transporting one cargo	103

D More about motor traffic in tube-like compartments	105
D.1 Radial equilibrium for periodic boundary conditions	105
D.2 Discrete mean field theory for open boundaries with radial equilibrium	106
D.3 Diffusive injection and extraction of motor particles: The one-dimensional case	110
List of symbols	111
Bibliography	115
Acknowledgments	123

Chapter 1

Introduction

Movement is one of the signatures of life and can be found on various length scales in the living world, from motion of whole organisms to movements of single biomolecules. In the following we will study movements of biomolecules within the cell or *in vitro*. There are two fundamentally distinct kinds of movements of biomolecules, organelles and cells: passive diffusion or Brownian motion and active motion powered by chemical free energy. Brownian motion affects every sufficiently small particle and is ubiquitous in biological systems [1]. In contrast, active motion depends on specific molecules, called molecular motors, which are able to convert chemical free energy into movement or mechanical work [2, 3].

In the following chapters, we will focus on processive cytoskeletal motors. These motors move unidirectionally along filaments of the cytoskeleton, hydrolyzing the fuel molecule adenosine triphosphate (ATP) and converting the released free energy into directed motion. The best studied examples are kinesins, which walk along microtubules, and certain types of myosins, which move along actin filaments. In the cell, these motors are involved in transport of vesicles and segregation of chromosomes.

In addition to the distinction between active and passive movements, these movements can further be classified according to their dimensionality, i.e. whether they occur in three-dimensional space, on two-dimensional surfaces, or along one-dimensional lines. The latter cases are relevant for particles that can bind to a surface or line, in which case their movements are restricted to these low-dimensional manifolds. In principle, both active and passive movements are possible in all three cases. Cytoskeletal motors thus perform active movement along one-dimensional filaments.

However, if such a motor is observed over a sufficiently long time, it will detach from its filamentous track, since its binding energy can be overcome by thermal fluctuations. The unbound motor then performs passive diffusion in the surrounding fluid, until it eventually reattaches to the same or another filament. This *interplay between directed active movement along filaments and free diffusion* will be the central subject of the following chapters, where we will discuss several transport phenomena related to this combined type of motion. In the remaining sections of this introduction, we will introduce the molecular motors and their passive and active movements in more detail and give an overview of the following chapters.

1.1 Brownian Motion

In 1828 Robert Brown observed that small particles extracted from pollen of various plants performed erratic movements in water. He first thought that he had observed self-animated

particles or "active molecules" [4], which at that time were believed by some biologists to be the constituents of organic bodies. Motion of these self-animated active particles was believed to be driven by a kind of internal living force specific for the organic world. During his further studies, however, Brown realized that particles which moved, when they were suspended in water, could be obtained from almost every substance, from dried plants and vegetable products to various kinds of minerals. Hence, contrary to his first conjecture, his observations showed that Brownian motion is a generic physical phenomenon rather than a biological one [5].

It was soon proposed that Brownian motion is related to heat, since it is affected by temperature changes [5], but quantitative explanations of the phenomenon failed until the works of Einstein [6] and Smoluchowsky [7] at the beginning of the 20th century. The crucial point of the explanation is the identification of these movements as fluctuation phenomena: while the random collisions with the thermally moving particles of the surrounding fluid do not cause motion on average, the fluctuations due to these collisions are visible. The variance of the position of the Brownian particle rather than its average position increases linearly with time. This linear behaviour is governed by the diffusion coefficient D , which is given by the famous Stokes–Einstein relation [1],

$$D = \frac{k_B T}{6\pi\eta R_{\text{hyd}}}. \quad (1.1)$$

It depends on the thermal energy $k_B T$, the viscosity η of the fluid and the effective hydrodynamic radius R_{hyd} of the Brownian particle.

Since a Brownian particle explores the whole accessible space, reduction of the dimensionality can enhance diffusion-driven processes such as collisions of Brownian particles or diffusion-controlled chemical reactions [8]. In biological systems, reduction of the dimensionality occurs if the Brownian particle binds to a surface such as the membrane of a cell or to one-dimensional objects such as cytoskeletal filaments or DNA, so that its motion is restricted to directions along these manifolds. In the specific case of biomolecules diffusing along a filament, this type of motion is called '*sliding*' and has been discussed extensively in the context of proteins binding to DNA [9,10]. It has been directly observed in *in vitro* experiments for the cases of RNA polymerase sliding along DNA [11] and for cytoskeletal motors sliding along microtubules in the absence of the fuel molecule ATP [12].

While the concept of a living force has been abandoned, active particles have found their way back into biology: As mentioned, many kinds of motion occurring in a living cell are active movements in the sense that they are driven by specific molecular motors. These motors, however, are now understood to be nanometer-sized chemo-mechanical machines rather than particles possessing a living force [3]. They convert the chemical energy of fuel molecules into motion, just like their macroscopic counterparts. The difference in size, however, implies a conceptual difference as well: energies of macroscopic engines are usually very large compared to the thermal energy $k_B T$, while the typical energy scale for a molecular motor is only a few $k_B T$ at room temperature or under physiological conditions. A molecular motor therefore necessarily has to cope with thermal fluctuations as a permanent source of perturbations and some molecular motors might even use thermal fluctuations to generate motion by rectifying the diffusive sliding along their track.¹

¹Rectification of diffusion by conformational changes of a motor (the so-called ratchet effect or Brownian motor mechanism) has been studied extensively during the last decade (see the review [13]) and can be used

1.2 Molecular motors

As mentioned, many transport processes in living cells are driven by specific motor molecules which convert chemical energy into movement and perform mechanical work. These active transport processes maintain the complex order of the cell and keep the cell's state far from equilibrium.

As in the case of macroscopic machines, different functions require different motors. According to their functions in the cell, these motors can be grouped into several classes: (i) rotary motors like F_1 -ATPase, which synthesizes ATP, and the bacterial flagella, which powers swimming of bacteria; (ii) membrane pumps, which maintain concentration gradients of certain ions or small molecules across membranes; (iii) contractile systems, which are assemblies of large numbers of motor molecules working together, e.g. myosins in muscle or dyneins that drive beating of cilia and sperm; finally there are motors processing along a linear track, which can be further classified according to the type of track: (iv) motors moving along DNA or RNA (e.g. RNA polymerase), which are involved in processing of the genetic information and (v) cytoskeletal motors moving along filaments of the cytoskeleton.

In addition, these motors vary in size, from single molecules to large complexes, and in the type of fuel they consume. Even within each class there are many different species of motors, e.g., the total number of different types of linear motors in a eukaryotic cell might be 50–100 [17].

In the following, we focus on *processive cytoskeletal motors*, which can move unidirectionally along cytoskeletal filaments over relatively large distances. These motors can be divided into three motor families, myosins, kinesins, and dyneins. Myosins move along actin filaments, while kinesins and dyneins move along microtubules. Note, however, that all three families contain both processive and non-processive members, which are adapted to different functions in the cell. The best studied type of myosin, muscle myosin (myosin II), is non-processive, it drives the contraction of muscles by cooperation in large groups of 10^6 – 10^9 motor molecules. On the other hand, other types of myosin such as myosin V have been shown to be processive and are involved in transport of vesicles. Kinesins are usually processive, as they are responsible for transport of vesicles, chromosomes and other cargoes over large distances, but some family members need to work in small groups, see Ref. [3]. Similarly, there are processive and non-processive dyneins.

The motors of all three classes hydrolyze adenosine triphosphate (ATP) and convert the released free energy into motion through a series of conformational changes in their actual motor domain.

The tracks along which these motors move, microtubules and actin filaments, are long semi-flexible biopolymers. A typical length of a microtubule is tens of micrometers, its diameter is 25 nm. Microtubules consist of (usually) 13 protofilaments, parallel tracks along which motors can move. Motors bind to specific binding sites, located regularly along the protofilaments with a longitudinal repeat distance of 8 nm. As the measured step size of kinesin motors is also 8 nm, this means that kinesin motors step from one binding site to the next one. Similarly, actin filaments have a repeat distance of 36 nm, which corresponds to the step size of the actin-based processive motor myosin V. Actin filaments are similar to microtubules in length,

for the construction of separation devices, e.g. [14]. It has been proposed as the processivity mechanism of monomeric kinesin motors, which exhibit small drift and large diffusion [15]. A recent study however indicates that these monomeric motors might dimerize under *in vivo* conditions and then work by a (more efficient) mechanism that does not rely on diffusion [16].

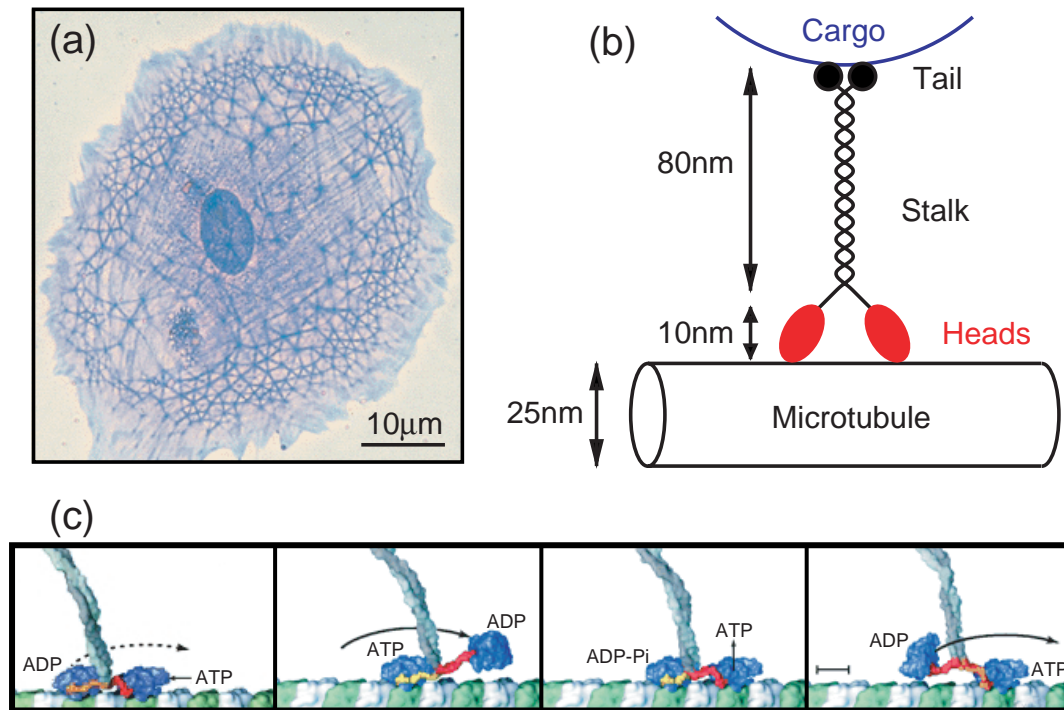


Figure 1.1: (a) The cytoskeleton is a network of biopolymers; from [2]. (b) A schematic picture of the motor protein kinesin which moves along a microtubule. (c) A molecular model for the step of kinesin; from [18].

but more flexible. In the cell these filaments form a dynamic network, the cytoskeleton, see Fig. 1.1(a). Apart from being a transportation system, the cytoskeleton has several functions such as giving the cell its mechanical stability and shape.

As an example, let us now focus on (conventional) kinesin [19], which is probably the best studied processive motor. However, other motors seem to work in a similar way [3]. Conventional kinesin is an elongated dimeric molecule, see Fig. 1.1(b). It consists of two globular head domains, which join in a neck region and are connected to a tail through an elongated coiled coil domain, the so-called stalk. The size of the heads is about 10 nm, a typical length of the stalk+tail region is 80 nm. The heads are the actual motor domains and contain both the binding sites for ATP (the fuel) and for microtubules (the track). On the other hand, the tail is responsible for binding the cargo. While the motor domain is widely conserved throughout the kinesin family (and even very similar to the myosin motor domain), the tails are adapted to specific cargoes. ATP hydrolysis in the two heads is coordinated and the kinesin molecule is thought to perform a kind of walking or 'hand-over-hand' movement, advancing one head in front of the other, which remains bound to the microtubule track to prevent the molecule from detaching.² According to this mechanism, a conformational change in the front head, induced by ATP binding to this head is amplified by the neck region to throw forward the rear head [18], see Fig. 1.1(c).

²While there is considerable evidence for coordinated motion of the heads [20–22], recent experiments seem to be inconsistent with the hand-over-hand mechanism and to support inchworm-like motion [23].

In this way, a single kinesin molecule can move cargoes such as vesicles or latex beads over large distances. A typical walking distance for a single kinesin molecule is $1\ \mu\text{m}$ or about 100 steps. This means that per step, there is a probability of about 1% that the kinesin–microtubule binding energy is overcome by thermal fluctuations. In this case, the motor (including its cargo) unbinds from the microtubule and explores the available volume by diffusion, until it rebinds to another or the same microtubule.

1.2.1 Recent experimental developments

During the last 15 years, cytoskeletal motors have attracted more and more interest. On the one hand, the atomic structure of many motors has been resolved by X-ray crystallography, e.g. for myosin and kinesin, which provides a structural basis for the understanding of the mechanism of the chemo-mechanical coupling, see chapter 12 of Ref. [3]. On the other hand, single-molecule experiments have been developed, by which one can measure transport properties of the motors such as velocity, force exerted, step size, walking distance etc., see Ref. [24] and chapter 15 of Ref. [3]. These transport properties have been measured for various types of motors including dimeric kinesin [25–30], the processive monomeric kinesin KIF1A [15], myosin V [31, 32] and dynein [33–35] as well as for some of their non-processive relatives, see Ref. [3].

Two types of experimental setups are used for measurements of transport properties: (i) Motors are attached to a surface and the motion of filaments driven by these motors is observed (filament gliding assay), or (ii) the filaments are immobilized to the substrate and motors moving along these filaments are observed by tracking their cargo, usually latex beads (bead assay). If the density of motors attached to the bead (or, in the alternative approach, to the planar substrate) is sufficiently low, transport powered by single motor molecules can be achieved. Velocities and diffusion coefficients can then be determined by tracking the motion of the beads. Trapping the bead, e.g. with optical tweezers, allows one to measure forces and to resolve single step displacements.

In addition, several attempts have been made to use biological motors in nanotechnological transport systems. Again, both basic setups are used. In one approach, tracks covered with kinesin molecules are produced on a patterned substrate and short pieces of microtubules are used as wagons, which can be loaded by a cargo [36, 37]. In the complementary approach, microtubules are fixed to a surface and kinesin-coated cargoes are transported along these tracks [38–40]. An important step towards such kinesin-powered transport systems is the development of methods to align many microtubules in parallel with isopolar orientation [39, 40]. If small cargoes are transported (by a single motor or a few motors) over large distances, traffic in these systems will again be affected by detachment of motors from the microtubules.³

1.2.2 Modeling — separation of scales

Movements of molecular motors involve three time regimes, which can be separated and modeled independently of each other [41]: (I) the molecular dynamics underlying the chemo-mechanical coupling and leading to a single step of step size $\sim 10\ \text{nm}$ and stepping time $\sim 10\ \text{ms}$; (II) the directed walks along a filament with typical walking distances of $\sim 1\ \mu\text{m}$ and walking times of $\sim 1\ \text{s}$; and (III) the random walks consisting of many cycles of attachment

³In the experiments reported in Refs. [38, 40] cargoes are rather large and transport is performed by the simultaneous action of many motors, so that complete detachment is very unlikely, see also appendix C.

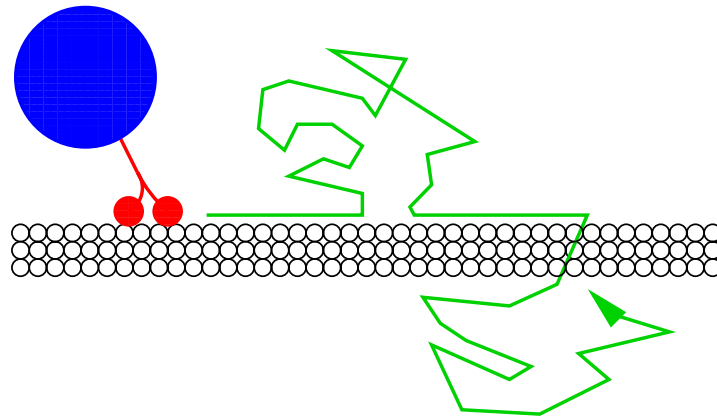


Figure 1.2: Random walks of molecular motors consist of alternating periods of directed motion along filaments and diffusion.

to and detachment from filaments, see Fig. 1.2. In the following chapters, we will present a theoretical approach to the long-time regime (III) and discuss several transport phenomena related to this regime. We will also show how the phenomena of regime (III) are related to the transport properties of the directed walks of regime (II).

The long-time regime (III) applies both to intracellular transport, where motors move over tens of micrometers or even tens of centimeters in the case of transport in axons [42], and to biomimetic transport systems, where biological motors are used to transport non-biological cargoes over similar distances, as reviewed in more detail above.

Most previous modeling approaches to molecular motors address the intermediate regime (II), where various approaches have been used, see e.g. [43–49]. Using specific models for specific motors, good agreement with experiments is obtained for the dependence of transport properties of the walks along filaments like the velocity, the diffusion coefficient and the walking distance on control parameters such as the ATP concentration or the applied load force [50–52]. On the other hand, using general schemes allows one to identify generic properties of these walks [53, 54]. In particular, a generic relationship can be derived for the dependence of the motor velocity on ATP concentration and load force [53].

The long-time regime (III) has, apart from one article by Ajdari [55], only been addressed rather recently by our work [56–58]. In Ref. [55], the random walks of single motors arising from many diffusive encounters with filaments are discussed for the case of unbounded geometries using scaling arguments. For these random walks, we have obtained analytical and numerical results for movements in both unbounded geometries and various bounded compartments [56, 57], which are presented in chapter 3.

A different field, which is related to regime (III) and which has attracted much interest in recent years, is the formation of the dynamic and highly ordered structures of the cytoskeleton, where transport by motors plays a crucial role, since motors move filaments against each other. In particular, the formation of microtubule asters, structures where many microtubules run from a center into radial direction, has been studied extensively, see e.g. [59–63]. In chapter 4 we discuss concentration profiles in arrays of filaments such as microtubule asters.

In the following chapters, we introduce and study a class of models, which on the one hand provide a simple framework to discuss several generic phenomena related to the long-time

Motor	Filament	ℓ (nm)	v_b (nm/s)	D_b (nm ² /s)	Δx_b (μm)	Δt_b (s)	
Dimeric kinesin	microtubule	8	680	1360			[29]
Dimeric kinesin	microtubule	8	710	2200	2.0	2.6	[15]
Monomeric kinesin (KIF1A)	microtubule	8	140	44000	0.84	6.1	[15]
Myosin V	actin	36	360	5800	1.6	4.5	[31, 32]
Dynein	microtubule	8	422		2.6	6.2	[34]
Dynein	microtubule	8	700		0.7	1.0	[33]
Dynein (+ dynactin)	microtubule	8	700		1.5	2.1	[33]

Table 1.1: Transport properties of motors bound to filaments: filament repeat distance ℓ , bound state velocity and diffusion coefficient, v_b and D_b , walking distance Δx_b and walking time Δt_b .

regime (III) and, on the other hand, allow precise numerical results for specific motors to be obtained. An additional ingredient of our theoretical studies are interactions of motors. In particular, we will study phenomena which are due to the simple fact that motors occupy a certain spatial region and that only one motor can bind to a given binding site of a filament.

1.2.3 Bound and unbound movements

Let us consider movements of motors over large scales, i.e. in regime (III), in more detail. Movements in this regime consist of an alternating sequence of bound and unbound motion. A bound motor performs active directed movement in a direction defined by the polarity of the filament to which the motor is bound. The bound movement is characterized by the bound state velocity, v_b , and the bound state diffusion coefficient, D_b , which describes the stochastic fluctuations in the directed motion. The bound velocity and diffusion coefficient can be influenced by several parameters, the most important of which is the concentration of the fuel molecules, ATP.

A third quantity characterizing the directed walks of bound motors, is the walking time Δt_b , the average time the motor spends bound to a filament and moving along it in a directed way. Equivalently, we can consider the walking distance Δx_b , related to the walking time by $\Delta x_b = v_b \Delta t_b$. Walking time and walking distance depend on the ionic conditions, see e.g. [64]. As mentioned before, the transport properties of bound motors along filaments have been measured for various types of motors. An overview over these transport properties is given in Table 1.1, which represents an update of the table in Ref. [56].

Unbound motion, on the other hand, is purely diffusive and non-directed. It is characterized by the unbound diffusion coefficient, D_{ub} , which is given by the Stokes–Einstein relation (1.1). Eq. (1.1) implies $D_{ub} = (100 \text{ nm}/R_{\text{hyd}}) \times 2.4 \mu\text{m}^2/\text{s}$ for a particle with the hydrodynamic radius R_{hyd} in water at room temperature. From this, we can estimate the diffusion coefficient for a motor without cargo as $D_{ub} \simeq 24 \mu\text{m}^2/\text{s}$ and for a motor with a 100 nm bead as $D_{ub} \simeq 2.4 \mu\text{m}^2/\text{s}$. Note that these values are for diffusion in water; as $D_{ub} \sim 1/\eta$, diffusion can be slowed down by adding additional solutes that increase the viscosity η . Diffusion *in vivo* is more complicated and depends strongly on the size of the diffusing particle [65]. Diffusion of small particles such as a motor molecule without cargo is reduced by a factor of three

compared to diffusion in water, but for larger particles, e.g. for a motor carrying a cargo of diameter 100nm, the reduction factor is much larger, since these particles are hindered by the gel-like structures of the cytoskeleton [65]. In addition, unbound motors in the cell can stick to other objects within the cytosol, which reduces the effective diffusion coefficient further. By contrast, *in vitro* motion of bound motors is usually slow compared to unbound diffusion, $D_b \ll D_{ub}$ and $v_b \ell \ll D_{ub}$, where ℓ is the repeat distance of the filament. This can, however, be changed, if unbound diffusion is slowed down.

1.3 Overview

This thesis is organized as follows. Chapter 2 introduces the models which we will use in the following chapters to study the random walks of molecular motors. These random walks consist of an alternating sequence of directed movements along filaments and unbound diffusion. We describe how the model parameters can be chosen in agreement with experimentally determined transport properties of bound and unbound motors, discuss the analytical description of the model, and introduce several approximations.

In chapter 3, random walks of single tracer motors in open compartments are discussed. Long-range movement depends on the geometry of the compartment, therefore we discuss explicitly several simple types of open compartments, in particular, half space, slab and tube geometries, which can be realized in experiments. In these systems, anomalous drift velocities and enhanced diffusion in the direction of the filaments can be observed.

Chapters 4 and 5 are concerned with motors interacting through hard core exclusion. In chapter 4, we consider stationary concentration profiles in closed compartments, where currents along the filaments are balanced by diffusive currents of unbound motors. Since the local concentrations of bound motors can get quite large, exclusion effects have to be taken into account which lead to mutual steric hindrance of motors, and to concentration profiles that depend on the total motor concentration. We study again two experimentally accessible geometries, uniaxial and aster-like arrangements of filaments. In chapter 5, we reconsider the open tube geometry introduced in chapter 3, but now for the case of higher motor concentration, so that exclusion effects are important. This case exhibits boundary-induced phase transitions similar to the asymmetric simple exclusion process, but with a phase diagram which depends on the precise choice of the boundary conditions.

In chapter 6, we discuss effective attractive interactions of motors. This is a largely unexplored topic from the experimental point of view, but making some simple and plausible assumptions, we are able to study this topic in a rather general way. If two species of motors compete for the binding sites of the filament, in the sense that motor–filament binding is enhanced next to a bound motor of the same species and weakened next to one of the other species, two kinds of phase transitions can be observed, a continuous transition with spontaneous symmetry breaking for sufficiently strong interactions in systems with equal numbers of motors of both species and a discontinuous transition, accompanied by hysteresis, upon varying the relative concentrations of the two species.

Finally, we conclude with a summary and outlook, pointing out possible experiments and raising a few open questions in chapter 7.

Chapter 2

Lattice models for the walks of molecular motors

In this chapter, we introduce the class of models which will be studied in the following chapters. Random walks of molecular motors which consist of alternating sequences of directed movements along filaments and unbound diffusion are mapped onto random walks on a lattice. Diffusive motion of unbound motors is represented by symmetric random walks, while movements of motors bound to a filament are mapped to biased random walks along a line.

On the one hand, these models describe *generic* behaviour and apply to all motors irrespective of the underlying motor mechanism responsible for processive movements. On the other hand, the hopping rates of the model can be adapted to the parameters of motion of bound and unbound motor movements to obtain results for *specific* motor molecules. Several variants of these lattice models are introduced in this chapter as well as the corresponding continuum equations and some approximations used in the following chapters. In addition, we discuss how motor–motor interactions can be included in the models.

2.1 Lattice models

Processive motors moving along cytoskeletal filaments detach from their tracks after a certain walking time, since their binding energy is finite and can be overcome by thermal fluctuations. Unbound motors then diffuse freely in the surrounding fluid, until they eventually reattach to the same or another filament. Hence, if motors are observed over a sufficiently long time, i.e. over many diffusive encounters with filaments, they perform peculiar random walks which consist of alternating sequences of directed movements along filaments and unbound diffusion. In this section we introduce lattice models for these walks: Depending on whether the motor is bound to a filament or not, it performs a biased (one-dimensional) random walk along the filament or a symmetric random walk in the (usually three-dimensional) surrounding fluid. The hopping rates are determined from the parameters of motion of bound and unbound motors.

We will introduce two variants of these models. The first one is a bit simpler, while the second one allows for a more accurate adaptation of the model parameters to the measured parameters of motion. Let us however anticipate that (i) the transport phenomena discussed in the following chapters are generic in the sense that they do not depend on the precise choice of the model details and that (ii) even the quantitative agreement of the two model variants is quite good. We will therefore use both lattice models in parallel, as well as continuum

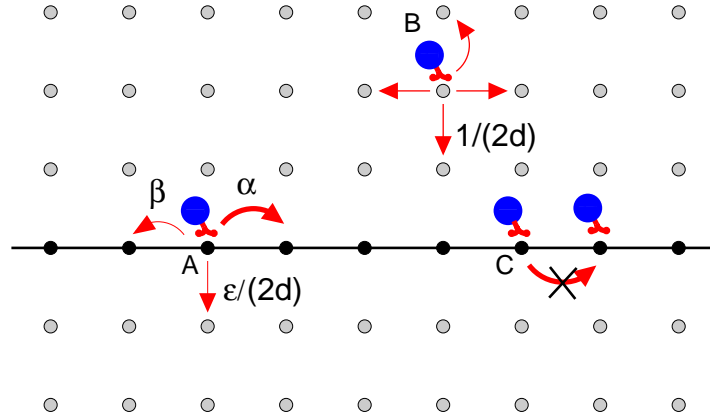


Figure 2.1: Mapping of the random walks of molecular motors onto a lattice model. The line represents a filament. Motor 'A' is bound to this filament and performs a biased random walk, motor 'B' is unbound and performs a symmetric random walk. In cases with hard core exclusion, hopping to occupied sites is forbidden (motor 'C'), see section 2.3 below.

descriptions.

2.1.1 Basic lattice model

In our models, motors move on a d -dimensional simple cubic lattice¹ with lattice constant ℓ . Filaments correspond to lines on this lattice. Along the filaments, a lattice structure is naturally given, since motors bind to specific binding sites, which are located periodically along the filament. These binding sites are represented in the model by the lattice sites on the lines corresponding to the filaments. The lattice constant ℓ is thus chosen to be the repeat distance of the filament, which is 8 nm in the case of kinesin motors moving along microtubules and 36 nm for myosin V motors moving along actin filaments. In the following, we will usually express all lengths in units of ℓ and specify the explicit dependence on ℓ only, when we are presenting numerical results for specific motors. Let us mention that microtubules usually consist of 13 protofilaments aligned in parallel. This can easily be modeled by parallel lines on the lattice. For simplicity, we will, however, neglect this fact in the following with the exception of chapter 4.4.

Away from the filament, the motor performs a symmetric random walk. It hops with equal probability to any of the neighbour sites. The hopping rate is $1/(2d\tau)$, where τ is the basic time scale of these random walks. τ is fixed to $\tau = \ell^2/(2dD_{\text{ub}})$ to adapt the model to the unbound diffusion coefficient, D_{ub} . In the computer simulations, τ is chosen as the discretization time.² We will also usually express times and rates in units of τ and τ^{-1} , respectively, in the following. Walls are included in the model as reflecting surfaces. A motor hopping to a lattice site of a wall is reflected to its starting site. Finally, if a motor reaches a site of a filament, it adsorbs there with the sticking probability π_{ad} .

On the other hand, if the motor is bound to a filament, it performs a biased random walk.

¹The dimension will usually be $d = 3$ as appropriate for real systems. In addition, we will discuss the case $d = 2$ in chapter 3.

²A brief description of the simulations is given in appendix A.

Per time τ , it makes a forward step with probability α , a backward step with probability β and no step at all with probability γ , see Fig. 2.1. With a small probability $\epsilon/(2d)$, it unbinds to each of the n_{ad} adjacent non-filament sites. There are $n_{\text{ad}} = 4$ such non-filament neighbour sites in the case of filaments in solution and $n_{\text{ad}} = 3$ if the filament is attached to a wall. As the sum of all hopping probabilities is one, we have $\gamma = 1 - \alpha - \beta - n_{\text{ad}}\epsilon/(2d)$.

2.1.2 Master equations

The dynamics described above can be summarized into master equations. Let us consider the case of a single filament located along the x -axis of a three-dimensional lattice. The coordinates along the two Cartesian axes perpendicular to the filament are denote by y_1 and y_2 . The lattice sites of the filament thus have coordinates $(x = n\ell, y_1 = 0, y_2 = 0)$. We first focus on the case of a single tracer motor.

We denote the probability that the motor is at a lattice site $(x, y_1, y_2) = (n\ell, m_1\ell, m_2\ell)$ at time t by $p(x, \mathbf{y}, t) = p_{n, \mathbf{m}}(t)$. We also introduce $P(x, t) = P_n(t) \equiv p_{n, 0, 0}(t)$ for the bound motors and express all lengths and times in units of ℓ and τ , respectively.

With these definitions, the master equations for the random walk of the motor are given by

$$P_n(t+1) = \alpha P_{n-1}(t) + \beta P_{n+1}(t) + \gamma P_n(t) + \frac{\pi_{\text{ad}}}{6} \sum_{\mathbf{i}} p_{n, \mathbf{i}}(t) \quad (2.1)$$

$$\begin{aligned} p_{n, \mathbf{m}}(t+1) &= \frac{1}{6} \left(p_{n+1, \mathbf{m}}(t) + p_{n-1, \mathbf{m}}(t) + \sum_{\mathbf{i}} p_{n, \mathbf{m}+\mathbf{i}}(t) \right) \\ &+ \sum_{\mathbf{i}} \delta_{\mathbf{m}, \mathbf{i}} \left(\frac{\epsilon}{6} P_n(t) - \frac{1}{6} p_{n, \mathbf{0}}(t) + \frac{1 - \pi_{\text{ad}}}{6} p_{n, \mathbf{m}}(t) \right), \end{aligned} \quad (2.2)$$

where Eq. (2.2) holds for all $\mathbf{m} \neq (0, 0)$. The summation variable \mathbf{i} runs over the transversal neighbours, $(0, \pm 1)$ and $(\pm 1, 0)$. Eqs. (2.1) and (2.2) specify the dynamics at filament and non-filament sites, respectively. The first line of Eq. (2.2) is the symmetric hopping of an unbound motor, while the second line of Eq. (2.2), which contributes only at sites adjacent to the filament, describes attachment to and detachment from the filament.

As the basic time scale τ is usually small compared to the time scales defined by the hopping rates, we can also take the continuum limit for the time variable. In this case, Eqs. (2.1) and (2.2) take the form

$$\frac{\partial}{\partial t} P_n(t) = \alpha P_{n-1}(t) + \beta P_{n+1}(t) - (1 - \gamma) P_n(t) + \frac{\pi_{\text{ad}}}{6} \sum_{\mathbf{i}} p_{n, \mathbf{i}}(t) \quad (2.3)$$

$$\frac{\partial}{\partial t} p_{n, \mathbf{m}}(t) = \frac{1}{6} \left(p_{n+1, \mathbf{m}}(t) + p_{n-1, \mathbf{m}}(t) + \sum_{\mathbf{i}} p_{n, \mathbf{m}+\mathbf{i}}(t) \right) - p_{n, \mathbf{m}}(t) \quad (2.4)$$

$$+ \sum_{\mathbf{i}} \delta_{\mathbf{m}, \mathbf{i}} \left(\frac{\epsilon}{6} P_n(t) - \frac{1}{6} p_{n, \mathbf{0}}(t) + \frac{1 - \pi_{\text{ad}}}{6} p_{n, \mathbf{m}}(t) \right). \quad (2.5)$$

Note that all rates in these equations are given in units of τ^{-1} .

Eqs. (2.1)–(2.2) and (2.3)–(2.5) hold for a system without confining walls. If walls are present, all terms corresponding to currents through the walls have to be omitted in the

equations for lattice sites adjacent to the walls and the dwell probability must be increased at these sites to account for reflection at the wall.

Let us now turn to the case of more than one motor. In this case the quantity of main interest is the motor density at site $(x, y_1, y_2) = (n\ell, m_1\ell, m_2\ell)$ at time t . We denote it by $\rho_{\text{ub}}(x, \mathbf{y}, t)$, if the lattice site is a non-filament site, i.e. if $\mathbf{y} \neq \mathbf{0}$, and by $\rho_{\text{b}}(x, t)$, if it is a filament site. If the motors do not interact or if the total motor concentration is sufficiently small, so that motor–motor interactions can be neglected, the local motor densities, $\rho_{\text{b}}(x, t)$ and $\rho_{\text{ub}}(x, \mathbf{y}, t)$ are governed by the same dynamics as $P(x, t)$ and $p(x, \mathbf{y}, t)$ and differ only in normalization. Neglecting motor–motor interactions is appropriate in the case of a fixed number of motors in an infinite system such as the open compartments discussed in chapter 3. On the other hand, interactions are important in closed systems, where local motor densities can get large due to accumulation of motors. Interacting motors will be discussed further in section 2.3.

2.1.3 Mapping parameters of motion to the hopping rates

Let us now describe how the hopping rates of the model can be determined from the parameters of motion of motors known from experiments. As an example, we consider the case of dimeric kinesin.

As mentioned above, the time scale τ is determined from the unbound diffusion coefficient D_{ub} as $\tau = \ell^2/(2dD_{\text{ub}})$. D_{ub} is given by the Stokes–Einstein relation (1.1), which implies $D_{\text{ub}} = (100 \text{ nm}/R_{\text{hyd}}) \times 2.4 \mu\text{m}^2/\text{s}$ for a particle with the hydrodynamic radius R_{hyd} in water at room temperature. For a kinesin molecule carrying a 100nm bead, we thus have $D_{\text{ub}} = 2.4 \mu\text{m}^2/\text{s}$ and therefore $\tau \simeq 4.4 \times 10^{-6}$ s.

The hopping rates for the movements of the bound motors are fixed by the measured parameters of motion of bound motors. As backward steps are very rare for dimeric kinesin, β can be set to zero. The forward rate is then fixed by the bound velocity $v_{\text{b}} = \bar{\alpha} \ell/\tau = \bar{\alpha} 2dD_{\text{ub}}/\ell$ with $\bar{\alpha} = \alpha/(\alpha + \beta + \gamma)$ and the detachment parameter ϵ is determined from the walking time $\Delta t_{\text{b}} = (\frac{1}{n_{\text{ad}}\epsilon/(2d)} - 1)\tau$. Note that ϵ is related to the binding energy ΔE of the motor–filament binding, $\epsilon \sim \exp(-\Delta E/k_{\text{B}}T)$. As the sum of all hopping probabilities is one, the dwell probability γ is given by $\gamma = 1 - \alpha - \beta - n_{\text{ad}}\epsilon/(2d)$. The bound velocity of dimeric kinesin is $v_{\text{b}} = 680 \text{ nm/s}$ and the motor makes on average 100 steps before detaching [29], thus for dimeric kinesin, we obtain in this way $\alpha \simeq 3.78 \times 10^{-4}$, $\gamma \simeq 0.99962$ and $\epsilon \simeq 5.61 \times 10^{-6}$. In addition, the sticking probability is taken to be $\pi_{\text{ad}} = 1$. Note that γ is close to one. This means that the discretization time τ is small compared to all other time scales, so that we are essentially dealing with random walks in continuous time. The reason for this, which is also the reason why the parameter γ has to be introduced, is that the ratio $D_{\text{ub}}/(v_{\text{b}}\ell)$ is large; in our specific case, it is $\simeq 440$.

2.1.4 Modified lattice model

The model described in the previous sections accounts for the unbound diffusion coefficient, the bound velocity and the average number of steps before detaching, but the bound diffusion coefficient was not taken into account. As we will discuss in the following, accounting for the bound diffusion coefficient as well, makes it necessary to refine the model. We therefore introduce a slightly modified variant of our model. This modified model variant is the variant originally proposed in Ref. [56].

As mentioned above, $D_{\text{ub}}/(v_{\text{b}}\ell)$ is large, so that the time unit τ is small and the bound motion is effectively a random walk in continuous time. In this case the bound velocity v_{b} and the bound diffusion coefficient D_{b} are given by

$$v_{\text{b}} = (\bar{\alpha} - \bar{\beta})\frac{\ell}{\tau} \quad \text{and} \quad D_{\text{b}} = (\bar{\alpha} + \bar{\beta})\frac{\ell^2}{2\tau}, \quad (2.6)$$

where $\bar{\alpha} = \alpha/(\alpha + \beta + \gamma)$ and $\bar{\beta} = \beta/(\alpha + \beta + \gamma)$. This implies that the ratio

$$r = \frac{2D_{\text{b}}}{v_{\text{b}}\ell}, \quad (2.7)$$

called the randomness parameter, must be larger than one, as the minimal diffusion coefficient is $\bar{\alpha}\ell^2/(2\tau)$ and the maximal velocity is $\bar{\alpha}\ell/\tau$. The minimal value of the randomness parameter is obtained for $\bar{\alpha} = 1$ and $\bar{\beta} = 0$. In contrast to this result, the measured value of r for dimeric kinesin is approximately 1/2 over a large range of load forces and ATP concentrations [30]. Similarly, $r \simeq 0.9$ has been reported for myosin V [32].

We therefore introduce a modified lattice model, which allows us to incorporate the correct value for the bound diffusion coefficient. Let us, however, mention, that for the behaviour at large times, the precise value of the bound diffusion coefficient is of minor importance. Some transport quantities like the time-dependent drift velocities discussed in chapter 3 are even completely independent of it. It is therefore legitimate to use the simpler model and, in the following chapters, we will use both model variants in parallel.

A randomness parameter smaller than one can be achieved by using a discrete time random walk to describe the bound movements: As τ is very small, we introduce a second time scale τ_{b} which governs the movements of bound motors. A motor bound to the filament then attempts to jump only at discrete times $\tau_0 + n\tau_{\text{b}}$, where n is an integer and τ_0 is the time of attachment to the filament. The hopping rates for bound motors are now given by α/τ_{b} , β/τ_{b} , γ/τ_{b} and $\epsilon/(6\tau_{\text{b}})$. The parameters α , β , γ , ϵ and τ_{b} can be fixed by the bound velocity, the bound diffusion coefficient, the average step number or walking distance, the assumption $\beta = 0$ and the condition $\alpha + \beta + \gamma + 4\epsilon/6 = 1$. In contrast to the previous case, the bound velocity and diffusion coefficient are now given by

$$v_{\text{b}} = (\bar{\alpha} - \bar{\beta})\frac{\ell}{\tau_{\text{b}}} \quad \text{and} \quad D_{\text{b}} = [\bar{\alpha} + \bar{\beta} - (\bar{\alpha} - \bar{\beta})^2]\frac{\ell^2}{2\tau_{\text{b}}}. \quad (2.8)$$

The diffusive spreading of a distribution of motors is reduced because the motors hop only at discrete times. In the case $\bar{\alpha} = 1$ and $\bar{\beta} = 0$ motor movements are perfectly synchronized and the diffusion coefficient D_{b} vanishes.

For the kinesin motors discussed above, the bound diffusion coefficient is $1360 \text{ nm}^2/\text{s}$ [29], corresponding to a randomness parameter of 1/2. We thus obtain $\alpha = 0.4975$, $\gamma = 0.4975$, $\epsilon = 0.00746$ and $\tau_{\text{b}} = 1341\tau$. These values will be used several times in the following chapters.

Let us add a few remarks: (1) The choice $\beta = 0$ implies a simple relation between the time scale τ_{b} and the randomness parameter r : For $\beta = 0$ we obtain $\bar{\alpha} = 1 - r$ and it follows that $\tau_{\text{b}} = (1 - r)\ell/v_{\text{b}}$.

(2) This refined model can be considered as a generalization of the simpler model introduced above. The simpler model is recovered in the particular case $\tau_{\text{b}} = \tau$.

(3) From the mathematical point of view, the refined model defines a Markov process of order τ_{b}/τ , see Ref. [66], since hopping depends on the state of the motor at the present time

and at the $\tau_b/\tau - 1$ preceding time steps. It is equivalent to a Markov process, which describes the motor as a particle with τ_b/τ possible internal states.

(4) From the physical point of view, the randomness parameter reflects the dynamics of the mechano-chemistry of the single step, i.e. the dynamical regime (I) in the terminology of chapter 1.2.2, which we do not model here. Introducing the time scale τ_b should be viewed as a way to incorporate the experimentally observed transport properties into our models rather than as accurately modeling the short-time regime (I), though it is related to the mean step time $\tau_s = \tau_b/(1 - \gamma)$ and the mean dwell time $\tau_{dw} = \tau_s - \tau_b = \tau_b\gamma/(1 - \gamma)$. In microscopic models, randomness parameters smaller than one arise either through a series of transitions between mechano-chemical states or through stepping with non-exponential waiting time distributions [51].

2.2 General features of the models

The class of models introduced above provides a framework for theoretical studies of the movements of processive molecular motors over long time and length scales. It incorporates the transport properties of both motors in solution and motors bound to filaments as well as adsorption and detachment rates. In particular, the large difference between bound and unbound diffusion coefficients (in water) and the small ratio $D_{ub}/(v_b\ell)$ is included easily. It thus provides a bridge from the intermediate-time regime of motor movements, where a motor performs a directed walk along a filament, to the long-time regime, where motor movements consist of many diffusive encounters with filaments. Let us mention again, that the parameters of the models can be chosen to incorporate all experimentally observed transport properties for a specific motor.³

On the other hand, many phenomena exhibited by these models are generic in the sense, that they do not depend on the precise choice of these parameters, but only on the basic fact that active, directed motion along filamentous objects is coupled to diffusion. In particular, no specific assumptions have to be made about the mechanisms by which the motors work, or the underlying molecular dynamics. Accordingly, our models are still sufficiently simple to allow for some analytical solutions.

As mentioned, the lattice structure along the filament arises in a natural way, while it is somewhat artificial, though not dangerous, for the unbound movements. From the theoretical point of view, the mapping of motor movements onto random walks on a lattice yields two advantages beyond its conceptual simplicity: (i) Interactions of motors can be easily included by considering hopping rates which depend on whether neighbouring lattice sites are occupied by other motor particles; see the following section for a more detailed discussion. (ii) We can make use of well-known results and methods of solution for random walks on a lattice, see, e.g., Refs. [66, 67], and (in the case of interacting motors) driven lattice gas models and exclusion processes, see, e.g., Refs. [68, 69]. There is, however, an important fundamental difference to these classes of models: In these models, one usually deals with spatially homogeneous systems (or homogeneously disordered systems), i.e., the hopping rates (or the statistical properties of hopping rates) are independent of the position of the walker, while in our models, the hopping rates depend on whether a lattice site belongs to a filament or not.

³In principle, even the case of motor complexes or several motors transporting one cargo together can be studied with this model; see appendix C, where we determine effective detachment rates and velocities for this case.

2.3 Interacting motors

As mentioned, motor–motor interactions can be included in our models by introducing hopping rates which depend on the positions of the other motors in the system. The most important interaction between motors that we will consider in the following chapters is mutual exclusion or hard core repulsion: If a motor is bound to a binding site of the filament, other motors cannot bind to that site. As motors are strongly attracted by the filaments, exclusion can become important even at small overall motor concentrations. In principle, steric hindrance affects also the motors in solution. However, as concentrations of unbound motors are usually much smaller, it is much less important than for motors bound to the filaments.

In our models, exclusion is taken into account by rejecting all hops to lattice sites which are already occupied by another motor particle. This means that the hopping rates defined above are now interpreted as rates for hopping attempts and the success of these attempts depends on whether the target site is occupied or not.

If exclusion interactions are included, our models constitute novel variants of exclusion processes or driven lattice gas models. Such models have been extensively studied in the context of ionic conductors [70], traffic flow [71,72] and non-equilibrium phase transitions, e.g. [73–75]. The simplest of these models is the asymmetric simple exclusion process (ASEP) in one dimension, in which particles hop on a one-dimensional lattice with a strong bias towards one direction (in the simplest case, there are no backward steps at all) and the only interaction of the particles is hard core exclusion, i.e., steps to occupied lattice sites are forbidden. Because of its simplicity, the ASEP has become a paradigmatic model for non-equilibrium phase transitions. We will review the most interesting case of an ASEP with open boundaries in chapter 5. Let us, however, emphasize again that, in contrast to previously studied lattice gas models, the walks of molecular motors are only 'driven' as long as the motors are attached to a filament, i.e. the 'driving' is localized to one or several lines.

In a mean field approach, we can incorporate mutual exclusion into the rates as factors $[1 - \ell^3 \rho_b(\vec{y})]$, where \vec{y} is the target site, since this factor is the probability that the target site is vacant.⁴ The master equations are thus

$$\begin{aligned} \frac{\partial}{\partial t} \rho_b(x, t) &= \alpha \left(\rho_b(x-1, t) [1 - \rho_b(x, t)] - \rho_b(x, t) [1 - \rho_b(x+1, t)] \right) \\ &+ \sum_{\mathbf{i}} \left(\frac{\pi_{\text{ad}}}{6} \rho_{\text{ub}}(x, \mathbf{i}, t) [1 - \rho_b(x, t)] - \frac{\epsilon}{6} \rho_b(x, t) [1 - \rho_{\text{ub}}(x, \mathbf{i}, t)] \right) \end{aligned} \quad (2.9)$$

$$\begin{aligned} \frac{\partial}{\partial t} \rho_{\text{ub}}(x, \mathbf{y}, t) &= \frac{1}{6} \left(\rho_{\text{ub}}(x+1, \mathbf{y}, t) + \rho_{\text{ub}}(x-1, \mathbf{y}, t) + \sum_{\mathbf{i}} \rho_{\text{ub}}(x, \mathbf{y} + \mathbf{i}, t) \right) - \rho_{\text{ub}}(x, \mathbf{y}, t) \\ &+ \sum_{\mathbf{i}} \delta_{\mathbf{y}, \mathbf{i}} \left(\frac{1}{6} \rho_{\text{ub}}(x, \mathbf{y}, t) - \frac{1}{6} \rho_{\text{ub}}(x, \mathbf{0}, t) \right. \\ &\left. - \frac{\pi_{\text{ad}}}{6} \rho_{\text{ub}}(x, \mathbf{i}, t) [1 - \rho_b(x, t)] + \frac{\epsilon}{6} \rho_b(x, t) [1 - \rho_{\text{ub}}(x, \mathbf{i}, t)] \right). \end{aligned} \quad (2.10)$$

Note that we have set $\beta = 0$, as appropriate for most processive motors, since backward steps

⁴If motors carry large cargoes, the excluded volume can be larger. We will consider this case briefly in chapter 4.4.

are very rare. Some comments may be useful for the understanding of Eq. (2.10): The first line describes symmetric hopping away from the filament, here exclusion terms cancel each other, the second line subtracts terms from the first line, which are absent for lattice sites adjacent to a filament site and the last line describes attachment and detachment. The detachment term contains a factor $(1 - \rho_{\text{ub}})$ describing hard core exclusion of unbound motors. As the unbound density is usually very small, this factor has very little influence on the results and can be safely ignored in most cases.⁵

For one-dimensional models such as the asymmetric simple exclusion process (ASEP), several methods have been developed to go beyond the mean field approximation and to obtain exact results. These methods include mapping to quantum spin chains and a matrix approach, see, e.g., Refs. [69, 76]. As our models are more complex than these one-dimensional models, we will, however, not go beyond the mean field approximation in the following chapters. An exception is the case of a tube with periodic boundary conditions in chapter 5, for which we will derive an exact solution using the 'quantum Hamiltonian' method in appendix D.1.

Finally, we should remark that only little experimental data is available concerning motor-motor interactions. Exclusion effects are clearly observed in microtubule decoration experiments, where one motor head binds to each tubulin subunit [77]. In motility assays, a decrease of the gliding velocity is observed, if the motor concentration at the surface is increased [78]. Interactions other than simple exclusion will be discussed in chapter 6.

2.4 Continuum equations

For an analytical description, it is sometimes more convenient to consider movements in a continuous space rather than walks on a lattice. As we are mainly interested in the behaviour on large time and length scales, neglecting the lattice structure does not strongly affect our results.

Expanding the probabilities in the length unit ℓ up to second order and in the time unit τ up to first order, we obtain⁶

$$\frac{\partial p}{\partial t} = D_{\text{ub}} \Delta p + \delta(\mathbf{y}) [\tilde{\epsilon} P - \tilde{\pi}_{\text{ad}} p_0] \quad (2.11)$$

$$\frac{\partial P}{\partial t} = -v_{\text{b}} \frac{\partial P}{\partial x} + D_{\text{b}} \frac{\partial^2 P}{\partial x^2} - \tilde{\epsilon} P + \tilde{\pi}_{\text{ad}} p_0, \quad (2.12)$$

with $v_{\text{b}} = (\alpha - \beta)\ell/\tau$, $D_{\text{b}} = \frac{\alpha+\beta}{2}\ell^2/\tau$, $D_{\text{ub}} = \frac{1}{6}\ell^2/\tau$, $\tilde{\epsilon} \equiv 4\epsilon/6$ and $\tilde{\pi}_{\text{ad}} \equiv 4\pi_{\text{ad}}/6$. Δ is the three-dimensional Laplace operator.

Note that the probability density $p(x, \mathbf{y}, t)$ is a density in three-dimensional space, while $P(x, t)$ and $p_0(x, t)$ are densities on a line. In principle, we have $p_0(x) = \ell^2 p(x, \mathbf{y} = \mathbf{0})$, if the

⁵A more formal way to obtain these equations is to define occupation variables $\eta(\vec{x})$, which are 1 or 0 if site \vec{x} is occupied by a motor or free, respectively. The density $\rho(\vec{x})$ is the expectation value of the occupation variable, $\rho(\vec{x}) = \langle \eta(\vec{x}) \rangle$, and hopping currents from site \vec{x} to site \vec{y} are then given by $\sigma \langle \eta(\vec{x}) [1 - \eta(\vec{y})] \rangle$, where σ stands for the corresponding rate; e.g., the current for a forward step at a filament site \vec{x} is $\alpha \langle \eta(\vec{x}) [1 - \eta(\vec{x}+1)] \rangle$. Collecting the current terms into a master equation, an equation for the expectation value of $\langle \eta \rangle$ or the density is obtained, which, however, involves the two-point correlation function $\langle \eta(\vec{x}) \eta(\vec{y}) \rangle$ as well. Eq. (2.9) is then obtained by the mean field approximation, $\langle \eta(\vec{x}) \eta(\vec{y}) \rangle \simeq \rho(\vec{x}) \rho(\vec{y})$. Let us also mention that to treat the equations for $\langle \eta(\vec{x}) \rangle$ exactly, the corresponding equations for $\langle \eta(\vec{x}) \eta(\vec{y}) \rangle$ have to be solved simultaneously, which in turn involves again higher correlation functions, resulting in the need for other methods of solution [76].

⁶We could also truncate the expansions at the first non-vanishing order and thus neglect the bound diffusion term. We will use this further approximation sometimes to simplify the equations.

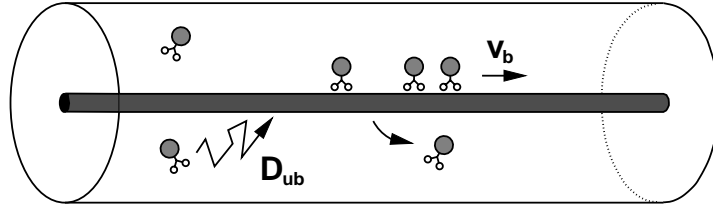


Figure 2.2: Motors which can bind to and unbind from a filament (dark rod) within a cylindrical tube. Single motors which are bound to the filament (and are not sterically hindered by other motors) move with velocity v_b to the right. Unbound motors diffuse with diffusion coefficient D_{ub} in the surrounding liquid.

filament is a line. This will lead to divergences in the analytical calculations, see chapters 3.4 and 4.3. Since a real filament, however, has a finite thickness, the δ function should not be taken literally. The expressions can be regularized by introducing the filament thickness a as a cutoff or, equivalently, putting $p_0(x) \sim \ell^2 p(x, |\mathbf{y}| = a)$.

The same approximation can be done for the case, where exclusion interactions are present and treated by the mean field approach. In this case, the continuum equations contain additional quadratic terms:

$$\frac{\partial \rho_{ub}}{\partial t} = D_{ub} \Delta \rho_{ub} + \delta(\mathbf{y}) \left[\tilde{\epsilon} \rho_b (1 - \rho_{ub,0}) - \tilde{\pi}_{ad} \rho_{ub,0} (1 - \rho_b) \right] \quad (2.13)$$

$$\frac{\partial \rho_b}{\partial t} = -v \frac{\partial}{\partial x} \rho_b (1 - \rho_b) + D_b \frac{\partial^2 \rho_b}{\partial x^2} - \tilde{\epsilon} \rho_b (1 - \rho_{ub,0}) + \tilde{\pi}_{ad} \rho_{ub,0} (1 - \rho_b). \quad (2.14)$$

Again, we have in principle $\rho_{ub,0}(x) = \ell^2 \rho_{ub}(x, \mathbf{y} = \mathbf{0})$. Note also, that the bound diffusion coefficient D_b can be considered as an independent parameter in the continuum equations and fixed to the experimentally measured value rather than to the value obtained from the hopping rates of the lattice model, so that these continuum equations can be used for both variants of the lattice models.

2.5 Two-state approximation

In the following chapters we will frequently consider stationary states in tube-like systems as shown in Fig. 2.2. One filament is aligned parallel to the symmetry axis of the tube which is taken to be the x -axis. In the lattice model, the discretized tube consists of one or several lines which represent the filaments and N_{ch} unbound 'channels', lines of lattice sites parallel to the x -axis. N_{ch} is related to the tube cross section ϕ by $\phi = (1 + N_{ch})\ell^2$.

In these systems, the unbound density depends only weakly on the radial coordinate. Therefore the following approximation is useful: We take the unbound density to depend only on the coordinate parallel the filament, x , so that a motor can be in one of two states, bound or unbound. The two-state description is exact for $N_{ch} = 1$ and for an arbitrary number N_{ch} of *equivalent* unbound channels. In all other cases, it gives a reasonable approximation, the validity of which will be discussed in chapter 4.3.

Assuming that ρ_{ub} depends only on x and summing all equations for the densities at

non-filament sites, we obtain

$$\begin{aligned} \frac{\partial}{\partial t} \rho_b(x, t) &= \alpha \left(\rho_b(x-1, t)[1 - \rho_b(x, t)] - \rho_b(x, t)[1 - \rho_b(x+1, t)] \right) \\ &\quad + \tilde{\pi}_{\text{ad}} \rho_{\text{ub}}(x, t)[1 - \rho_b(x, t)] - \tilde{\epsilon} \rho_b(x, t)[1 - \rho_{\text{ub}}(x, t)] \end{aligned} \quad (2.15)$$

$$\begin{aligned} N_{\text{ch}} \frac{\partial}{\partial t} \rho_{\text{ub}}(x, t) &= \frac{N_{\text{ch}}}{6} \left(\rho_{\text{ub}}(x+1, t) + \rho_{\text{ub}}(x-1, t) - 2\rho_{\text{ub}}(x, t) \right) \\ &\quad - \tilde{\pi}_{\text{ad}} \rho_{\text{ub}}(x, t)[1 - \rho_b(x, t)] + \tilde{\epsilon} \rho_b(x, t)[1 - \rho_{\text{ub}}(x, t)]. \end{aligned} \quad (2.16)$$

The continuous case is completely analogous. Integrating over the tube cross-section ϕ , we obtain

$$\frac{\partial}{\partial t} \rho_b = -v_b \frac{\partial}{\partial x} \rho_b (1 - \rho_b) + D_b \frac{\partial^2 \rho_b}{\partial x^2} - \tilde{\epsilon} \rho_b (1 - \rho_{\text{ub}}) + \tilde{\pi}_{\text{ad}} \rho_{\text{ub}} (1 - \rho_b) \quad (2.17)$$

$$\phi \frac{\partial}{\partial t} \rho_{\text{ub}} = D_{\text{ub}} \phi \frac{\partial^2 \rho_{\text{ub}}}{\partial x^2} + \tilde{\epsilon} \rho_b (1 - \rho_{\text{ub}}) - \tilde{\pi}_{\text{ad}} \rho_{\text{ub}} (1 - \rho_b). \quad (2.18)$$

The two-state equations can easily be adapted to more complicated arrays of filaments such as parallel arrangements of filaments or asters without increasing the necessary computational efforts. In these cases the cross-section ϕ is replaced by an effective cross-section, which may depend on the spatial coordinate as in the case of the aster geometry, see chapter 4.5.

2.6 Summary

We have introduced lattice models to describe the large-scale movements of molecular motors, which consist of periods of directed movements along filaments and free diffusion if the motor is detached from the filament. These movements are mapped onto random walks on a lattice, where lines on the lattice are identified as the filament. Motors at lattice sites belonging to one of the filaments perform biased random walks with a small probability for detachment, while motors at non-filament sites undergo simple symmetric random walks. In addition, we have discussed how motor–motor interactions can be studied within this framework with particular emphasis on exclusion effects.

Let us finally stress two general features of our class of models: (i) We have introduced several variants of these models (discrete time/continuous time, lattice/continuous space, refined model to account for the bound diffusion coefficient, two-state approximation), but we want to emphasize that all these variants describe the same phenomena. The generic behaviour is the same for all variants (and in most cases even quantitative agreement is quite good). Therefore we will use them in parallel in the following chapters and take advantage of using the description that is most convenient for the particular problem.

(ii) We want to repeat, that our interest in these models is two-fold: On the one hand, we will study generic phenomena related to large-scale movements of motors, which are independent of the choice of parameters and the variant of the model. On the other hand, our models allow us to obtain precise numerical results for specific motors, as the model parameters, in particular the hopping rates, can be fixed by incorporating the experimentally determined parameters of motion of bound and unbound motors.

Chapter 3

Random walks of single motors in open compartments

In this chapter, we will discuss the random walks of molecular motors which result from the combination of directed motion along filaments and diffusion. We consider random walks of single tracer motors in open compartments. In particular, we study half space, slab and tube geometries, which are experimentally accessible, as well as the more idealized cases of a filament in two- or three-dimensional space using scaling arguments, computer simulations and exact analytical and semi-analytical calculations [56, 57].

Movement over large scales is obviously geometry-dependent. In compartments where motors can make excursions away from the filament of unrestricted length, these random walks exhibit *anomalous drift*: The average displacement of the motors grows slower than linearly with time. In addition, diffusion can be strongly enhanced because of attachment to and detachment from the filament. We argue that these effects are accessible to *in vitro* experiments and discuss briefly possible experimental realizations.

3.1 Anomalous drift: Scaling arguments and simulations

In the following, we consider the open compartments shown in Fig. 3.1 with one filament oriented along the x -axis, which is sufficiently long, so that its ends are not reached during the time of observation and we can treat it as infinitely long. We assume that the filament has been immobilized and fixed to a surface, i.e., we do not consider mobile filaments or

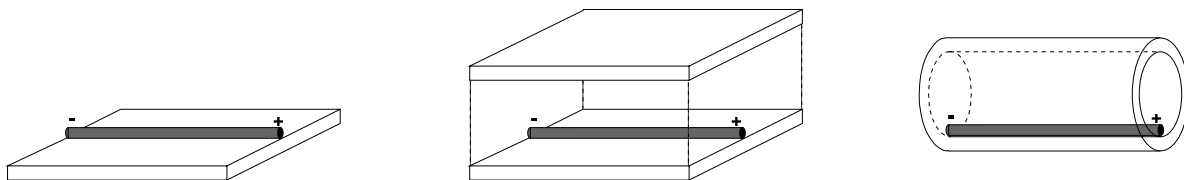


Figure 3.1: Geometries of the open compartments studied in this chapter: Half space, slab, and tube. In all three cases, one filament is immobilized to a surface.

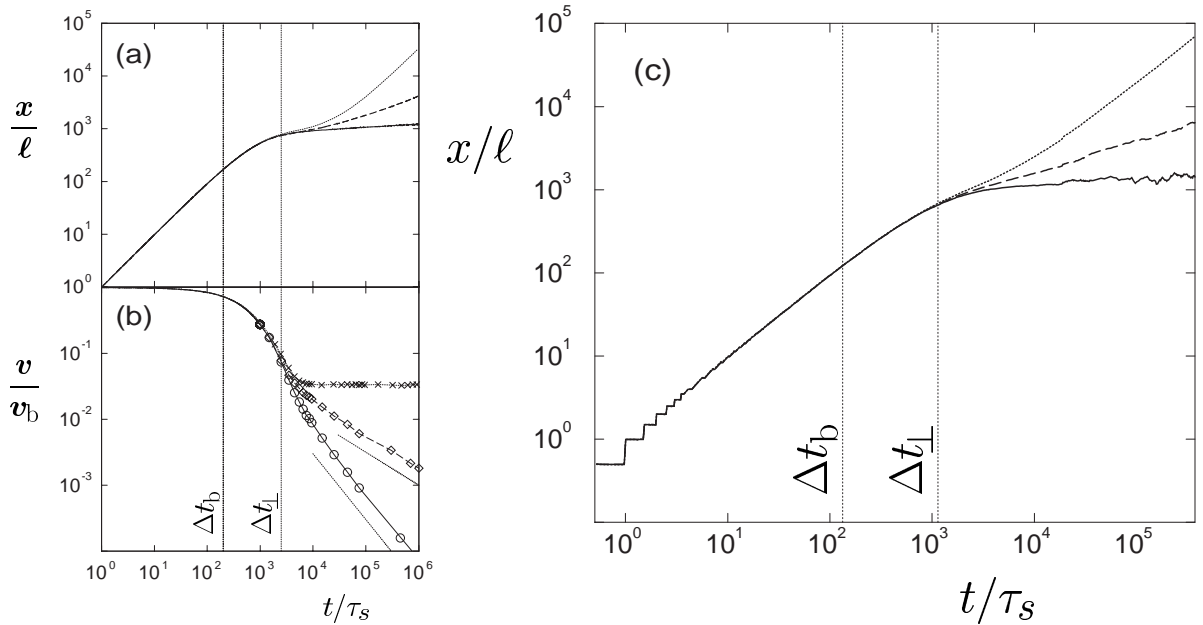


Figure 3.2: (a) Average position x and (b) velocity v of motors in the half space (solid line), slab (dashed line) and tube geometry (dotted line) as functions of time t as obtained from computer simulations of the simple model variant ($\tau_b = 1$). The parameters are $\gamma = 0.99$, $\epsilon = 1.5 \times 10^{-4}$, $\beta = 0$ and $L_{\perp} = 250\ell$. Times are expressed in units of the step time τ_s and lengths in units of the filament repeat distance ℓ . Thin dotted lines in (b) indicate the power laws t^{-1} and $t^{-1/2}$, respectively. (c) Average position x for the modified model for kinesin-like parameters as described in chapter 2.1.4. Data were obtained by averaging over runs of 4500 motors in (a) and (b) and 2000 in (c). Velocity data at large times [data points in (b)] have in addition been time-averaged over 10–30 subsequent data points. The vertical lines mark the crossover times $t = \Delta t_b$ and $t = \Delta t_{\perp}$, see text.

filaments that assemble and disassemble. We also assume that the motor concentration is small, so that interactions of motors can be neglected. The simplest geometry is the half space geometry, where the filament is attached to a surface and unbound motors can explore the whole half space above this surface. This geometry is usually used for *in vitro* experiments with molecular motors. By introducing a second surface above the first one, diffusion of unbound motors can be restricted to the slab between the two planes. In this case, motors can make arbitrarily large excursions away from the filament in only one direction. Finally, by inserting the filament into a tube, diffusion can be further restricted, so that unrestricted diffusion is now only possible in the direction parallel to the filament. In both cases, we denote the linear size of the compartment along the directions of restricted diffusion, i.e. the height of the slab and the radius of the tube, by L_{\perp} .

The main question is how fast motors advance over large distances, when they detach from and reattach to the filament many times. The effective velocity as a function of time as obtained from computer simulations is shown in Fig. 3.2(b). As the motors start bound to the filament in our simulations, the velocity is equal to the bound-state velocity v_b at small times. After the average walking time $\Delta t_b \simeq 6\tau/(n_{ad}\epsilon) = 2\tau/\epsilon$, however, motors are slowed

down, because they start to detach and do not advance in the detached state. Finally for large times, the velocity becomes geometry-dependent. This geometry-dependent regime is reached after a time $\Delta t_{\perp} = (2L_{\perp})^2/(2D_{\text{ub}})$, the time to diffuse to the confining walls and back.

In the case of the tube, the effective velocity is constant at large times, as, on average, a motor diffuses to the tube wall and back after walking its average walking distance along the filament. In the other two cases, however, the velocity keeps decreasing for large times, as larger and larger excursions away from the filament contribute to the observed behaviour. In both cases, the velocity decreases as a power law, $v(t) \sim t^{-1/2}$ in the slab and $v(t) \sim t^{-1}$ in the half space. Correspondingly, the displacement of the motors grows linearly with time in the tube, but slower than linearly in the other cases. In the slab, $x(t) \sim \sqrt{t}$ and in the half space $x(t) \sim \ln t$, see Fig. 3.2(a) and (c).

This long-time behaviour can be understood by a simple scaling argument. In the case of the tube, movements perpendicular to the filament are equilibrated at long times. Therefore the effective velocity is equal to the average velocity,

$$v = \frac{v_b P_b}{P_b + P_{\text{ub}}} = \frac{v_b}{1 + (\epsilon/\pi_{\text{ad}})\phi} \approx \frac{v_b}{(\epsilon/\pi_{\text{ad}})\phi}, \quad (3.1)$$

where the last expression holds for large tube cross-sections ϕ .¹ P_b is the probability that the motor is bound, given by $P_b = 1/\epsilon$, and P_{ub} is the probability that the motor is unbound, $P_{\text{ub}} = \phi/\pi_{\text{ad}}$. In these expressions, we have neglected a normalization constant, which, however, drops out again anyway. This expression for the velocity is exact, and we will rederive it later in this chapter in a more formal way.

In the half space and the slab, there is no defined cross-section, as motors can make excursions away from the filament of unrestricted length. However, at a time t , the motors cannot have made arbitrarily large excursions, as they have started bound to the filament. The space a motor has explored at time t is restricted by the diffusive length scale $L_{\text{diff}} = \sqrt{D_{\text{ub}}t}$, so that we can define an effective time-dependent cross-section of the space the motor has explored at time t . In the case of the slab, we obtain $\phi(t) \sim L_{\perp} L_{\text{diff}}$ and thus $v(t) \sim v_b/[(\epsilon/\pi_{\text{ad}})L_{\perp}\sqrt{D_{\text{ub}}t}] \sim 1/\sqrt{t}$, as observed in the simulations. In the half space geometry, diffusion is restricted along two directions by the diffusive length scale L_{diff} and thus, $\phi(t) \sim L_{\text{diff}}^2$ and $v(t) \sim v_b/[(\epsilon/\pi_{\text{ad}})D_{\text{ub}}t] \sim 1/t$.

The scaling argument can also be put into a slightly different form: To avoid complicated expressions, we consider a filament in d -dimensional space without confining walls, but the same argument holds for compartments of the same dimensionality, i.e. with $d-1$ dimensions of unrestricted diffusion. At large times the diffusive length scale $L_{\text{diff}} = \sqrt{D_{\text{ub}}t}$ is the only relevant length scale, therefore the probability distribution for the perpendicular coordinates of the motor, $P_{\perp}(\mathbf{y}, t)$, has the scaling form $P_{\perp}(\mathbf{y}, t) = \Phi(\mathbf{y}/L_{\text{diff}})/L_{\text{diff}}^{d-1}$, where the denominator is due to normalization and Φ is a dimensionless scaling function. Hence, the probability that the motor is bound, $P_b(t)$, and the velocity, $v = v_b P_b$, are given by $v(t) \sim P_b(t) \sim L_{\text{diff}}^{-(d-1)} \sim t^{-(d-1)/2}$. Let us mention that, for the case of geometries without confining walls, similar scaling arguments have previously been given by Ajdari [55].

Comparing the two variants of the model introduced in chapter 2.1.4, we want to point out, that for corresponding parameters, the displacements agree perfectly for large times. Differences can be seen at short times, where the discrete-time random walk in the bound state results in discrete steps, see Fig. 3.2(c).

¹Remember that we express all times and lengths in units of the basic time scale τ and the filament repeat distance ℓ , respectively.

Experimental realization

Let us finally discuss briefly the possibilities of experimental realizations of these random walks. Compartments like those discussed above can be realized using glass surfaces. As mentioned, the half space geometry is the standard geometry in single molecule experiments (bead assays) on molecular motors. Slab geometries with heights of $5\ \mu\text{m}$ have, for example, been used in experiments on aster formation [60]. Typical diameters of a glass tubes (used e.g. as micropipettes) are also in the order of a few μm . Alternatively, the confining walls could be surfaces of a liquid in fluid microchannels, see e.g. [79]. Again, such channels can have diameters down to a few μm .

Movements of motors in these compartments could be observed either by single particle tracking or by fluorescence microscopy of ensembles of fluorescently labeled motors. In the latter case, the average displacement and the positional variance could be obtained from the fluorescence intensity profiles. The second approach has presumably the advantage of yielding better statistics. (In the simulations with kinesin-like parameters, to obtain reasonable statistics, we had to average over at least 1000 motor trajectories.)

The time scales relevant to the random walks are experimentally accessible. The walking time Δt_b is typically of the order of one or a few seconds. The time to enter the geometry-dependent regime, Δt_\perp , depends, of course, both on the size of the compartment and the diffusion coefficient of the motor. In water, it is $\Delta t_\perp \simeq (L_\perp/\mu\text{m})^2$ s for kinesin motors carrying 100 nm-beads and $\Delta t_\perp \simeq 0.1 (L_\perp/\mu\text{m})^2$ s for kinesin without beads. In a tube of radius $10\ \mu\text{m}$ or a slab of height $10\ \mu\text{m}$, kinesin motors without beads thus enter the geometry-dependent regime after about 10 seconds and motors with beads after 1–2 minutes.

3.2 Analytical solution in two and three dimensions

In this section, we discuss the analytical solution of the master equations for the random walks of molecular motors in two and three dimensions without confining walls. We will explain the two-dimensional case in more detail and give only the main results of the three-dimensional case, which is technically more involved. This analytical work was done in collaboration with Theo Nieuwenhuizen and is presented in detail in Refs. [57, 80].

Analytical results are obtained by the following method, which is a variant of the method of Fourier–Laplace transforms for random walks in homogeneous space (see Ref. [66] and appendix B): By using Fourier–Laplace transforms of the probability distributions, the master equations of the random walk can be transformed into a set of algebraic equations, one of which, however, requires the solution of a non-trivial integral. Solving these algebraic equations, solutions for the Fourier–Laplace transformed probability distributions and their moments are obtained and closed expressions in terms of integrals can be derived for the time-dependent probability distributions and moments. These can, on the one hand, be evaluated numerically to obtain results for all times; on the other hand, asymptotic results for small and large times can be obtained fully analytically by using the Tauberian theorems. In this way, we derive the binding probability and effective velocities and diffusion coefficients for long times.

Let us finally mention that, apart from the proper value of analytical results, comparison of the exact results with simulation data allows us also to check the accuracy of our simulations. We anticipate at this point, that, for all quantities checked, agreement of simulations and analytical or semi-analytical results is very good.

3.2.1 The two-dimensional case

In the two-dimensional case the master equations (2.1) and (2.2) can be written as

$$P_n(t+1) = \alpha P_{n-1}(t) + \beta P_{n+1}(t) + \gamma P_n(t) + \frac{\pi_{\text{ad}}}{4} p_{n,1}(t) + \frac{\pi_{\text{ad}}}{4} p_{n,-1}(t) \quad (3.2)$$

$$p_{n,m}(t+1) = \frac{1}{4} \left[p_{n+1,m}(t) + p_{n-1,m}(t) + p_{n,m+1}(t) + p_{n,m-1}(t) \right] \quad (3.3)$$

$$p_{n,\pm 1}(t+1) = \frac{1}{4} \left[p_{n+1,\pm 1}(t) + p_{n-1,\pm 1}(t) + p_{n,\pm 2}(t) \right] + \frac{\epsilon}{4} P_n(t) + \frac{1 - \pi_{\text{ad}}}{4} p_{n,\pm 1}(t), \quad (3.4)$$

where the second equation holds for $m \neq 0, \pm 1$. Let us for the moment consider the case $\pi_{\text{ad}} = 1$, so that the last term in Eq. (3.4) vanishes. We will reintroduce π_{ad} in section 3.2.3. The initial conditions are chosen as $p_{n,m}(t=0) = \delta_{m,0} \delta_{n,0}$ or $P_0(t=0) = 1$, i.e., all motors start bound to the filament at site $n = 0$. By introducing the Fourier–Laplace transforms,

$$P(k, s) \equiv \sum_{t=0}^{\infty} \sum_{n=-\infty}^{\infty} \frac{e^{ikn}}{(1+s)^{t+1}} P_n(t) \quad (3.5)$$

$$p(q, k, s) \equiv \sum_{t=0}^{\infty} \sum_{n,m=-\infty}^{\infty} \frac{e^{ikn+iqm}}{(1+s)^{t+1}} p_{n,m}(t), \quad (3.6)$$

the master equations can be reduced to an algebraic equation

$$\left(1 + s - \frac{1}{2} \cos q - \frac{1}{2} \cos k \right) p(q, k, s) = 1 + \left[\left(\alpha - \frac{1}{4} \right) e^{ik} + \left(\beta - \frac{1}{4} \right) e^{-ik} + \gamma - \frac{1-\epsilon}{2} \cos q \right] P(k, s). \quad (3.7)$$

Here the first line is what one would get in the case of a simple symmetric random walk in two dimensions, and the second line corrects those terms that are changed by the presence of the filament. As an immediate consequence of this equation, we obtain an expression which relates the bound and unbound distributions, $P(k, s)$ and $p(q, k, s)$:

$$p(q, k, s) = \frac{1 + \left[\left(\alpha - \frac{1}{4} \right) e^{ik} + \left(\beta - \frac{1}{4} \right) e^{-ik} + \gamma - \frac{1-\epsilon}{2} \cos q \right] P(k, s)}{1 + s - \frac{1}{2} \cos q - \frac{1}{2} \cos k}. \quad (3.8)$$

A second condition follows from $P_n(t) = p_{n,0}(t)$,

$$P(k, s) = \frac{1}{2\pi} \int_0^{2\pi} dq p(q, k, s). \quad (3.9)$$

Inserting (3.8) and performing the integral (see appendix B.4), we obtain the explicit solution for the bound motors

$$\begin{aligned} P(k, s) &= \left[(1 - \epsilon)(1 + s - \frac{1}{2} \cos k) - \gamma - \left(\alpha - \frac{1}{4} \right) e^{ik} - \left(\beta - \frac{1}{4} \right) e^{-ik} + \frac{\epsilon}{2I_1^{(1)}(2 + 2s - \cos k)} \right]^{-1} \\ &= \left[(1 - \epsilon)(1 + s) - \gamma - i v_b \sin k - \left(\alpha + \beta - \frac{\epsilon}{2} \right) \cos k + \frac{\epsilon}{2} \sqrt{(2 + 2s - \cos k)^2 - 1} \right]^{-1} \\ &\approx \frac{1}{(1 - \epsilon)s - i v_b k + \epsilon \sqrt{s^2 + s}}, \end{aligned} \quad (3.10)$$

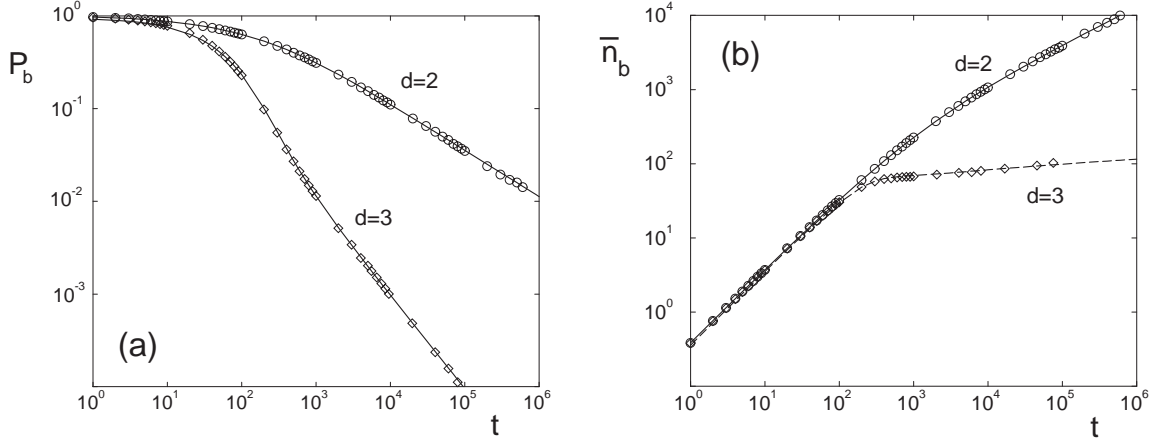


Figure 3.3: (a) Probability that a motor is bound to the filament, P_b , and (b) average position of bound motors, \bar{n}_b , as a function of time for the cases of two and three dimensions. Curves result from numerical evaluation of the closed analytical expressions, circles and diamonds are simulation data. The parameters for the hopping probabilities are $\alpha = 0.675$, $\beta = 0.3$, $\gamma = 0$ and $\epsilon = 0.05$.

where the bound-state velocity $v_b = \alpha - \beta$ has been inserted.² The last expression of (3.10) holds for small k and is correct up to linear order in k . The solution for the unbound motors is obtained by inserting (3.10) into Eq. (3.8).

Moments of the distribution of bound motors

On the one hand, the Fourier–Laplace transform can be inverted to obtain the full distribution of bound and unbound motors from Eqs. (3.10) and (3.8), see Refs. [57,80]. On the other hand, a lot of information about the moments of the distribution and their asymptotic behaviour can be obtained from Eq. (3.10) without calculating the full distributions.

For $k = 0$, Eq. (3.10) yields the zeroth moment of the distribution for the bound motors, which is the probability $P_b(t)$ that the motor is bound to the filament at a certain time, as $P_b(t) = \sum_n P_n(t) = P(k = 0, t)$:

$$P_b(s) = P(k = 0, s) = \frac{1}{(1 - \epsilon)s + \epsilon\sqrt{s^2 + s}}. \quad (3.11)$$

Inverting the Laplace transform, we obtain a closed expression for the probability that the motor is bound to the filament, which is exact at all times,

$$P_b(t) = \oint \frac{ds}{2\pi i} (1 + s)^t P(k = 0, s) = \int_0^{1/\epsilon^2} \frac{dy}{\pi \sqrt{y}} \frac{(1 - \epsilon^2 y)^{t+1/2}}{[1 + (1 - 2\epsilon)y]}. \quad (3.12)$$

²Note that this definition is slightly different from the one used in the previous chapter, where we had normalized the forward and backward hopping probabilities to the situation where no detachment occurs. The difference is, however, only of order ϵ and thus small for processive motors.

This closed expression can be evaluated numerically. Comparison to computer simulations shows perfect agreement, see Fig. 3.3(a).

The asymptotic behaviour for large times can be obtained fully analytically: From Eq. (3.11) we obtain

$$P_b(s) \approx \frac{1}{\epsilon\sqrt{s}} \quad (3.13)$$

for small s . Using the Tauberian theorems (see appendix B.3), the probability that the motor is bound, $P_b(t)$, is obtained for large t :

$$P_b(t) \approx \frac{1}{\sqrt{\pi\epsilon^2 t}}. \quad (3.14)$$

This result confirms the prediction of the scaling arguments, that the probability to be bound to the filament decreases as $t^{-1/2}$. Note that it defines a crossover time $t_* = 1/(\pi\epsilon^2)$, which is larger than the average time the motor is bound, $1/\epsilon$. This means that, though unbinding happens after a time of order $1/\epsilon$, a motor stays close to the filament for a time of order $1/\epsilon^2$.

In the same way, the linear order in k of Eq. (3.10) yields the first moment of the distribution of bound motors,

$$N_1(t) \equiv \sum_n n P_n(t) = \frac{2v_b(1-\epsilon)}{\pi\epsilon^2} \int_0^{\epsilon^{-2}} dy \frac{\sqrt{1-\epsilon^2 y}}{\sqrt{y}[1+y(1-2\epsilon)]^2} [1 - (1-\epsilon^2 y)^t]. \quad (3.15)$$

The average displacement of bound motors is given by $\bar{n}_b = N_1(t)/P_b(t)$. It is again evaluated numerically and compared with simulation results, showing very good agreement, see Fig. 3.3(b). For large times, we obtain

$$\bar{n}_b \approx \frac{v_b\sqrt{\pi t}}{\epsilon}, \quad (3.16)$$

in agreement with the scaling $\sim\sqrt{t}$ predicted by scaling arguments. Taking the derivative with respect to time, we can define an effective velocity, with which the distribution of bound motors advances,

$$\bar{v}_b \equiv \frac{\partial}{\partial t} \bar{n}_b \approx \frac{\sqrt{\pi}}{2} \frac{v_b}{\epsilon\sqrt{t}} = \frac{\pi}{2} P_b(t) v_b, \quad (3.17)$$

The last relation confirms the scaling $v_b(t) \sim v_b P_b(t)$, which has been assumed in the scaling approach. The effective velocity of the motors is reduced by a factor given by the probability that a motor is in the bound state. Let us mention, that the same happens in a simple two-state random walk, where motion is directed in one of the states only. In difference to the simple two-state random walk, however, this factor is time-dependent here. The factor $\pi/2$ is solely due to the fact that only the bound motors are considered. We will show below, that this factor is absent, if all, bound and unbound, motors are considered.

Finally, we obtain the positional variance Δn_b^2 from the quadratic order in k of Eq. (3.10). In this case the exact expression is a bit more complicated, but can again be evaluated numerically, see Fig. 3.4. Here we give only the asymptotics for large times,

$$\Delta n_b^2 \approx \frac{v_b^2(4-\pi)}{\epsilon^2} t. \quad (3.18)$$

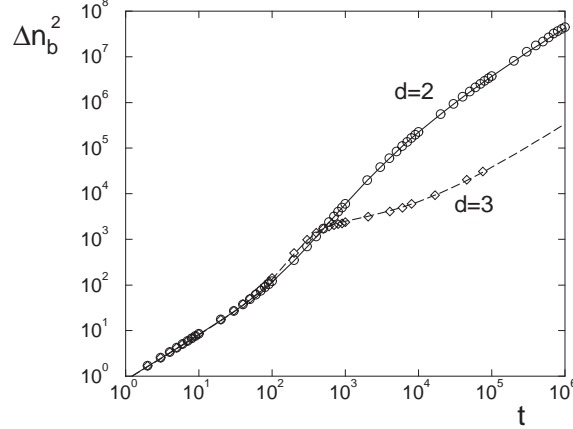


Figure 3.4: Positional variance Δn_b^2 of bound motors as a function of time. Parameters are as in Fig. 3.3.

From this result, we can derive an effective diffusion coefficient,

$$\bar{D}_b \equiv \frac{1}{2} \frac{\partial}{\partial t} \Delta n_b^2 \approx \frac{v_b^2(4 - \pi)}{2\epsilon^2}. \quad (3.19)$$

Note that this diffusion coefficient is large compared to both the diffusion coefficients of the bound and unbound state of the motors. Effective diffusion at large times will be discussed in more detail in section 3.5.

Moments of the distributions of unbound motors and all motors

The analogous analysis can be done for the unbound motors. We define $p_{\text{ub}}(q, k, s) \equiv p(q, k, s) - P(k, s)$. For small q , k and s , we obtain from Eq. (3.8):

$$p_{\text{ub}}(q, k, s) \approx \frac{4\epsilon\sqrt{s}}{(s - iv_b k + \epsilon\sqrt{s})(q^2 + 4s)}. \quad (3.20)$$

The first moment of the distribution of unbound motors is $N_1^{(\text{ub})} = \frac{v_b P_b(s)}{s} - N_1(s)$. For the average position of the unbound motors, we obtain at large times

$$\bar{n}_{\text{ub}}(t) \equiv \frac{N_1^{(\text{ub})}(t)}{1 - P_b(t)} \approx \frac{2v_b}{\sqrt{\pi}\epsilon} \sqrt{t}, \quad (3.21)$$

which has the same scaling as the position of the bound motors discussed above. Since for large times basically all motors are detached from the filament, Eq. (3.21) gives also the asymptotic displacement of all motors, i.e. for the case that averages are taken over bound and unbound motors, $\bar{n} = \bar{n}_b P_b + \bar{n}_{\text{ub}}(1 - P_b) \approx \bar{n}_{\text{ub}}$. The effective (time-dependent) velocity at large times is $v_b P_b(t)$, as predicted by scaling arguments. This can also be obtained by inspection of $N_1^{(\text{ub})}$: The displacement of all motors is given by

$$\bar{n} \equiv N_1(s) + N_1^{\text{ub}}(s) = v \frac{P_b(s)}{s}, \quad (3.22)$$

as the normalization factor for all motors is one. The effective velocity is obtained from the inverse:

$$v(t) = v_b \frac{d}{dt} \int \frac{ds}{2\pi i} \frac{e^{st} P_b(s)}{s} = v_b \int \frac{ds}{2\pi i} e^{st} P_b(s) = v_b P_b(t). \quad (3.23)$$

The large-time positional variance of the unbound motors grows with a large diffusion coefficient along the direction of the filament, $\bar{D}_{\parallel} \approx \frac{v_b^2(\pi-2)}{\pi\epsilon^2}$, as motors attach to the filament and are then driven away quickly. The variance in the direction perpendicular to the filament, Δm^2 , is obtained from the order q^2 of Eq. (3.8),

$$\Delta m^2 \approx \frac{t}{2} \left(1 - \frac{2}{\epsilon\sqrt{\pi t}} \right). \quad (3.24)$$

Diffusion perpendicular to the filament is initially suppressed, because motors remain bound to the filament, but for large times, the usual unbound diffusion coefficient $D_{\text{ub}} = 1/4$ is adopted, $\bar{D}_{\perp} \equiv \frac{1}{2} \frac{\partial}{\partial t} \Delta m^2 \approx D_{\text{ub}}[1 - P_b(t)]$.

3.2.2 The three-dimensional case

In the three-dimensional case, the solution is completely analogous, but technically more involved. We will give only a brief summary and refer the reader to Refs. [57, 80] for more details.

The master equations for this case are:

$$P_n(t+1) = \alpha P_{n-1}(t) + \beta P_{n+1}(t) + \gamma P_n(t) + \frac{\pi_{\text{ad}}}{6} \sum_{\mathbf{i}} p_{n,\mathbf{i}}(t) \quad (3.25)$$

$$p_{n,\mathbf{m}}(t+1) = \frac{1}{6} \left(p_{n+1,\mathbf{m}}(t) + p_{n-1,\mathbf{m}}(t) + \sum_{\mathbf{i}} p_{n,\mathbf{m}+\mathbf{i}}(t) \right) \quad (3.26)$$

$$p_{n,\mathbf{j}}(t+1) = \frac{1}{6} \left(p_{n+1,\mathbf{j}}(t) + p_{n-1,\mathbf{j}}(t) + \sum_{\mathbf{i} \neq \mathbf{j}} p_{n,\mathbf{j}-\mathbf{i}}(t) \right) + \frac{\epsilon}{6} P_n(t) + \frac{1 - \pi_{\text{ad}}}{6} p_{n,\mathbf{j}}(t). \quad (3.27)$$

Here Eq. (3.26) holds for $\mathbf{m} \neq (0, 0), (0, \pm 1), (\pm 1, 0)$ and Eq. (3.27) for $\mathbf{j} = (0, \pm 1), (\pm 1, 0)$. The summations run over the perpendicular neighbour sites of a filament site, $\mathbf{i} = (0, \pm 1), (\pm 1, 0)$. We consider again the case $\pi_{\text{ad}} = 1$. As in the two-dimensional case, we use Fourier–Laplace transforms, but now we have an additional Fourier transform for the second dimension perpendicular to the filament. We obtain

$$p(\mathbf{q}, k, s) = \frac{1 + [(\alpha - \frac{1}{6})e^{ik} + (\beta - \frac{1}{6})e^{-ik} + \gamma - \frac{1-\epsilon}{3}(\cos q_1 + \cos q_2)] P(k, s)}{1 + s - \frac{1}{3} \cos k - \frac{1}{3} \cos q_1 - \frac{1}{3} \cos q_2}. \quad (3.28)$$

Integrating over q_1 and q_2 (see appendix B.4), we get the exact solution

$$P(k, s) = \left[(1 - \epsilon)(1 + s - \frac{1}{3} \cos k) - \gamma - (\alpha - \frac{1}{6})e^{ik} - (\beta - \frac{1}{6})e^{-ik} + \epsilon \mathcal{J}(s, k) \right]^{-1} \approx \frac{1}{(1 - \epsilon)s - iv_b k + \epsilon \mathcal{J}(s, k=0)} \quad (3.29)$$

with

$$\mathcal{J}(s, k) = \frac{1}{3I_1^{(2)}(3 + 3s - \cos k)} = \frac{\pi(1 + s - \frac{1}{3}\cos k)}{2K(\frac{4}{(3+3s+\cos k)^2})}. \quad (3.30)$$

The last expression in Eq. (3.29) holds for small s and k and is exact up to linear order in k . As in the two-dimensional case, we derive closed expressions for the moments of the distributions of bound and unbound motors by expanding Eqs. (3.29) and (3.28) in k and \mathbf{q} . These are again evaluated numerically and agree well with simulation results, see Figs. 3.3 and 3.4. In addition, solutions for large times can be obtained analytically using the Tauberian theorems and the asymptotic behaviour of the elliptic integral $K(m) \approx \frac{1}{2} \ln \frac{16}{1-m}$ for m close to one [81]. In the following, we briefly summarize the main results.

The binding probability now decreases as $1/t$ as expected from scaling arguments. The exact solution for large times is

$$P_b(t) \approx \frac{3}{2\pi\epsilon t}. \quad (3.31)$$

Note that, unlike in two dimensions, the crossover time $t_* = 3/(2\pi\epsilon)$ is now of order $1/\epsilon$, i.e., if a motor detaches from the filament, it is likely, that the motor diffuses away immediately, while for $d = 2$ quick rebinding is quite probable.

The average displacement of the bound motors in the three-dimensional case is given by

$$\bar{n}_b(t) \approx \frac{3v_b}{\pi\epsilon} \ln t \quad (3.32)$$

at large times. The corresponding result for the unbound motors has an additional factor $1/2$. Again, the result for the unbound motors is equal to the one for all (bound and unbound) motors at large times and the corresponding velocity is given by $3v_b/(2\pi\epsilon t) = v_b P_b(t)$ in agreement with the prediction of scaling arguments.

Finally, at large times, the positional variances of bound and unbound motors in direction parallel to the filament behave to leading order as if there was no filament, but exhibit large logarithmic corrections of order $(v_b/\epsilon)^2$:

$$\Delta n_b^2(t) \approx \frac{t}{3} + \frac{3v_b^2}{2\pi^2\epsilon^2} \ln^2 t, \quad \Delta n_{ub}^2(t) \approx \frac{t}{3} + \frac{3v_b^2}{4\pi^2\epsilon^2} \ln^2 t. \quad (3.33)$$

Note that the linear term is equal to $2D_{ub}t$, as $D_{ub} = 1/6$. Diffusion in directions perpendicular to the filament is again suppressed at the beginning, but reaches asymptotically its unperturbed value as if there was no filament, $\Delta m_1^2 = \Delta m_2^2 \approx \frac{t}{3}(1 - \frac{3\ln t}{2\pi\epsilon t})$. The relation $\bar{D}_\perp \approx D_{ub}[1 - P_b(t)]$ holds in this case as well.

3.2.3 Sticking probability

We now reinclude the variable sticking probability in our model: If a motor reaches the filament, it rebinds to it with a probability π_{ad} , while it is reflected from the filament with probability $1 - \pi_{ad}$. Such a behaviour might, for example, be due to steric constraints, if, e.g., a motor with attached bead diffuses close to the filament, but with the bead between the motor and the filament. In the long time regime, it is expected from our scaling argument that the introduction of this additional parameter reduces the probability that a motor is bound to the filament and thus the effective time-dependent velocity by a factor π_{ad} . This expectation is confirmed by simulations. In the following, we derive this result analytically.

The two-dimensional case

Let us begin with the simpler case $d = 2$ and consider Eqs. (3.2)–(3.4) for arbitrary values of π_{ad} . On the lines $m = \pm 1$ the rate for hopping to $m = 0$, i.e. to the filament is now $\pi_{\text{ad}}/4$, while there is a rate $(1 - \pi_{\text{ad}})/4$ not to jump. We use again Fourier–Laplace transforms. The equivalent of Eq. (3.7) now contains an additional term with $p_1(k, s)$, the Fourier–Laplace transform of $p_{n,1}(t)$:

$$(1 + s - \frac{1}{2} \cos q - \frac{1}{2} \cos k)p(q, k, s) = 1 + \frac{1 - \pi_{\text{ad}}}{2}(1 - \cos q)p_1(k, s) \\ + [\gamma + (\alpha - \frac{1}{4})e^{ik} + (\beta - \frac{1}{4})e^{-ik} - \frac{1 - \epsilon}{2} \cos q]P(k, s). \quad (3.34)$$

$P(k, s)$ and $p_1(k, s)$ are related via the Fourier–Laplace transform of Eq. (3.2),

$$p_1(k, s) = \frac{2}{\pi_{\text{ad}}} \left(1 - [1 + s - \alpha e^{-ik} - \beta e^{ik} - \gamma]P(k, s) \right). \quad (3.35)$$

Using this expression for $p_1(k, s)$, we can proceed in the same way as above and obtain

$$P(k, s) = \frac{1 + \frac{1 - \pi_{\text{ad}}}{\pi_{\text{ad}}}(1 - \Psi)}{[s + (1 - \gamma)(1 - \cos k) + \frac{\epsilon}{2} \cos k - iv \sin k][1 + \frac{1 - \pi_{\text{ad}}}{\pi_{\text{ad}}}(1 - \Psi)] - \frac{\epsilon}{2}\Psi} \quad (3.36)$$

with $\Psi \equiv \frac{I_2^{(1)}(2+2s-\cos k)}{I_1^{(1)}(2+2s-\cos k)}$. For small k and s , this expression can be approximated by

$$P(k, s) \approx \frac{1}{(1 - \frac{\epsilon}{\pi_{\text{ad}}})s - iv_b k + \frac{\epsilon}{\pi_{\text{ad}}} \sqrt{s(s+1)}}, \quad (3.37)$$

which has exactly the same form as Eq. (3.10), but with an effective detachment rate ϵ/π_{ad} . Likewise, we find for the unbound motors

$$p_{\text{ub}}(q, k, s) \approx \frac{4\epsilon\sqrt{s}}{(s - iv_b k + \frac{\epsilon}{\pi_{\text{ad}}}\sqrt{s})(q^2 + 4s)}, \quad (3.38)$$

corresponding to Eq. (3.20). Hence, in the long-time regime, the only effect of the sticking probability π_{ad} is a rescaling of the detachment rate. Thus the probability for a motor to be bound to the filament decays as $P_b(t) \approx \pi_{\text{ad}}/(\sqrt{\pi\epsilon})t^{-1/2}$ for large times and the average displacement grows as $\bar{n}(t) \approx 2v_b\pi_{\text{ad}}/(\epsilon\pi^{1/2})\sqrt{t}$, i.e., both quantities are reduced by a factor π_{ad} as expected from the scaling approach.

The three-dimensional case

For $d = 3$ the calculation is completely analogous. $p(\mathbf{q}, k, s)$, $p_1(k, s)$ and $P(k, s)$ are related via

$$p_1(k, s) = \frac{3}{2\pi_{\text{ad}}} \left(1 + [\alpha e^{-ik} + \beta e^{ik} + \gamma - 1 - s]P(k, s) \right) \quad (3.39)$$

and

$$p(\mathbf{q}, k, s) = \frac{1 + [\gamma + (\alpha - \frac{1}{6})e^{ik} + (\beta - \frac{1}{6})e^{-ik} - \frac{1 - \epsilon}{3}(\cos q_1 + \cos q_2)]P(k, s)}{1 + s - \frac{1}{3} \cos r - \frac{1}{3} \cos q_1 - \frac{1}{3} \cos q_2} \\ + \frac{\frac{1 - \pi_{\text{ad}}}{3}[2 - \cos q_1 - \cos q_2]p_1(k, s)}{1 + s - \frac{1}{3} \cos k - \frac{1}{3} \cos q_1 - \frac{1}{3} \cos q_2}. \quad (3.40)$$

From these two equations we obtain a rather complicated expression for $P(k, s)$, which for small s and k reduces to

$$P(k, s) \approx \frac{1}{s - iv_b k + (\epsilon/\pi_{\text{ad}})\mathcal{J}(s)}. \quad (3.41)$$

This equation differs from the corresponding result for the case $\pi_{\text{ad}} = 1$, Eq. (3.29), only by a rescaling of the detachment rate, as in the two-dimensional case discussed above. The same is true for the distribution of unbound motors.

Therefore we can conclude, that in both two and three dimensions, the long-time displacement and the probability to be bound to the filament are reduced by a factor π_{ad} , as these quantities are proportional to $1/\epsilon$.

3.3 Return to the filament and asymptotic displacement

To obtain some more insight into the nature of the anomalous drift velocities, let us discuss another approach to estimate the asymptotic behaviour. If we are only interested in the mean displacement parallel to the filament, we can consider the excursions away from the filament as periods of rest. The long-time behaviour of the displacement is then given by effective 'steps', periods during which the motor advances quickly over a distance $x_s \sim v_b/\epsilon$, and waiting periods between these 'steps'. The waiting times τ_w are distributed according to a distribution $\psi(\tau_w)$, which is given by the distribution of return times to the filament. The distribution of return times to a line in d dimensions is equivalent to the distribution of return times to the origin in $d - 1$ dimensions, which is a classical problem in the theory of random walks, solved by Polya in 1921 [82].

Introducing the Laplace transform of the waiting time distribution,

$$\psi(s) \equiv \int_0^\infty dt \psi(t) e^{-st}, \quad (3.42)$$

a simple relation for the asymptotic mean displacement of the motor can be given [83], which follows directly from the general solution of continuous time random walks on a homogeneous lattice, see Appendix B,

$$x(s) \approx \frac{x_s \psi(s)}{s[1 - \psi(s)]}, \quad (3.43)$$

from which the displacement for large times can be obtained by inverting the Laplace transform. Hence, we can determine the asymptotic displacement as a function of time, if we know the large-time (or small s) behaviour of the waiting time distribution $\psi(\tau_w)$, which is equal to the distribution of return times to the origin in $d - 1$ dimensions. The physical significance of Eq. (3.43) is, that the displacement at large times is determined by the long-time tails of the waiting time distribution $\psi(\tau_w)$. Normal drift is obtained, as long as $\psi(\tau_w)$ has a finite mean value, $\bar{\tau}_w$, and thus $\psi(s) \approx 1 + \bar{\tau}_w s$ for small s . This is the case, if, e.g., the waiting time distribution decays exponentially for large τ_w . If, however, $\psi(\tau_w)$ decays slower than $\sim \tau_w^{-2}$, the mean waiting time diverges, corresponding to a divergence of $[\psi(s) - 1]/s$ for small s , and anomalous drift is obtained, i.e., the average displacement $x(t)$ grows slower than linearly with time. This behaviour occurs in our case, where waiting times are given by return times to the filament.

A short summary of the derivation of the return time distributions will be given in Appendix B for the two cases $d = 2$ and $d = 3$. Let us now consider the asymptotic displacement:

In two dimensions, the waiting time distribution behaves as $\psi(\tau_w) \approx 1/(2\sqrt{\pi}\tau_w^{3/2})$ for large τ_w . The corresponding asymptotic behaviour of the Laplace transform is $\psi(s) \approx 1 - \sqrt{s}$ for small s . Inserting this into Eq. (3.43) and using the Tauberian theorem, we obtain

$$x(s) \approx \frac{x_s}{s^{3/2}} = \frac{v_b}{\epsilon s^{3/2}} \quad \text{and} \quad x(t) \approx \frac{2x_s\sqrt{t}}{\sqrt{\pi}} = \frac{2v_b\sqrt{t}}{\epsilon\sqrt{\pi}}. \quad (3.44)$$

Similarly, in the three-dimensional case, the waiting time distribution is $\psi(\tau_w) \approx 2\pi/(3\tau_w \ln^2 \tau_w)$ for large τ_w or $\psi(s) \approx 1 - 2\pi/(3 \ln s^{-1})$ for small s . Inserting again into Eq. (3.43), we obtain

$$x(s) \approx \frac{3x_s \ln s^{-1}}{2\pi s} = \frac{3v_b \ln s^{-1}}{2\pi\epsilon s} \quad \text{and} \quad x(t) \approx \frac{3x_s}{2\pi} \ln t = \frac{3v_b}{2\pi\epsilon} \ln t. \quad (3.45)$$

Both results agree exactly with the asymptotic results from the exact solution of the full master equations presented above.³

3.4 Continuum model and open compartments

The continuum equations for the random walks of tracer motors can be treated in a similar way and yield the same results as the lattice model. However, the continuum description is more flexible in terms of boundary conditions. We thus use it, after recovering the main results of the lattice model for the two- and three-dimensional cases discussed in the previous sections, to derive analytical solutions for open compartments as the ones discussed above.

3.4.1 The two-dimensional case

We start with the idealized two-dimensional case, rederiving the results of the lattice model. The diffusion equations corresponding to Eqs. (2.11) and (2.12) for the two-dimensional case are

$$\frac{\partial p}{\partial t} = D_{\text{ub}}\Delta p + \delta(y) [\tilde{\epsilon}P - \tilde{\pi}_{\text{ad}}p_0] \quad (3.46)$$

$$\frac{\partial P}{\partial t} = -v_b \frac{\partial P}{\partial x} + D_b \frac{\partial^2 P}{\partial x^2} - \tilde{\epsilon}P + \tilde{\pi}_{\text{ad}}p_0, \quad (3.47)$$

where Δ is the two-dimensional Laplace operator and $p_0(x, t) = \ell p(x, y = 0, t)$. We will, in the following, express again all lengths in units of ℓ .

These equations can be solved in a completely analogous way to the lattice equations by using (now continuous) Fourier–Laplace transforms. The transformed equations are

$$sp(k, q, s) = -D_{\text{ub}}(k^2 + q^2)p(k, q, s) + \tilde{\epsilon}P(k, s) - \tilde{\pi}_{\text{ad}}p_0(k, s) \quad (3.48)$$

$$sP(k, s) = 1 + iv_b kP(k, s) - D_b k^2 P(k, s) - \tilde{\epsilon}P(k, s) + \tilde{\pi}_{\text{ad}}p_0(k, s). \quad (3.49)$$

Eq. (3.48) can be integrated over the transversal momentum q :

$$\begin{aligned} p_0(k, s) &= \int_{-\infty}^{\infty} \frac{dq}{2\pi} p(k, q, s) = \int_{-\infty}^{\infty} \frac{dq}{2\pi} \frac{\tilde{\epsilon}P - \tilde{\pi}_{\text{ad}}p_0}{s + D_{\text{ub}}(k^2 + q^2)} \\ &= (\tilde{\epsilon}P - \tilde{\pi}_{\text{ad}}p_0) \frac{1}{2\pi} \frac{1}{\sqrt{s + D_{\text{ub}}k^2} \sqrt{D_{\text{ub}}}} \int_{-\infty}^{\infty} \frac{d\tilde{q}}{1 + \tilde{q}^2}. \end{aligned} \quad (3.50)$$

³In principle, they could differ by a numerical factor, because we did not specify the short-time behaviour, which determines the effective ‘step’ size x_s .

The last integral is π , so we obtain

$$p_0(k, s) = \frac{\tilde{\epsilon}P(k, s)}{2\sqrt{s + D_{\text{ub}}k^2}\sqrt{D_{\text{ub}}} + \tilde{\pi}_{\text{ad}}} \quad (3.51)$$

and

$$\begin{aligned} P(k, s) &= \left(s - iv_{\text{b}}k + D_{\text{b}}k^2 + \tilde{\epsilon} - \frac{\tilde{\epsilon}\tilde{\pi}_{\text{ad}}}{2\sqrt{s + D_{\text{ub}}k^2}\sqrt{D_{\text{ub}}} + \tilde{\pi}_{\text{ad}}} \right)^{-1} \\ &\approx \left(s - iv_{\text{b}}k + \frac{2\tilde{\epsilon}}{\tilde{\pi}_{\text{ad}}}\sqrt{D_{\text{ub}}s} \right)^{-1}, \end{aligned} \quad (3.52)$$

where the second expression holds for small s and k . For $k = 0$, we obtain the binding probability

$$P_{\text{b}}(s) \equiv P(k = 0, s) \approx \left(s + \tilde{\epsilon} \frac{2\sqrt{D_{\text{ub}}}\sqrt{s}}{\tilde{\pi}_{\text{ad}}} \right)^{-1} \approx \frac{\tilde{\pi}_{\text{ad}}}{2\sqrt{D_{\text{ub}}}\sqrt{s}\tilde{\epsilon}}, \quad (3.53)$$

therefore the probability that a motor is bound to the filament decays at large times as

$$P_{\text{b}}(t) \equiv P(k = 0, t) \approx \frac{\tilde{\pi}_{\text{ad}}}{2\tilde{\epsilon}\sqrt{\pi}\sqrt{D_{\text{ub}}t}}. \quad (3.54)$$

If we express $\tilde{\pi}_{\text{ad}}$, $\tilde{\epsilon}$ and D_{ub} in terms of the parameters of the lattice model, we recover exactly the result obtained by the lattice calculation.

3.4.2 The three-dimensional case

In the three-dimensional case the continuum equations are given by Eqs. (2.11) and (2.12):

$$\frac{\partial p}{\partial t} = D_{\text{ub}}\Delta p + \delta(\mathbf{y})[\tilde{\epsilon}P - \tilde{\pi}_{\text{ad}}p_0] \quad (3.55)$$

$$\frac{\partial P}{\partial t} = -v_{\text{b}}\frac{\partial P}{\partial x} + D_{\text{b}}\frac{\partial^2 P}{\partial x^2} - \tilde{\epsilon}P + \tilde{\pi}_{\text{ad}}p_0, \quad (3.56)$$

where Δ is now the three-dimensional Laplace operator. We use again the Fourier–Laplace transformed form of these equations,

$$sp(k, \mathbf{q}, s) = -D_{\text{ub}}(k^2 + q_1^2 + q_2^2)p(k, \mathbf{q}, s) + \tilde{\epsilon}P(k, s) - \tilde{\pi}_{\text{ad}}p_0(k, s) \quad (3.57)$$

$$sP(k, s) = 1 + iv_{\text{b}}kP(k, s) - D_{\text{b}}k^2P(k, s) - \tilde{\epsilon}P(k, s) + \tilde{\pi}_{\text{ad}}p_0(k, s). \quad (3.58)$$

Doing the same steps as above, we get

$$\begin{aligned} p_0(k, s) &= \int_{-\infty}^{\infty} \frac{dq_1}{2\pi} \frac{dq_2}{2\pi} p(k, \mathbf{q}, s) = \int_{-\infty}^{\infty} \frac{dq_1}{2\pi} \frac{dq_2}{2\pi} \frac{\tilde{\epsilon}P - \tilde{\pi}_{\text{ad}}p_0}{s + D_{\text{ub}}(k^2 + q_1^2 + q_2^2)} \\ &= (\tilde{\epsilon}P - \tilde{\pi}_{\text{ad}}p_0) \int_0^{\infty} \frac{dq}{2\pi} \frac{q}{s + D_{\text{ub}}k^2 + D_{\text{ub}}q^2} = \frac{\tilde{\epsilon}P - \tilde{\pi}_{\text{ad}}p_0}{2\pi D_{\text{ub}}} \int_0^{\infty} d\tilde{q} \frac{\tilde{q}}{1 + \tilde{q}^2}. \end{aligned} \quad (3.59)$$

The problem with this expression is that the last integral diverges. This divergence is due to the fact that in the three-dimensional continuum model, to return to the filament, a point-like motor has to return to a line without thickness, hence it can pass the filament arbitrarily closely without taking note of it. Return to the line is thus not certain as on the lattice. To

obtain a convergent integral, we introduce a cutoff q_c as the upper integration limit. This cutoff corresponds to a certain range of attraction or thickness of the filament or a size of the motor. Defining

$$I \equiv \int_0^{\tilde{q}_c} d\tilde{q} \frac{\tilde{q}}{1+\tilde{q}^2} = \frac{1}{2} \ln(1+\tilde{q}_c^2) \quad \text{with} \quad \tilde{q}_c = \sqrt{\frac{D_{\text{ub}}}{s + D_{\text{ub}}k^2}} q_c, \quad (3.60)$$

we obtain

$$p_0 = \frac{\tilde{\epsilon}P}{2\pi I^{-1} + \tilde{\pi}_{\text{ad}}}. \quad (3.61)$$

Hence we obtain for the probability density on the filament

$$\begin{aligned} P(k, s) &= \left(s - iv_b k + D_b k^2 + \tilde{\epsilon} - \frac{\tilde{\epsilon}\tilde{\pi}_{\text{ad}}}{2\pi I^{-1} + \tilde{\pi}_{\text{ad}}} \right)^{-1} \\ &\approx \left(s - iv_b k + \frac{\tilde{\epsilon}}{\tilde{\pi}_{\text{ad}}} \frac{4\pi D_{\text{ub}}}{\ln(D_{\text{ub}}q_c^2 s^{-1})} \right)^{-1}, \end{aligned} \quad (3.62)$$

where the second expression holds for small s and k .

For $k = 0$, the binding probability is obtained, which asymptotically behaves as

$$P(k = 0, s) \approx \frac{\tilde{\pi}_{\text{ad}}[\ln(D_{\text{ub}}q_c^2) - \ln s]}{4\pi\tilde{\epsilon}D_{\text{ub}}}. \quad (3.63)$$

For arbitrary, but finite cutoff q_c the term containing q_c can be neglected for sufficiently small s , so that for sufficiently large t , the binding probability decays as

$$P(k = 0, t) \approx \frac{\tilde{\pi}_{\text{ad}}}{4\pi\tilde{\epsilon}D_{\text{ub}}t}. \quad (3.64)$$

Reinserting the parameters of the lattice model, the previous result is again recovered.

3.4.3 Open compartments

Let us now consider the solutions of the continuum equations for the motor's random walk in open compartments, as the ones studied above using computer simulations and scaling arguments. We derive the long-time behaviour of the binding probability, from which we obtain the crossover times for the entry into the geometry-dependent long-time regime.

Half space

The case of the half space is the simplest one. It can be treated by the method of reflection and superposition, see e.g. Ref. [84]: Since the diffusion equations (3.55) and (3.56) are linear differential equations, we can think of the part of the three-dimensional solution for $y_2 < 0$ as being reflected at the surface, so that a superposition of $p(y_2)$ with $p(-y_2)$ is obtained. This superposition fulfills the boundary condition

$$\frac{\partial p}{\partial y_2} = 0 \quad \text{at} \quad y_2 = 0. \quad (3.65)$$

As the density profile is symmetric under reflection at the plane $y_2 = 0$, the solution for the half space is twice the solution for the full three-dimensional space. This factor two carries over to the bound profile and hence to the velocity and displacement.

Slab

Let us start with a slab of height $2L_\perp$, where the filament is located at $y_1 = y_2 = 0$ in the middle of the slab. The case where the filament is fixed to the surface of the slab will then be deduced by reflection and superposition. In the slab we have the boundary conditions

$$\frac{\partial p}{\partial y_2} = 0 \quad \text{at} \quad y_2 = \pm L_\perp. \quad (3.66)$$

Equivalently, we can consider periodic boundary conditions at $y_2 = \pm L_\perp$ instead of the reflecting ones. In this case, we can expand the unbound density into a Fourier series,

$$p(\dots, y_2) = \frac{1}{2L_\perp} \sum_{j=-\infty}^{\infty} p(\dots, \omega_j) e^{i\omega_j y_2} \quad (3.67)$$

with $\omega_j = \frac{2\pi j}{2L_\perp}$. Here and in the following we use the symbol ω for discrete and q for continuous momentum variables. Using this Fourier series and doing the Fourier and Laplace transforms for the other variables in the same way as above, the equations of the three-dimensional case remain valid, if q_2 is replaced by ω_j . Eq. (3.59) becomes then

$$p_0(s, k) = \int_{-\infty}^{\infty} \frac{dq_1}{2\pi} \frac{1}{2L_\perp} \sum_{j=-\infty}^{\infty} p(k, q_1, \omega_j, s). \quad (3.68)$$

Inserting the expression for $p(k, q_1, \omega_j, s)$ and integrating out q_1 , we obtain

$$p_0(s, k) = \frac{\tilde{\epsilon}P - \tilde{\pi}_{\text{ad}}p}{4L_\perp \sqrt{D_{\text{ub}}}} \left(\frac{1}{\sqrt{s + D_{\text{ub}}k^2}} + 2 \sum_{j=1}^{\infty} \frac{1}{\sqrt{s + D_{\text{ub}}k^2 + D_{\text{ub}}\omega_j^2}} \right). \quad (3.69)$$

We approximate the sum in the last term by an integral,

$$S(k, s) \equiv \sum_{j=1}^{\infty} \frac{1}{\sqrt{s + D_{\text{ub}}k^2 + D_{\text{ub}}\omega_j^2}} \simeq \frac{L_\perp}{\pi} \int_{\pi/L_\perp}^{\infty} d\omega \frac{1}{\sqrt{s + D_{\text{ub}}k^2 + D_{\text{ub}}\omega^2}}. \quad (3.70)$$

To prevent the integral from diverging, we introduce again a cutoff ω_c corresponding to the range of attraction of the filament or the size of the motors. We then obtain

$$S = \frac{1}{\sqrt{D_{\text{ub}}}} \ln \left(\omega_c + \sqrt{\frac{s + D_{\text{ub}}k^2}{D_{\text{ub}}} + \omega_c^2} \right) - \frac{1}{\sqrt{D_{\text{ub}}}} \ln \left(\frac{\pi}{L_\perp} + \sqrt{\frac{s + D_{\text{ub}}k^2}{D_{\text{ub}}} + \frac{\pi^2}{L_\perp^2}} \right) \quad (3.71)$$

and the bound density follows as

$$P(k, s) = \left[s - iv_b k + D_b k^2 + \tilde{\epsilon} - \tilde{\epsilon} \tilde{\pi}_{\text{ad}} \left(\tilde{\pi}_{\text{ad}} + \frac{4L_\perp D_{\text{ub}}}{\sqrt{\frac{D_{\text{ub}}}{s + D_{\text{ub}}k^2} + \frac{2L_\perp}{\pi} \sqrt{D_{\text{ub}} S(k, s)}}} \right)^{-1} \right]^{-1}. \quad (3.72)$$

For large scales this expression can be simplified. The range of attraction of the filament can be assumed to be small compared to the slab height. We therefore consider the case where

$s/(D_{\text{ub}}\omega_c^2) \ll 1$. In this case the first logarithmic term in $S(k, s)$ can be neglected. We also neglect terms of quadratic order in k .

If $s \gg D_{\text{ub}}(\pi/L_{\perp})^2$ or $t \ll (L_{\perp}/\pi)^2/D_{\text{ub}}$, i.e., if motors have not yet reached the boundaries of the slab, we can consider L_{\perp} as infinite, in this case the term $\sim \sqrt{s}$ is small compared to the logarithm, and we obtain

$$P(k, s) \approx \left[s - iv_{\text{b}}k + \frac{\tilde{\epsilon}}{\tilde{\pi}_{\text{ad}}} \frac{4\pi D_{\text{ub}}}{\ln s^{-1}} \right]^{-1}, \quad (3.73)$$

which is the result of the three-dimensional case discussed above, as it should be. For larger times, $t \gg (L_{\perp}/\pi)^2/D_{\text{ub}}$ or $s \ll D_{\text{ub}}(\pi/L_{\perp})^2$, the square root term is dominating and the logarithm can be neglected in Eq. (3.72). In this case we obtain,

$$P(k, s) \approx \left[s - iv_{\text{b}}k + \frac{\tilde{\epsilon}}{\tilde{\pi}_{\text{ad}}} 4L_{\perp} \sqrt{D_{\text{ub}}s} \right]^{-1}, \quad (3.74)$$

which is the two-dimensional result with an effective reattachment rate $\tilde{\pi}_{\text{ad}}/(2L_{\perp})$. The probability to be bound to the filament (and also the long-time velocity $v_{\text{b}}P_{\text{b}}$) therefore decays for large times as

$$P_{\text{b}}(t) \approx \begin{cases} \tilde{\pi}_{\text{ad}}/(4\pi\tilde{\epsilon}D_{\text{ub}}t) & \text{for } t \ll t_{**} \\ \tilde{\pi}_{\text{ad}}/(4L_{\perp}\tilde{\epsilon}\sqrt{\pi}\sqrt{D_{\text{ub}}t}) & \text{for } t \gg t_{**} \end{cases} \quad (3.75)$$

with the crossover time $t_{**} = L_{\perp}^2/(\pi D_{\text{ub}})$, which differs from the one defined above, Δt_{\perp} , by a numerical factor.

Finally, let us come back to the case, where the filament is located directly on the lower surface at $y_2 = 0$. The upper surface is still located at $y_2 = L_{\perp}$. This case can be obtained from the results derived above by reflection and superposition analogously to the case of the half space and the densities are just the ones for the case above multiplied by an additional factor of two. Therefore also the probability of being bound to the filament and the displacement are twice the results calculated above.

Tube

Finally, we consider the tube geometry, where diffusion in all directions perpendicular to the filament is restricted by walls. For simplicity, we start with a tube with quadratic cross-section. The boundary conditions are

$$\frac{\partial p}{\partial y_i} = 0 \quad \text{at } y_i = \pm L_{\perp} \quad (i = 1, 2). \quad (3.76)$$

In this case we have discrete momenta $\omega_{1,i}$ and $\omega_{2,j}$ corresponding to the transverse coordinates y_1 and y_2 , and Eq. (3.59) is now replaced by

$$p_0(s, k) = \frac{1}{(2L_{\perp})^2} \sum_{i,j=-\infty}^{\infty} p(k, \omega_{1,i}, \omega_{2,j}, s). \quad (3.77)$$

As in the case of the slab, we approximate the double sum by the term for $i = j = 0$ plus an integral,

$$p_0(s, k) = \frac{1}{(2L_{\perp})^2} (\tilde{\epsilon}P - \tilde{\pi}_{\text{ad}}p_0) \left(\frac{1}{D_{\text{ub}}k^2 + s} + \frac{L_{\perp}^2}{D_{\text{ub}}\pi^2} \int_{\pi/L_{\perp}}^{\omega_c} d\omega \frac{2\pi\omega}{D_{\text{ub}}(k^2 + \omega^2) + s} \right), \quad (3.78)$$

where we have again introduced a cutoff ω_c , and after some steps we obtain

$$P(k, s) \approx \left\{ s - iv_b k + \frac{4L_\perp^2 \tilde{\epsilon}}{\tilde{\pi}_{\text{ad}}} \left(s^{-1} + \frac{L_\perp^2}{\pi D_{\text{ub}}} \left[\ln\left(1 + \frac{D_{\text{ub}} \omega_c^2}{s}\right) - \ln\left(1 + \frac{D_{\text{ub}} \pi^2}{L_\perp^2 s}\right) \right] \right)^{-1} \right\}^{-1}, \quad (3.79)$$

which holds for small s and k . For $s \gg D_{\text{ub}}(\pi/L_\perp)^2$, i.e., if motors have not yet reached the boundaries, this expression yields again the solution for the three-dimensional case without confining walls, as the dominating term is the logarithm containing ω_c . If $s \ll D_{\text{ub}}(\pi/L_\perp)^2$, i.e. for times large compared to L_\perp^2/D_{ub} , the logarithms can be neglected and we get

$$P(k, s) \approx \left[s \left(1 + 4L_\perp^2 \frac{\tilde{\epsilon}}{\tilde{\pi}_{\text{ad}}} \right) - iv_b k \right]^{-1}. \quad (3.80)$$

Thus the probability to be bound to the filament is constant for large times

$$P_b(t) \approx \frac{1}{1 + 4L_\perp^2 \tilde{\epsilon}/\tilde{\pi}_{\text{ad}}}. \quad (3.81)$$

To obtain the moments of the distribution for large times, we neglect the logarithmic terms and expand $P + p$ for $q = 0$ and small k and s . From the moments of $P + p$, the effective parameters of motion follow immediately. The effective velocity v for long times is given by

$$v = \frac{v_b}{1 + 4L_\perp^2 \tilde{\epsilon}/\tilde{\pi}_{\text{ad}}}, \quad (3.82)$$

as expected, since transition between the bound and unbound state are equilibrated at long times. Note that with Eq. (3.82) we have recovered in a more formal way the result of Eq. (3.1). The effective diffusion coefficient, D , is given by

$$D = \frac{D_b + 4L_\perp^2 \frac{\tilde{\epsilon}}{\tilde{\pi}_{\text{ad}}} D_{\text{ub}}}{1 + 4L_\perp^2 \tilde{\epsilon}/\tilde{\pi}_{\text{ad}}} + \frac{v_b^2 \tilde{\epsilon} \tilde{\pi}_{\text{ad}} / (4L_\perp^2)}{[\tilde{\pi}_{\text{ad}} / (4L_\perp^2) + \tilde{\epsilon}]^3}. \quad (3.83)$$

The first term is simply the average of the bound and unbound diffusion coefficient, the second one describes additional spreading of the distribution by detachment: some of the motors detach from the filament and do not move on average, while those still bound are driven away. Let us note that in the large-time regime and averaged over the tube cross-section, i.e., if the logarithmic term are neglected and q is set to zero, the system reduces to a one-dimensional two-state random walk with the rates $\tilde{\epsilon}$ and $\tilde{\pi}_{\text{ad}}/(4L_\perp^2)$ for transitions from the bound to the unbound state and vice versa.

The crossover to the long-time regime is given by the crossover time

$$t_{**} = \frac{v_b}{v} \frac{\tilde{\pi}_{\text{ad}}}{\tilde{\epsilon} 4\pi D_{\text{ub}}} \approx \frac{L_\perp^2}{\pi D_{\text{ub}}}, \quad (3.84)$$

where the last expression holds for large L_\perp and agrees with the crossover time obtained for the slab.

The results of the previous paragraphs can be generalized to tubes with arbitrarily shaped cross-sections. In this case, one has to replace the Fourier series by an expansion of $p(x, r, t)$ in a series of eigenfunctions of the perpendicular parts of the Laplacian which satisfy the appropriate boundary conditions. As one of the eigenfunctions is a constant for all tube shapes, we can always separate the constant from the other eigenfunctions and use an approximation corresponding to Eq. (3.78). Hence for long times, an effectively one-dimensional two-state random walk is obtained for arbitrary tube shape. The effective transition rate from the unbound to the bound state is $\tilde{\pi}_{\text{ad}}/\phi$, where ϕ is the cross-section of the tube.

3.5 Effective diffusion coefficient

In the discussion of the analytical solutions, we have already mentioned that large-scale diffusion is enhanced by repeated binding to and unbinding from the filament. A distribution of motors spreads quickly, as part of the cloud of motors is driven away by the filament, while those motors that are not bound to the filament perform simple diffusion. The effective diffusion coefficient is larger than the average of bound and unbound diffusion coefficients. For example, we have seen that it is given by

$$D = \frac{D_b + 4L_{\perp}^2 \frac{\tilde{\epsilon}}{\tilde{\pi}_{\text{ad}}} D_{\text{ub}}}{1 + 4L_{\perp}^2 \tilde{\epsilon} / \tilde{\pi}_{\text{ad}}} + \frac{v_b^2 \tilde{\epsilon} \tilde{\pi}_{\text{ad}} / (4L_{\perp}^2)}{[\tilde{\pi}_{\text{ad}} / (4L_{\perp}^2) + \tilde{\epsilon}]^3}. \quad (3.85)$$

in the case of the tube geometry. The second term is maximal if $\tilde{\epsilon} = \frac{\tilde{\pi}_{\text{ad}} / (4L_{\perp}^2)}{2}$. This means, that for a given geometry long-range diffusion can be optimized by tuning the detachment rate, e.g. by changing ionic conditions. In the case of a fixed detachment rate, diffusion can be optimized by adapting geometry. The optimum of the diffusion coefficient obtainable in this way is of the order $v_b^2 / \tilde{\epsilon}$, which can be quite large if ϵ is very small. Note, however, that, the smaller ϵ , the larger the crossover time to the geometry-dependent long-range transport regime.

Let us remember that enhancement of diffusion is also exhibited in the two-dimensional case and the slab, where it is of the order $(v_b / \epsilon)^2$, but not in the three-dimensional case. In that case only large logarithmic corrections, again of the order $(v_b / \epsilon)^2$, are obtained.

While this enhancement of diffusion might be quite useful, for example to increase the rates of diffusion-controlled chemical reactions, it is, in fact, not too surprising. The same expression for the effective diffusion coefficient as given in Eq. (3.85) is obtained for a simple two-state random walk [85] and has been discussed previously in various contexts including electrophoresis, chromatographic columns and hydrodynamic flow, see, e.g., Ref. [86].

Finally, let us mention that this enhancement of diffusion is also observed, if one considers two filaments in a tube, oriented into opposite directions, so that the net drift of the motors vanishes at large times. Similar behaviour can be expected for arrays of many filaments oriented randomly in all directions, a situation that might be interesting for the application of this enhancement of diffusion in an experiment or a nanotechnological device.

3.6 Arrays of parallel filaments

In vitro, microtubules can be aligned in parallel isopolar arrays [39, 40]. Let us briefly discuss motor movements in such systems of parallel filaments. First, we consider the case of an *infinite number of parallel filaments*, arranged periodically in a distance d_f . For the movement along the direction of the filament, we can equivalently consider a single filament, but periodic boundary conditions at surfaces in a distance $d_f/2$ on both sides of the filament. Hence, systems with infinitely many filaments in two dimensions or in the slab geometry exhibit similar behaviour as systems with one filament in a stripe in the two-dimensional plane or a rectangular tube, respectively. Periodically arranged filaments in the half-space geometry, fixed in parallel to the surface, result in movements as in a half slab. In both cases, the effective velocity is predicted by our first scaling argument to behave as $v \sim d_f^{-1}$ for sufficiently large d_f , which is confirmed by simulations.

Second, let us consider the case of a *finite number* N_f of filaments. We can adapt our original scaling argument for this case: The probability that the motor is bound is now given by $P_b \sim N_f/\epsilon$, while the probability that the motor is unbound is still given by the effective cross-section of the area it has explored. At large times, this area is independent of the size of the space between the filaments and thus of the filament–filament distance d_f . Hence, we predict that the time-dependent velocity is given by $v(N_f) \approx N_f \times v(N_f = 1)$ at large times and that the time-dependent scaling is the same as in the case of a single filament. The long-time velocity is independent of the distance d_f between the filaments, but the crossover to the large-time regime depends on d_f . This behaviour is confirmed by simulations for two- and three-dimensional situations.

3.7 Summary

In this chapter, we have discussed random walks of molecular motors in simple open geometries. These random walks consist of alternating sequences of directed movements along filaments and unbound diffusion. The compartment geometries are chosen such that diffusion in directions perpendicular to the filament may be restricted by confining walls, but not the movement along the filament and diffusion parallel to it. Long-range transport properties such as the effective velocity and the effective diffusion coefficient depend on the geometry, in particular the dimensionality of the compartment. In compartments where the motors can make excursions away from the filament of arbitrary length, such as the half space or the slab, the random walks of molecular motors exhibit anomalous drift. The effective velocities decrease as a power law at large times with an exponent depending on the dimensionality, $v(t) \sim t^{-(d-1)/2}$. These anomalous drift velocities are determined by the long-time tails of the distribution of return times to the filament. In addition, effective diffusion can be strongly enhanced by repeated binding and unbinding of motors and filaments.

Chapter 4

Concentration profiles in closed compartments

In the previous chapter, we have considered compartments which were open in at least one direction. In these systems, motors can move along filaments for a very long time. In this chapter, we consider closed compartments, i.e., now we close the system in all directions. In this case, the situation is different. Filaments now have to end inside the system, and motors moving along the filaments accumulate at their ends, generating density gradients inside the compartment. These density gradients lead to diffusive currents, so that eventually a stationary state forms, in which drift currents along the filaments are balanced by diffusive currents of unbound motors. As motors accumulate close to the filament ends, local motor concentrations can become large in these regions and exclusion interactions are important.

In this chapter, we will determine the stationary concentration profiles in closed compartments. We consider two basic geometries, a single filament or a number of parallel filaments in a closed tube [56] and a quasi-two-dimensional aster-like arrangement of filaments. Both geometries are accessible to experiments, and in fact some experimental concentration profiles have recently been determined in the case of asters [87].

4.1 Density profile in a closed tube

We first consider the tube geometry. On the one hand, placing one or several filaments and motors inside a tube should be experimentally feasible. The tube could again be either a glass tube or a liquid microchannel, as discussed in the previous chapter. On the other hand,

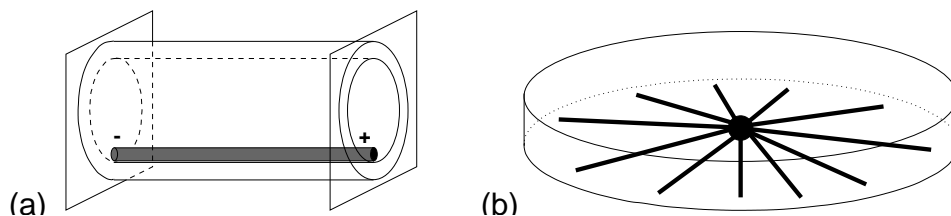


Figure 4.1: Geometries studied in this chapter: (a) a single filament in a closed tube and (b) an aster-like arrangement of filaments in a closed disk-like compartment.

tube-like geometries are quite common in cells, the most prominent example being the axon of a nerve cell, a thin tubular process, which can be up to a meter long. Similar processes, the hyphae, exist in the case of fungal cells. But also compartments inside the cell can have tubular shape, e.g. strands of cytosol crossing the vacuole in plant cells [88].

We consider a cylindrical tube of length L and radius R . One filament is located inside the tube. We assume that its length is equal to the tube length, so that motors arriving at the filament's end cannot step forward any more and have to wait there until they detach. This assumption is, however, not crucial, and introducing a finite distance between the filament end and the tube end does not alter the results dramatically. The filament can be located along the symmetry axis of the cylinder or parallel to it, fixed to the wall. We will treat these two cases as essentially equal, since simulations show that the differences are small. Obviously the first case is the nicer one for theoretical consideration because of its symmetry, while the second one should be a better description for a system that can be realized experimentally. In the following, we will also assume that the direction of motor movement along the filament is to the right.

Imagine now that a certain number of motors is placed into this tube. In the absence of ATP, the system will relax to an equilibrium state, where binding to and unbinding from the filament balance each other locally, i.e. at every single binding site. Both the bound and the unbound motor densities are constant. They are related by the equilibrium condition

$$\epsilon\rho_b = \pi_{\text{ad}}\rho_{\text{ub}}, \quad (4.1)$$

stating that the bound density is larger by a factor π_{ad}/ϵ than the unbound density. Remember that the detachment rate ϵ is related to the binding energy, $\epsilon \sim \exp(-\Delta E/k_B T)$. As the motors are strongly attracted by the filament, the filament can get quite crowded, even if the overall motor concentration is small. Therefore mutual exclusion of the motors, which ensures that a given binding site of the filament can only be occupied by one motor, has to be taken into account. Eq. (4.1) then becomes¹

$$\epsilon\rho_b = \pi_{\text{ad}}\rho_{\text{ub}}(1 - \rho_b). \quad (4.2)$$

As the unbound motor density is much smaller, it is not necessary to consider exclusion effects in the unbound state. We will therefore neglect them in the analytical calculations throughout this chapter.

The importance of exclusion in the bound state is even increased, when ATP is added to the system and the motors start to move along the filament. Motors moving to the right along the filament will build up a density gradient, which generates a diffusive current balancing the drift current of bound motors. Assuming now as a first approximation, that Eq. (4.1) still holds (which is justified if the velocity v_b is small and the bound density sufficiently low, as we will discuss later in this chapter), this balance can be expressed as

$$v_b\rho_b = D_{\text{ub}}\phi\frac{\partial\rho_{\text{ub}}}{\partial x} = D_{\text{ub}}\phi\frac{\epsilon}{\pi_{\text{ad}}}\frac{\partial\rho_b}{\partial x}, \quad (4.3)$$

which indicates that the motor density will increase exponentially along the filament. Thus motors accumulate at the right end of the filament, further increasing the bound density there. We will show below that an exponential profile is also found if we drop the assumption of local

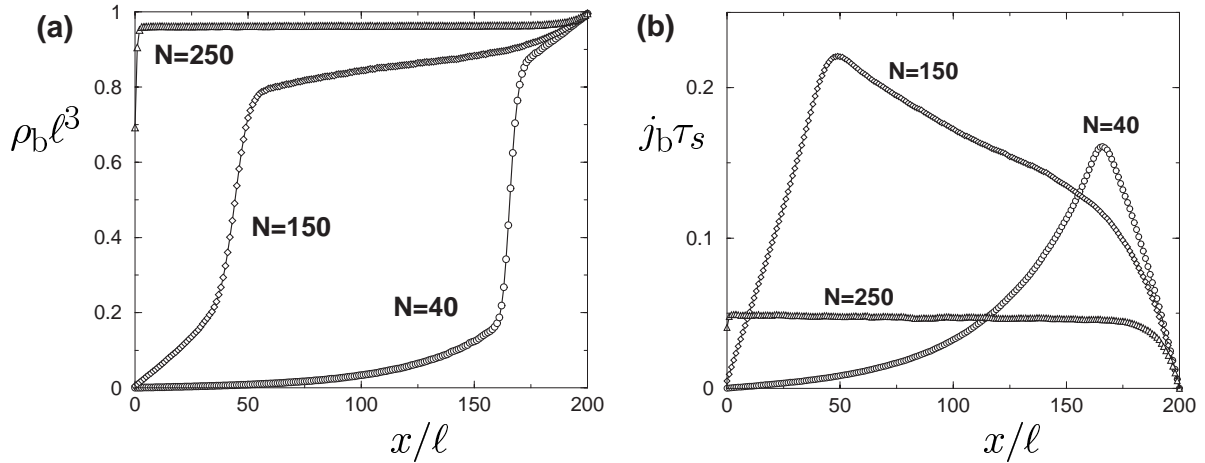


Figure 4.2: Profiles of (a) the bound density ρ_b and (b) the corresponding bound current j_b as functions of the coordinate x along the filament in the closed tube for three different total numbers of motors, N . The tube has length $L = 200\ell$ and radius $R = 25\ell$. Transport parameters are for kinesin as described in chapter 2.1.4.

equilibrium of binding and unbinding.

Let us now consider typical density profiles as obtained from Monte Carlo simulations, see Fig. 4.2 (a). If the total number N of motors is relatively small (the case $N = 40$ in Fig. 4.2), motors will crowd only at the end of the filament forming a kind of 'traffic jam'. If a motor detaches from the filament in the crowded region, it will diffuse back over a certain distance and rebind to the filament in the region behind the 'traffic jam', as in the jammed region rebinding is strongly reduced, since all binding sites are occupied. Again bound to the filament, the motor will propagate quickly along it, until it joins the 'traffic jam' again. Since motors are very likely to be recaptured by the filament closely behind the jammed region, the bound density in the region further away from the right end is small. In this region, exclusion plays no role, and here in fact an exponential density profile can be found.

If the number of motors in the tube is increased, the traffic jam will spread further to the left, as shown in Fig. 4.2 for $N = 150$. Motors will then also diffuse backwards over large distances since many attempts to rebind to the filament will fail, because the binding sites are already occupied.

Finally, if the motor concentration is very large, so that the filament is crowded over its whole length, the density profile becomes essentially constant except for the regions close to the ends, see the case $N = 250$ in Fig. 4.2. In this case, motors may diffuse back over the whole system length, but on the other hand the current along the filament is very small, because only few motors find an empty binding site in front of them.

The corresponding profiles of the current along the filament are shown in Fig. 4.2 (b). In the stationary state, the diffusive current of unbound motors integrated over the tube cross-section has the same absolute value, but the opposite sign. The current depends strongly on the position x along the filament. It also increases exponentially in regions of small density,

¹Remember that we use dimensionless units: Densities are defined per unit volume ℓ^3 , which is assumed to be occupied by one motor molecule and from which other motors are excluded. Exclusion effects are enhanced if the motors carry large cargoes, see section 4.4.

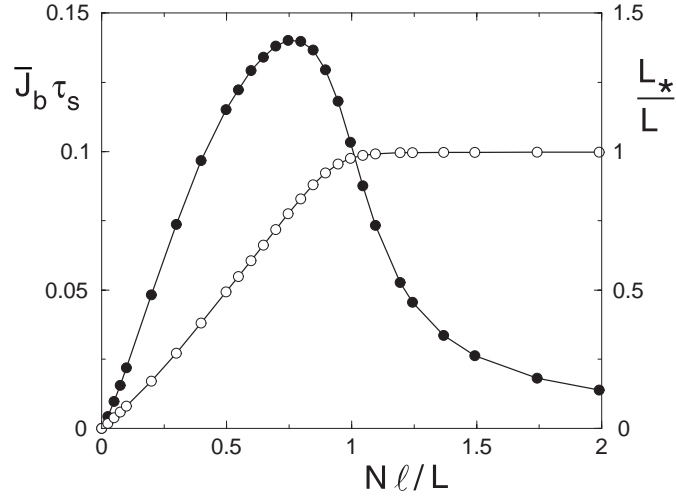


Figure 4.3: Average bound current \bar{J}_b (filled circles) and 'traffic jam' length L_* (open circles) as functions of the total number N of motors in the tube. Geometry and parameters of motion are the same as in Fig. 4.2.

but decreases rapidly in the jammed region. It reaches its maximum close to the end of the traffic jam. For the case of the completely jammed filament, the current profile is nearly flat, but the absolute current is small.

To obtain a global characterization of transport in the system, we determined the average current

$$\bar{J}_b \equiv \int_0^L dx j_b(x). \quad (4.4)$$

As a function of the total number N of motors in the system (or, equivalently, the motor concentration) it exhibits a maximum at an optimal motor concentration, see Fig. 4.3. For small N , it grows linearly with the number of motors, while for large N it decreases again since motion of the bound motors is slowed down by the increasing traffic jam. However, this decrease of the currents is rather slow, since additional motors introduced into the system can only rarely find free binding sites. For the system of Fig. 4.3, the maximal current occurs for $N \simeq 150$ motors, which corresponds to the intermediate case of the profiles in Fig. 4.2. A second quantity, which gives a global characterization of the profiles, is the length of the traffic jam, L_* . L_* can be determined from the condition $\rho_b(x_*) = 1/2$ as $L_* = L - x_*$. Results for L_* are also shown in Fig. 4.3. Comparing with the curve for \bar{J}_b shows that the optimal transport occurs when a large part of the filament is crowded, $L_* \simeq 0.77L$, but the traffic jam is not yet too dense.

Let us now insert some numbers. The data shown in Figs. 4.2 and 4.3 have been obtained for kinesin-like parameters by simulating the refined model described in chapter 2.1.4, which also models correctly the bound diffusion coefficient (or equivalently the randomness parameter). Let us mention at that point, that the differences compared to the simpler model are rather small.² The tube had length $L = 200\ell \simeq 1.6\mu\text{m}$ and radius $R = 25\ell \simeq 0.2\mu\text{m}$, where the periodicity $\ell = 8\text{nm}$ of microtubules has been inserted. For these parameters, the length scale

²In the more realistic model the length scale of the exponential part of the profile is slightly larger, leading to a slightly shorter traffic jam at the right end compared to the simpler model.

of the exponential part of the profile is $37\ell \simeq 300\text{nm}$. The maximal current occurs for a total number of $N \simeq 150$ motors in the tube, which corresponds to a total kinesin concentration of $\simeq 3\mu\text{M}$ in the chosen tube volume. Let us also mention that the stationary profiles are built up after about 5×10^5 Monte Carlo steps, which corresponds to a couple of seconds in real time.

Finally, we add a few remarks concerning the realization of such density profiles in cells. Strong localization of kinesin as discussed above for the case small overall motor concentration has been observed at the tip of fungal hyphae [89]. However, this localization is only found for kinesin lacking a regulatory domain.³ Wild-type kinesin can be deactivated by folding of the tail, if no cargo is bound to it [89,91]. As these deactivated motors do not advance along filaments, they can diffuse back over larger distances.

The question, whether and how motors are transported back is most prominent in the case of axons. Further regulatory mechanisms proposed for this case include local degradation of motors at the axon terminal [92] and backward transport by motors of opposite directionality [93,94]. Our results suggest that even without further regulation, diffusive backflow can be efficient in a certain range of overall motor concentrations. However, whether such conditions are realized in cells has to remain open at this point. Let us repeat that for transport in cells exclusion effects are strongly enhanced by large cargoes.

4.2 Two-state approximation

To get some further insight into the properties of these self-organized density profiles, we consider the stationary state in the two-state approximation, in which the dependence of the concentration profiles on the radial coordinate is neglected and motors can be in two states, namely bound and unbound. As we will see, this approximation captures most of the relevant features of these profiles, it allows for analytical solutions in some limits, and numerical solutions for the stationary profiles are obtained much faster than by Monte Carlo simulations. We will only consider the stationary state and use both the continuous and discrete versions of the two-state model, as the first one is more convenient for analytical considerations and the second one for numerics. A discussion of the validity of the two-state approximation will follow in section 4.3.

4.2.1 Continuous two-state equations

Let us first consider the continuous two-state model defined by Eqs. (2.17) and (2.18). As we are interested in the stationary solution, we can replace one of the equations by the condition that the sum of the bound and unbound currents vanishes. For simplicity, we will neglect exclusion effects of unbound motors in the following.⁴

The continuous two-state equations for the stationary bound and unbound density profiles are thus

$$v_b \rho_b (1 - \rho_b) = D_{ub} \phi \frac{\partial \rho_{ub}}{\partial x} + D_b \frac{\partial \rho_b}{\partial x} \quad (4.5)$$

$$v_b \frac{\partial}{\partial x} \rho_b (1 - \rho_b) - D_b \frac{\partial^2 \rho_b}{\partial x^2} = \tilde{\pi}_{ad} \rho_{ub} (1 - \rho_b) - \tilde{\epsilon} \rho_b. \quad (4.6)$$

³Similar observations in a different geometry have been made in experiments using liver cells [90].

⁴Exclusion interactions for the unbound motors are easily included in the numerical calculations presented below, but do not substantially alter the results.

Approximative solutions

(i) First, we consider the low-density limit, where we can neglect hard core exclusion. This is appropriate in the non-crowded region, where $\rho_b \ll 1$. For simplicity, we also neglect the bound diffusion terms, i.e., we consider the case $D_b = 0$. On the one hand, this can be understood as taking into account only the first non-vanishing terms in the derivation of the continuum equations. On the other hand, a comparison of numerical solutions of the equations with and without this terms shows, that the precise value of D_b is largely irrelevant for the solution, as long as the detachment rate is small, which, however, is the case for processive motors. In the low-density limit the equations become linear,

$$v_b \rho_b = D_{ub} \phi \frac{\partial \rho_{ub}}{\partial x} \quad (4.7)$$

$$v_b \frac{\partial \rho_b}{\partial x} = \tilde{\pi}_{ad} \rho_{ub} - \tilde{\epsilon} \rho_b, \quad (4.8)$$

and the solution is a density profile that increases exponentially along the tube,

$$\rho_b(x) = \mathcal{N} e^{x/\xi}, \quad (4.9)$$

where \mathcal{N} is a constant and

$$\xi^{-1} = -\frac{\tilde{\epsilon}}{2v_b} + \frac{1}{2} \sqrt{\frac{\tilde{\epsilon}^2}{v_b^2} + \frac{4\tilde{\pi}_{ad}}{D_{ub}\phi}}. \quad (4.10)$$

For small v_b , we obtain $\xi \approx (\frac{\tilde{\epsilon}}{\tilde{\pi}_{ad}} D_{ub} \phi) / v_b$, which is the result obtained above from our first approximation assuming that detachment and reattachment are equilibrated. The unbound density is given by

$$\rho_{ub}(x) = \frac{\tilde{\epsilon}}{\tilde{\pi}_{ad}} \rho_b(x) + \frac{v_b}{\tilde{\pi}_{ad}} \frac{\partial \rho_b(x)}{\partial x} = \mathcal{N} \left(\frac{\tilde{\epsilon}}{\tilde{\pi}_{ad}} + \frac{v_b}{\tilde{\pi}_{ad}\xi} \right) e^{x/\xi}, \quad (4.11)$$

i.e., bound and unbound density are proportional in the low-density limit. The first term of the factor relating bound and unbound density is the one obtained in the case of equilibrated transitions between the bound and unbound states, the second one is a correction showing that attachment and detachment are driven out of equilibrium if $v_b \neq 0$. (Note, however, that this term is of order v_b^2 , since $\xi \sim 1/v_b$, so that up to linear order in v_b attachment and detachment are still equilibrated.) As this correction term is positive, the current of motors attaching to the filament at a given site, $\tilde{\pi}_{ad} \rho_{ub}(x)$, is larger than the current of detaching motors at the same site, $\tilde{\epsilon} \rho_b(x)$, which is easy to understand, since the motors bound to the filament are driven away by the drift v_b . For small driving velocity v_b , we can replace the local balance of currents at a site x by the condition

$$\tilde{\epsilon} \rho_b(x + \frac{v_b}{\tilde{\epsilon}}) = \tilde{\pi}_{ad} \rho_{ub}(x), \quad (4.12)$$

which states that all motors attaching to the filament at site x , move for a distance $v_b/\tilde{\epsilon}$ and thus detach at site $x + v_b/\tilde{\epsilon}$. Inserting the solution given above, we can check that this is fulfilled for small $v_b/\tilde{\epsilon}$.

$$\tilde{\epsilon} \rho_b(x + \frac{v_b}{\tilde{\epsilon}}) = \tilde{\epsilon} e^{v_b/(\tilde{\epsilon}\xi)} \rho_b(x) \approx (\tilde{\epsilon} + \frac{v_b}{\xi}) \rho_b(x) = \tilde{\pi}_{ad} \rho_{ub}(x). \quad (4.13)$$

The fact that more motors attach to the filament than detach from it, indicates that this solution cannot be correct for all x . In a system without hard core exclusion, the current of detaching motors will be larger than the current of attaching motors only at the end of the filament. In the spirit of the ansatz (4.12) we can account for detachment at the filament end by assuming that all motors that would have detached in the interval $[L, L + \frac{v_b}{\epsilon}]$ are forced by the boundary to detach at the last binding site of the filament. Therefore the density at the filament end, $\rho_b(x = L)$, is given by

$$\rho_b(x = L) = \frac{1}{\ell} \int_L^{L + \frac{v_b}{\epsilon}} dx \mathcal{N} e^{x/\xi} = \frac{\xi}{\ell} \mathcal{N} e^{L/\xi} \left(e^{v_b/(\epsilon\xi)} - 1 \right) \approx \frac{v_b}{\epsilon\ell} \mathcal{N} e^{L/\xi}, \quad (4.14)$$

where ℓ is again the size of the binding site and the last approximation is for small velocity v_b , for which the ansatz (4.12) is justified. Comparing with simulations for the case without hard core exclusion shows good agreement of the density at the last lattice site with the values obtained by this procedure. In the more realistic case, where there is hard core exclusion, however, the present solution holds only as long as the bound density is sufficiently small and will break down at a certain x , as the bound density increases exponentially along the filament.

(ii) Let us now consider the opposite limit, where ρ_b is close to one as appropriate for the right end of the tube. At the end of the tube, motors have to detach from the filament, while attachment to the filament is negligible, since there are nearly no free binding sites. We thus neglect the term $\tilde{\pi}_{\text{ad}}\rho_{\text{ub}}(1 - \rho_b)$. With this approximation the equations decouple and we obtain

$$v_b(1 - 2\rho_b) \frac{\partial \rho_b}{\partial x} = -\tilde{\epsilon}\rho_b, \quad (4.15)$$

which can be integrated and gives

$$\ln \rho_b - 2\rho_b = \frac{x_0 - x}{v_b/\tilde{\epsilon}}. \quad (4.16)$$

If ρ_b is close to one, we can expand the logarithm and obtain a linear profile

$$\rho_b(x) = 1 + \frac{x - L}{v_b/\tilde{\epsilon}}, \quad (4.17)$$

where the integration constant x_0 has been fixed by the boundary condition $\rho_b(x = L) = 1$, which ensures that the bound current through the right wall is zero. The unbound profile is obtained by integration of Eq. (4.5),

$$\rho_{\text{ub}}(x) = \frac{\tilde{\epsilon}}{D_{\text{ub}}\phi} \left[x \left(L - \frac{x}{2} \right) + C \right], \quad (4.18)$$

where C is a constant. Note that the boundary condition for the unbound density, $\partial\rho_{\text{ub}}/\partial x = 0$ at $x = L$, is automatically fulfilled. Comparison with the numerical solution for the lattice case indicates that these expression for the bound and unbound density profiles are only valid very close to the right boundary.

Comparison with the continuum equation for the ASEP

It is instructive to compare our case with the simpler case of the one-dimensional asymmetric simple exclusion process (ASEP), which corresponds to the motion on the filament without

the possibility to detach into the unbound state. In this case, the continuum equation is

$$\frac{\partial \rho}{\partial t} = D \frac{\partial^2 \rho}{\partial x^2} - v \frac{\partial}{\partial x} \rho (1 - \rho), \quad (4.19)$$

where we have used the same symbols as above but without the subscript 'b' and reintroduced the 'bound' diffusion term. Using the substitution $\rho(x) = \frac{1}{2}[1 + u(x)]$, Eq. (4.19) can be reduced to the Burgers equation,

$$\frac{\partial u}{\partial t} = D \frac{\partial^2 u}{\partial x^2} + vu \frac{\partial u}{\partial x}. \quad (4.20)$$

In the stationary state this gives

$$v\rho(1 - \rho) = D \frac{\partial \rho}{\partial x} \quad \text{or} \quad \frac{2D}{v} \frac{\partial u}{\partial x} = 1 - u^2, \quad (4.21)$$

if the system is closed and the net current flowing through it vanishes. The solution is given by

$$\rho^{(\text{ASEP})}(x) = \frac{1}{2} \left[1 + \tanh \frac{v(x - x_0)}{2D} \right]. \quad (4.22)$$

In the limit $D = 0$, corresponding to no backward steps in the lattice model, this solution is a step from zero density to density one at $x = x_0$. For finite D , the step has a finite width. In both cases however, the stationary state is an equilibrium profile, in the sense that local currents through all bonds of the lattice vanish. This case can be imagined, as in the standard driven lattice gas, as a system where gravity or an electric field drives the particles towards the right boundary, while thermal fluctuations lead to backward diffusion. Returning to our case, we note that this is not the case here. Local currents are not zero, because the current on the filament is not balanced by a diffusive current along the filament, but by the diffusive current of unbound motors. Only the integral of the current over the tube cross section is zero.

Let us derive an equation corresponding to Eq. (4.21). By eliminating the unbound density from Eq. (4.5) using Eq. (4.6), we obtain

$$\begin{aligned} v_b \rho_b (1 - \rho_b) &= D_b \frac{\partial \rho_b}{\partial x} + \frac{D_{\text{ub}} \phi \tilde{\epsilon}}{\tilde{\pi}_{\text{ad}}} \frac{\partial}{\partial x} \frac{\rho_b}{1 - \rho_b} + \frac{D_{\text{ub}} \phi}{\tilde{\pi}_{\text{ad}}} \frac{\partial}{\partial x} \frac{v_b \frac{\partial}{\partial x} \rho_b (1 - \rho_b) - D_b \frac{\partial^2}{\partial x^2} \rho_b}{1 - \rho_b} \\ &= D_{\text{eff}} \frac{\partial \rho_b}{\partial x} + j_{\text{eff}}(\rho_b(x)). \end{aligned} \quad (4.23)$$

The first term on the right hand side can be interpreted as a diffusion term with a density-dependent effective diffusion coefficient D_{eff} defined by

$$D_{\text{eff}}(\rho_b) \equiv D_b + \frac{D_{\text{ub}} \phi \tilde{\epsilon} / \tilde{\pi}_{\text{ad}}}{(1 - \rho_b)^2}. \quad (4.24)$$

This effective diffusion coefficient has the unusual property to increase with increasing density, i.e., motors diffuse faster in regions with a high motor density instead of being slowed down by mutual exclusion. This counterintuitive effect is due to the fact that the motors that really diffuse are the unbound ones, while those having a high density are the bound ones. The increase in diffusive current is simply obtained because more motors are unbound in a region where the density of bound motors is high. Unlike in Eq. (4.21), however, the driven and

the diffusive current do not balance each other here: the second term on the right hand side of Eq. (4.23), which can be interpreted as an effective net flux $j_{\text{eff}}(x)$, is a signature for the out-of-equilibrium nature of the stationary state.

Let us finally use Eq. (4.23) to obtain another approximative solution in an expansion around the solution for the ASEP. We assume that the exchange between the bound and unbound state is approximately in equilibrium and neglect the last term of Eq. (4.23). Using the same substitution as in Eq. (4.20), we get

$$\frac{v_b}{4}(1 - u^2) = \frac{D_b}{2} \frac{\partial u}{\partial x} + \frac{D_{\text{ub}} \phi \tilde{\epsilon}}{\tilde{\pi}_{\text{ad}}} \frac{\partial}{\partial x} \frac{1 + u}{1 - u}. \quad (4.25)$$

For $\tilde{\epsilon} \phi / \tilde{\pi}_{\text{ad}} = 0$, we recover the case of the ASEP. The correction to linear order in $\tilde{\epsilon} \phi / \tilde{\pi}_{\text{ad}}$ can be derived in a straight-forward way by putting $u = u_0 + \frac{\tilde{\epsilon} \phi}{\tilde{\pi}_{\text{ad}}} u_1$, where u_0 is the solution for $\tilde{\epsilon} \phi / \tilde{\pi}_{\text{ad}} = 0$. The solution for u_1 is

$$u_1(x) = F(x) \exp\left(-\int_{x_0}^x dy \frac{v_b u_0(y)}{D_b}\right) \quad (4.26)$$

with

$$F(x) = -\frac{2D_{\text{ub}}}{D_b} \int_{x_0}^x d\tilde{y} \left[\frac{\partial}{\partial \tilde{y}} \frac{1 + u_0}{1 - u_0} \right] \times \exp\left(\int_{x_0}^{\tilde{y}} dy \frac{v_b u_0(y)}{D_b}\right). \quad (4.27)$$

We now consider the region, where $\rho_b \simeq 1/2$. In this region u_0 , u_1 and $x - x_0$ are small and we can approximate the solution by

$$u_1 \simeq F(x) \simeq -\frac{4D_{\text{ub}}}{D_b} (u_0 + u_0^2). \quad (4.28)$$

Let us remember that $u_0(x) \sim (x - x_0) + O([x - x_0]^3)$. Our result therefore yields a linear profile for small $x - x_0$, just as in the case of the ASEP, but with an effective diffusion coefficient $D_b + 4D_{\text{ub}} \phi \tilde{\epsilon} / \tilde{\pi}_{\text{ad}}$, i.e., the increase of the profile is less steep due to backward diffusion of unbound motors. However, in contrast to that case, here the quadratic term breaks the symmetry $u(x_0 + x) = -u(x_0 - x)$: For positive $x - x_0$ the profile is more strongly flattened than for negative $x - x_0$. This reflects the density dependence of the effective diffusion coefficient discussed above. As the density increases, more motors detach and thus the effective diffusion coefficient grows, enhancing the flattening of the profile.

4.2.2 Discrete model

For numerical purposes, the discrete two-state model defined by Eqs. (2.15) and (2.16) is more convenient than the continuum model. In comparison to Monte Carlo simulations, it has the advantage that run times to obtain stationary profiles are much shorter. This is particularly important to study large systems, where $L \gtrsim 1250\ell$ or $L \gtrsim 10\mu\text{m}$ in the case of kinesin and microtubules.

In the stationary state the discrete two-state equations (2.15) and (2.16) can be written as

$$v_b \rho_b(x) [1 - \rho_b(x + 1)] = \phi D_{\text{ub}} [\rho_{\text{ub}}(x + 1) - \rho_{\text{ub}}(x)] \quad (4.29)$$

$$v_b \rho_b(x) [1 - \rho_b(x + 1)] - v_b \rho_b(x - 1) [1 - \rho_b(x)] = \tilde{\pi}_{\text{ad}} \rho_{\text{ub}}(x) [1 - \rho_b(x)] - \tilde{\epsilon} \rho_b(x), \quad (4.30)$$

where ϕ is the cross-section of the tube or, more general, the number of unbound 'channels' per bound 'channel'. For a cylindrical tube of radius R with a single filament, $\phi \approx \pi R^2$; if there are N_f isopolar parallel filaments, $\phi \approx \pi R^2/N_f$. At the boundaries, $x = 0$ and $x = L$, terms corresponding to currents through the tube walls have to be omitted in Eq. (4.30). Eq. (4.29) holds for $0 < x < L$. Together with the normalization condition

$$\sum_{x=0}^L [\rho_b(x) + \phi \rho_{ub}(x)] = \frac{N}{\ell^2 N_f}, \quad (4.31)$$

which fixes the total number N of motors in the tube, these equations form a system of $2L$ (however nonlinear) equations for the $2L$ unknown densities $\rho_b(x)$ and $\rho_{ub}(x)$, $0 < x \leq L$.

If the hard core exclusion can be neglected, i.e. far from the jammed region, Eqs. (4.29) and (4.30) are equivalent to the recursion relation

$$\left[2 + \frac{\tilde{\pi}_{ad}}{D_{ub}\phi} + \frac{\tilde{\epsilon}}{v_b}\right] \rho_{ub}(x) - \rho_{ub}(x-1) - \left[1 + \frac{\tilde{\epsilon}}{v_b}\right] \rho_{ub}(x+1) = 0, \quad (4.32)$$

with the solution $\rho_b(x) \sim \rho_{ub}(x) \sim a^x$, where a is given by a quadratic equation as

$$a = \frac{1}{2} \left[1 + \frac{1 + \tilde{\pi}_{ad}/(D_{ub}\phi)}{1 + \tilde{\epsilon}/v_b} \right] + \frac{1}{2} \sqrt{\left[1 + \frac{1 + \tilde{\pi}_{ad}/(D_{ub}\phi)}{1 + \tilde{\epsilon}/v_b} \right]^2 - \frac{4}{1 + \tilde{\epsilon}/v_b}}. \quad (4.33)$$

Taking the continuum limit the solution of the continuum model is recovered.

Numerical solutions for the density profiles

The full system of equations (4.29)–(4.31) is solved numerically. We applied Newton's method with backtracking to find solutions of the system of non-linear equations, see chapter 9.7 of Ref. [95]. Density profiles are obtained within a few seconds for small systems ($L = 200\ell$), in which case the simulations take several hours, for a large system ($L = 1000\ell$) simulations sometimes (depending on the parameters, in particular the number of motors) do not reach the stationary state within several days, while density profiles are obtained from the two-state equations within about one day.

Some profiles of the bound motor density as well as the average current as a function of the number of motors are shown in Fig. 4.4 for a relatively large system ($L = 1000$). While the main features are the same as for the smaller system discussed above, some additional details can be seen here. The current increases linearly with the number N of motors for small N , but at a certain point, $N \simeq 500$ in Fig. 4.4(b), the slope begins to change. The current then increases more slowly, but again nearly linearly, until it reaches its maximum. This change in slope of the current corresponds to the formation of a plateau in the density profile, where the density in the traffic jam is approximately constant and changes only little upon addition of motors.

Comparing the density profiles with those obtained from simulations, we find that the length scale of the exponential increase of the density is smaller in the two-state model. Correspondingly the traffic jam is slightly longer in this case. This difference is due to neglecting a depletion zone close to the filament: Close to the filament, the unbound density is smaller than its radial average in the low-density region. Taking it as independent of the radial coordinate, we thus overestimate the current from the unbound to the bound state. Therefore

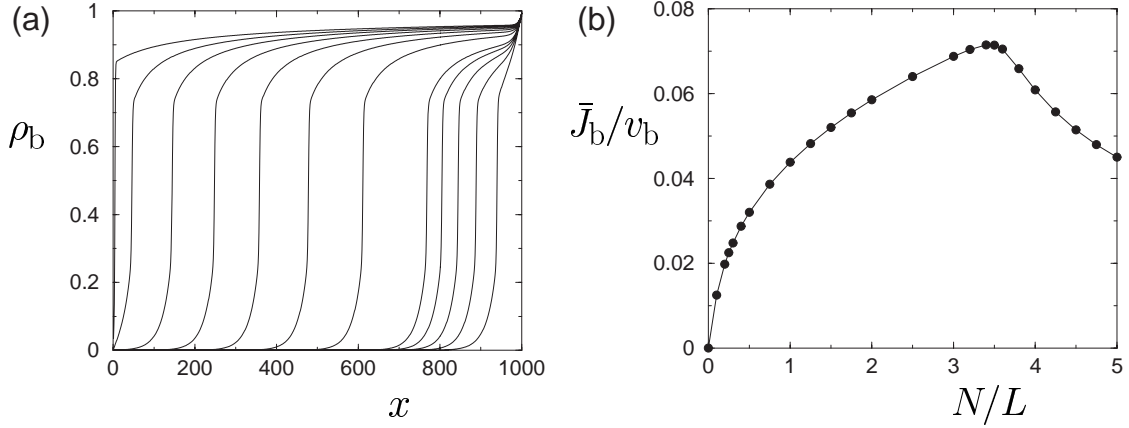


Figure 4.4: (a) Profiles of the bound motor density ρ_b as a function of the spatial coordinate x parallel to the filament and (b) average bound current \bar{J}_b as a function of the number N of motors in the tube as obtained by numerical solution of the discrete two-state model. The chosen tube has length $L = 1000$ and radius $R = 25$. The parameters of motion are $v_b = 0.01$, $D_{ub} = 1/6$, $\epsilon = 10^{-4}$, $\pi_{ad} = 1$. The numbers of motors in (a) are (from right to left) $N = 100, 200, 300, 400, 500, 1000, 1500, 2000, 2500, 3000, 3500$ and 4000 .

there are more motors bound to the filament in the two-state model than in the simulations, which results in a longer traffic jam, and the maximum of the current is shifted to a smaller number of motors in the system. On the other hand, agreement of the results of the two-state model and simulations is good, if the entire filament is crowded by motors.

4.3 Depletion layer

We have discussed in the previous section that in the two-state approximation a depletion zone close to the filament is disregarded. In this section, we derive analytically an expression for the radial dependence of the unbound density, which exhibits depletion of motors close to the filament. We restrict the analysis again to the linear regime, i.e. to the region of low motor concentration.

Let us therefore consider the full continuum equations (2.13) and (2.14). In the stationary state, the linearized equations (obtained by neglecting exclusion terms) are given by

$$-D_{ub}\Delta\rho_{ub} = \delta(\mathbf{r}) \left[\tilde{\epsilon}\rho_b - \tilde{\pi}_{ad}\rho_{ub,0} \right] \quad (4.34)$$

$$v_b \frac{\partial \rho_b}{\partial x} - D_b \frac{\partial^2 \rho_b}{\partial x^2} = -\tilde{\epsilon}\rho_b + \tilde{\pi}_{ad}\rho_{ub,0} \quad (4.35)$$

with $\rho_{ub,0}(x) = \ell^2 \rho_{ub}(x, r = 0)$. The separation ansatz

$$\rho_{ub}(x, r) = e^{x/\xi} f(r), \quad \rho_b(x) = B_0 e^{x/\xi}, \quad (4.36)$$

where B_0 is a constant, leads to

$$0 = D_{ub} \left[\xi^{-2} + \frac{\partial^2 f(r)}{\partial r^2} + \frac{1}{r} \frac{\partial f(r)}{\partial r} \right] \quad (4.37)$$

$$0 = -v_b \xi^{-1} B_0 + D_b \xi^{-2} B_0 - \tilde{\epsilon} B_0 + \tilde{\pi}_{ad} f_0, \quad (4.38)$$

where $f_0 = \ell^2 f(0)$. Eq. (4.37) holds for $r \neq 0$. The solution for $f(r)$ can be expressed in terms of the Bessel functions of order zero of the first and second kind, J_0 and Y_0 [81],

$$f(r) = C \left[J_0(r/\xi) - \frac{J_1(R/\xi)}{Y_1(R/\xi)} Y_0(r/\xi) \right], \quad (4.39)$$

where C is a constant and J_1 and Y_1 are Bessel functions of the first order,

$$J_1(z) = -\frac{\partial}{\partial z} J_0(z) \quad \text{and} \quad Y_1(z) = -\frac{\partial}{\partial z} Y_0(z). \quad (4.40)$$

This solution fulfills the boundary condition $\partial f / \partial r = 0$ at $r = R$. However, $f(r)$ diverges logarithmically for small r as can be seen from the asymptotic behaviour of the Bessel functions,

$$J_0(z) \approx 1 - \frac{1}{4} z^2 \quad \text{and} \quad Y_0(z) \approx \frac{2}{\pi} \ln\left(\frac{z}{2}\right) \quad (4.41)$$

for small z . This divergence is again due to the description of the filament as a line.

We thus consider a filament of finite radius ℓ . In this case, the diffusion equation (4.34) holds only for $r > \ell$ and thus the δ -term can be omitted. Binding to and unbinding from the filament are again described by Eq. (4.35) and matched to the diffusion equation by $\rho_{\text{ub},0}(x) = (\pi\ell^2/4)\rho_{\text{ub}}(x, r = \ell)$, which yields a second boundary condition for $f(r)$, $f(r = \ell) = (4/\pi\ell^2)\rho_{\text{ub},0}(x)e^{-x/\xi} = (4/\pi\ell^2)f_0$. With the last expression, we fixed the remaining overall multiplicative constant, so that $\rho_{\text{ub},0}(x) = f_0 e^{x/\xi}$. The solution for $f(r)$ is then fully determined and given by

$$f(r) = \frac{4f_0}{\pi\ell^2} \frac{J_0(r/\xi)Y_1(R/\xi) - J_1(R/\xi)Y_0(r/\xi)}{J_0(\ell/\xi)Y_1(R/\xi) - J_1(R/\xi)Y_0(\ell/\xi)}. \quad (4.42)$$

A condition to determine ξ can now be obtained from the balance of bound and unbound currents,

$$v_{\text{b}}\rho_{\text{b}}(x) = D_{\text{b}} \frac{\partial \rho_{\text{b}}(x)}{\partial x} + D_{\text{ub}} 2\pi \int_{\ell}^R dr r \frac{\partial}{\partial x} \rho_{\text{ub}}(x, r). \quad (4.43)$$

Inserting the exponential dependence on x , derivatives are replaced by powers of ξ and the integral over ρ_{ub} is turned into an integral over $f(r)$ only. ρ_{ub} is expressed in terms of ρ_{b} , and with the definition

$$I(\ell/\xi, R/\xi) \equiv \frac{2\pi}{\xi^2} \int_{\ell}^R dr r \frac{f(r)}{4/(\pi\ell^2)} = 2\pi \int_{\ell/\xi}^{R/\xi} dz z \frac{J_0(z)Y_1(R/\xi) - J_1(R/\xi)Y_0(z)}{J_0(\ell/\xi)Y_1(R/\xi) - J_1(R/\xi)Y_0(\ell/\xi)}, \quad (4.44)$$

Eq. (4.43) can be written as

$$v_{\text{b}} = \frac{D_{\text{b}}}{\xi} + D_{\text{ub}} \frac{4\xi^2}{\pi\ell^2} I(\ell/\xi, R/\xi) \left[\frac{\tilde{\epsilon}}{\tilde{\pi}_{\text{ad}}\xi} + \frac{v_{\text{b}}}{\tilde{\pi}_{\text{ad}}\xi^2} - \frac{D_{\text{b}}}{\tilde{\pi}_{\text{ad}}\xi^3} \right], \quad (4.45)$$

from which we determine ξ numerically. There are actually several roots of Eq. (4.45), but the relevant one for our case is the largest one, as smaller roots lead to oscillatory radial profiles, which do not correspond to stationary states.

Let us now discuss the profiles obtained by these calculations and compare them to those obtained by Monte Carlo simulations. In Fig. 4.5, we have plotted both the longitudinal [Fig. 4.5(a)] and radial profiles [Fig. 4.5(b)] as obtained by both methods. For sufficiently

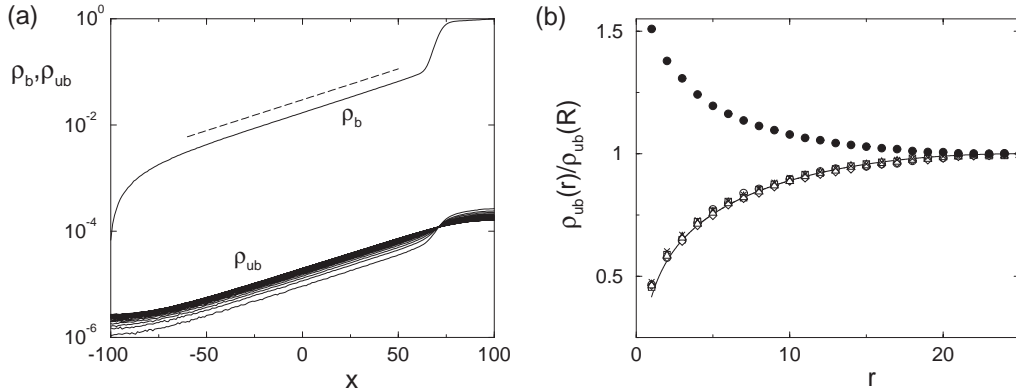


Figure 4.5: (a) Profiles of the bound density ρ_b (thick line) and the radius-dependent unbound density ρ_{ub} as functions of the spatial coordinate x parallel to the filament. The dashed line indicates the exponential $\sim \exp(x/37.37)$ as obtained from the linearized mean field equations. (b) Radial profile of the unbound density in the exponential profile region, $x = -40$ (\circ), -20 (\square), 0 (\diamond), 20 (\triangle), 40 (\times), and in the crowded region, $x = 80$ (\bullet). The solid line shows the analytical result (4.42). The parameters are $L = 201$, $R = 25$, $N = 50$, $\alpha = 9.93 \times 10^{-3}$, $\beta = 0$, $\gamma = 0.99$, $\epsilon = 10^{-4}$, and $\pi_{ad} = 1$.

small bound densities, where we can use the linearized description, the radial profile of the unbound density is nearly flat far from the filament and exhibits a depletion zone close to the filament, which behaves as $\ln(r/\xi)$ for small r . The filament acts like a sink for the unbound motors [84], because these are driven away upon binding to it. In Fig. 4.5(b), the radial profiles obtained from simulations have been rescaled by $\rho_{ub}(x, r = R)$, so that curves for different values of x fall together, showing that the separation ansatz (4.36) is justified in the low-density region. In the low-density limit the simulated radial profiles agree well with the analytical description of the depletion layer. In the crowded region close to the right end of the tube, on the other hand, there is no depletion, but rather an increased unbound density close to the filament [filled circles in Fig. 4.5(b)].

Finally, solving Eq. (4.45) numerically, we obtain $\xi \simeq 37.37$ for the parameters used in Fig. 4.5, in good agreement with the value from simulations of the lattice model, which is $\xi \simeq 37$. The two-state approximation yields a smaller value, $\xi \simeq 24$. As already discussed in the previous section, the current of motors attaching to the filament is overestimated by the two-state approximation, in which it is determined by the average unbound density rather than by the smaller value of the unbound density in the depletion layer close to the filament.

4.4 Some modifications of the model

The systems discussed so far are idealizations of a real system in several aspects. In the following, we consider a few modifications of the model. We anticipate that these modifications do not change substantially the qualitative features of our results. The main properties of the density profiles are generic and independent of the detailed modeling.

(1) We have assumed that detachment at the end of the filament occurs with the same rate as detachment at any other site of the filament. A second possibility is that motors

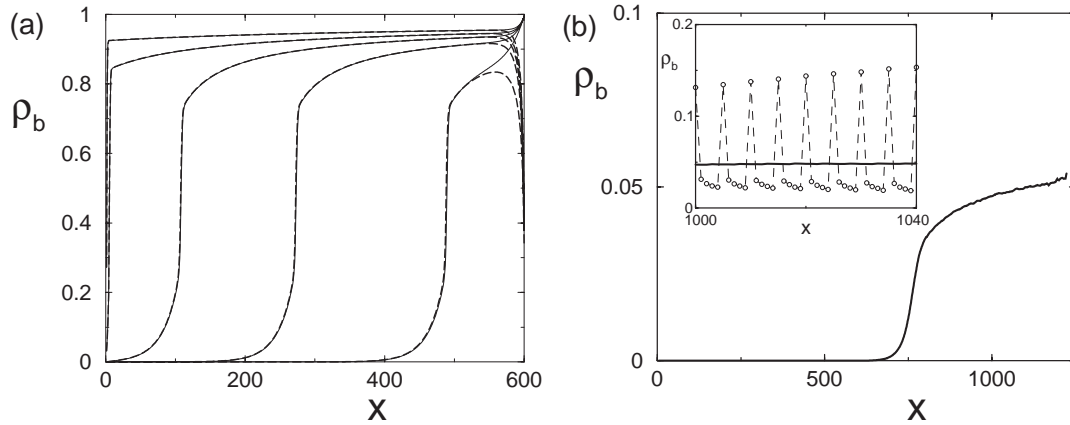


Figure 4.6: (a) Profiles of the bound density ρ_b for active and thermal detachment of motors at the filament end: A Motor at the end of the filament detaches with the same probability as at any other filament site (solid lines) or by a forward step (dashed lines). $L = 600$, $R = 25$, parameters of motion as in Fig. 4.4 and $N = 200, 800, 1400, 2000, 2600$ (from right to left) (b) Motors carrying larger cargoes: Profile of the bound density in the case where motors occupy a volume $(5\ell)^3$, see text. In the region close to the filament end, a sublattice structure is observed (inset). The solid line is an average of the profile over five subsequent lattice sites. $L = 1250$, $R = 25$, $N = 1000$, parameters of motion as in Fig. 4.5.

detach quickly at the end by making a normal step which, however, leads to unbinding. The two cases correspond to thermal and active detachment, respectively. The question which case is appropriate for biological motors must, of course, be decided by experiments (and the answer could also be a combination of both and/or depend on the type of motor). To our knowledge there is only indirect evidence for a quicker detachment of kinesin motors at the microtubule end from experiments and computer simulation of the formation of microtubule aster by motors.⁵ Fig. 4.6(a) shows density profiles for both cases as obtained from the discrete two-state model. One can clearly see that the profiles agree well except for the region close to the filament end. In particular, the steep increase of the density profile at the beginning of the 'traffic jam' is the same in both cases. This observation shows that the traffic jam is not due to the slow detachment at the end, but to the exponential increase of the motor concentration, which follows from the balance of bound drift current and unbound diffusive currents. Only the weaker increase of the bound density inside the jammed region is due to the small detachment rate at the end of the filament and is therefore missing in the case of quick detachment at the end, where the profile is decreasing rather than increasing in the jammed region. The overall current is, of course, larger in the case of quick detachment at the end.

⁵In these studies the detachment rate at the end of the microtubule has been identified as the crucial parameter for the formation of aster or vortex structures. A higher detachment rate at the end than at other binding sites has to be assumed to reproduce the experimentally observed vortex structures in simulations [62]. For the formation of asters, on the other hand, the detachment at the microtubule end should not be too quick, as motor complexes have to remain bound for some time at the end of a microtubule to allow for the transport of that microtubule [61]. Kinesin is able to form both asters and vortices, suggesting that detachment at the microtubule end is relatively quick, while the kinesin-related motor ncd only forms asters and thus probably detaches slowly at the microtubule end [62].

(2) Mutual exclusion of motors is obviously enhanced, if the motors carry large cargoes such as latex beads or vesicles. On the other hand, microtubules consist of 13 protofilaments (parallel tracks), i.e., there are more binding sites. We have therefore performed simulations for a model, where these two features have been included. Some limitations however remain because of the underlying lattice. In our simulations, motors move on a microtubule consisting of 12 protofilaments arranged in a tubular geometry and occupy a cubic volume of M^3 lattice sites. In the simulations we chose $M = 3$ and $M = 5$. In addition, these cubes attach to the filament only with one of their surface sites, which represents the motor. By consequence, the cubes not bound to the filament have an additional rotational degree of freedom. They are rotated by 90° into each of the four possible directions with a probability $(1 - \gamma_{\text{rot}})$ per unit time. The resulting profiles differ from the ones discussed so far in two respects, see Fig. 4.6(b): (i) A sublattice structure is observed in the crowded region of the microtubule [see inset in Fig. 4.6(b)], which is due to the cubic shape of the cargoes and the rigidity of their attachment to the motors. If we average over this sublattice structure, we obtain profiles that resemble the ones for the simpler case. (ii) The value of the bound density in the crowded region is much smaller, as a smaller number of motors can block the filament. In particular, a motor bound to one protofilament also blocks binding sites of the adjacent protofilaments because of the steric hindrance induced by its large cargo.

4.5 Density profiles in asters

In this section, we consider profiles of the motor concentration in aster-like arrangements of filaments. Microtubule asters can be formed *in vitro* by self-organization of microtubules and kinesin motor complexes. This combined dynamics of motors and microtubules has been studied extensively in the last years and has become a paradigmatic system for biological self-organization [59–62]. The interest in the self-organization of asters is mainly due to the restructuring of the microtubule network during cell division, where an aster is transformed into the mitotic spindle and after the segregation of the chromosomes two asters form in the daughter cells [2,96]. However, the asters in a cell are three-dimensional structures, while those studied *in vitro* are quasi two-dimensional, since they are confined between two surfaces. Let us also mention, that asters of actin filaments have been observed as well, both *in vivo* [97] and *in vitro* [98].

In the following, we will not consider the self-organization of the asters, but the simpler case, where the asters have been formed and fixed, so that the action of motors does not change their structure. In that case, directed motion of motors along the filaments and diffusive motor currents will again be balanced in a stationary state, just as in the case of the tube discussed above. For the aster geometry some theoretical and experimental results have recently been reported by Nédélec *et al.* [87]. We recover their main theoretical result, an algebraic density profile far from the center of the aster, and extend the study of concentration profiles in asters by exploring the effect of exclusion interactions.

4.5.1 Two-state equations

Asters can be easily implemented in the two-state approach by substituting the coordinate x parallel to the tube axis with the radius coordinate r in the aster and the tube cross-section ϕ with a corresponding radius-dependent quantity $\phi(r)$, defined as the ratio of the free surface

(i.e. not covered by filaments) to the area covered by filaments,

$$\phi(r) = \frac{2\pi r h - N_f A_0}{N_f A_0} \approx \frac{2\pi r h}{N_f A_0} = \phi_0 r, \quad (4.46)$$

where N_f is the number of filaments, $A_0 = \ell^2$ is the cross-section of a single filament 'channel', and h is the height of the slab, into which the aster is confined. We thus obtain the following equations for the case of motors moving outwards in an aster:

$$v_b \rho_b(r) [1 - \rho_b(r+1)] = D_{ub} \phi(r) [\rho_{ub}(r+1) - \rho_{ub}(r)] \quad (4.47)$$

$$v_b \rho_b(r) [1 - \rho_b(r+1)] - v_b \rho_b(r-1) [1 - \rho_b(r)] = \tilde{\pi}_{ad} \rho_{ub}(r) [1 - \rho_b(r)] - \tilde{\epsilon} \rho_b(r). \quad (4.48)$$

At the boundaries, the equations have to be adapted as in the case of the tube, and the normalization, which fixes the total number of motors, yields an additional equation,

$$\sum_{r=0}^L [\rho_b(r) + \phi(r) \rho_{ub}(r)] = \frac{N}{A_0 N_f}. \quad (4.49)$$

Neglecting hard core exclusion and taking the continuum limit, we obtain

$$v_b \rho_b = \phi_0 r D_{ub} \frac{\partial \rho_{ub}}{\partial r} + D_b \frac{\partial \rho_b}{\partial r} \quad (4.50)$$

$$v_b \frac{\partial \rho_b}{\partial r} - D_b \frac{\partial^2 \rho_b}{\partial r^2} = \tilde{\pi}_{ad} \rho_{ub} - \tilde{\epsilon} \rho_b. \quad (4.51)$$

In the case $D_b = 0$, these equations are equivalent to those used by Nédélec *et al.* to describe their experimental results [87]. From these equations we get

$$v_b \rho_b = D_{ub} \phi_0 r \left(\frac{\tilde{\epsilon}}{\tilde{\pi}_{ad}} \frac{\partial \rho_b}{\partial r} + \frac{v_b}{\tilde{\pi}_{ad}} \frac{\partial^2 \rho_b}{\partial r^2} - \frac{D_b}{\tilde{\pi}_{ad}} \frac{\partial^3 \rho_b}{\partial r^3} \right) + D_b \frac{\partial \rho_b}{\partial r}. \quad (4.52)$$

To recover the asymptotic solution given in Ref. [87] we assume $\rho_b \sim r^\eta$ and neglect terms of order $r^{\eta-1}$. We obtain $\eta = \tilde{\pi}_{ad} v_b / (\tilde{\epsilon} \phi_0 D_{ub})$. Note that the bound diffusion coefficient does not contribute to the result in this limit. Interestingly, neglecting terms of order $r^{\eta-1}$ is equivalent to the assumption that attachment to and detachment from the filament are balanced locally. Hence asymptotically, bound and unbound density are related by $\rho_b = \frac{\tilde{\epsilon}}{\tilde{\pi}_{ad}} \rho_{ub}$, in contrast to the case of the tube.⁶ The case with hard core exclusion is again studied numerically.

If motion of motors is directed inwards in the aster (i.e. $v_b < 0$), Eqs. (4.47) and (4.48) must be slightly modified. In this case, the two-state equations are

$$v_b \rho_b(r+1) [1 - \rho_b(r)] = \phi(r) D_{ub} [\rho_{ub}(r+1) - \rho_{ub}(r)] \quad (4.53)$$

$$v_b \rho_b(r+1) [1 - \rho_b(r)] - v_b \rho_b(r) [1 - \rho_b(r-1)] = \tilde{\pi}_{ad}(r) \rho_{ub}(r) [1 - \rho_b(r)] - \tilde{\epsilon} \rho_b(r). \quad (4.54)$$

The asymptotic behaviour of the linearized equations discussed above remains unchanged. However, the exponent η is negative in this case and the profiles decrease for large r .

⁶Note that our densities ρ_b and ρ_{ub} are defined with respect to a lattice site of volume ℓ^3 , while the densities used by Nédélec *et al.* in Ref. [87] are defined with respect to a larger volume, which includes regions occupied by filaments as well as regions without filaments; in particular this implies that their density of bound motors, $b(r)$, is related to $\rho_b(r)$ by $b(r) \sim \rho_b(r)/r$.

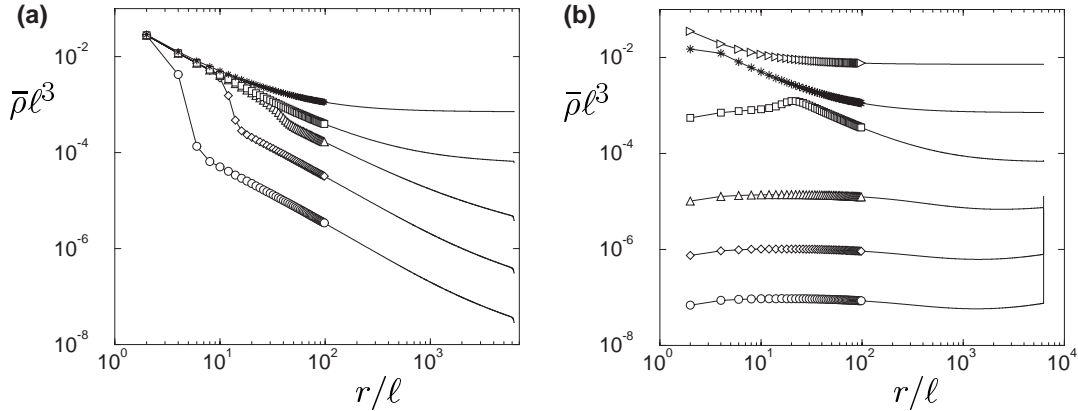


Figure 4.7: Concentration profiles for motors moving (a) inwards and (b) outwards in aster geometries as functions of the radial coordinate r . Parameters are for motor complexes as described by Nédélec *et al.* [87], see text. The numbers of motors are (from bottom to top) $N = 10^4$ (\circ), 10^5 (\diamond), 10^6 (\triangle), 10^7 (\square), 10^8 (\star), 10^9 (\triangleright). The profiles shown are profiles of the total motor concentration $\bar{\rho} \simeq \rho_b/\phi(r) + \rho_{ub}$. Because of the logarithmic scale, discrete data points are only indicated for small r .

4.5.2 Numerical results

To study the effect of hard core exclusion in asters, we used the parameters given by Nédélec *et al.* for the motor constructs used in their experiments [87]. In the numerics all parameters are given in units of the microtubule periodicity $\ell = 8 \text{ nm}$ and the step time $\tau_s = 10 \text{ ms}$. Parameters of the bound state are: $v_b = 0.8 \mu\text{m/s} = \ell/\tau_s$ and $\tilde{\epsilon} = 0.01 \tau_s^{-1}$ corresponding to detachment after 100 steps, and those of the unbound state: $D_{ub} = 20 \mu\text{m}^2/\text{s} = 3125 \ell^2/\tau_s$ and $\tilde{\pi}_{ad} = 2.6 \mu\text{m}^2\text{s}^{-1}/A_0 = 405.6 \tau_s^{-1}$. Parameters which correspond to kinesin with beads as used above for the case of the tube and in Ref. [56] give similar results. All results shown in the following are obtained for an aster of $N_f = 300$ microtubules of length $50 \mu\text{m} = 6250 \ell$, which is confined in a slab of height $9 \mu\text{m} = 1125 \ell$.

Motors moving inwards

We consider first the case, where motors move inwards. For this case, experimental results have been reported by Nédélec *et al.* [87]. Accumulation of motors in the center of the aster can be clearly observed by fluorescence microscopy. Profiles of the total motor concentration, i.e. the concentration averaged over bound and unbound motors,

$$\bar{\rho}(r) = \frac{\rho_b(r) + \phi(r)\rho_{ub}(r)}{1 + \phi(r)} \simeq \frac{1}{\phi(r)}\rho_b + \rho_{ub}, \quad (4.55)$$

can be extracted from the fluorescence images. As $\phi(r) \sim r$, this density exhibits a crossover from a decay $\sim r^{\eta-1}$ for small r to $\sim r^\eta$ for large r . This crossover behaviour is seen in the experimental data [87].

These results correspond to what is expected from the linearized theory, which should be appropriate for small motor concentrations. The question is now which additional features of

the profiles can be expected, when higher motor concentrations are considered and exclusion effects cannot be neglected.

For small total numbers of motors, the numerical solution of the master equations exhibits the power law behaviour predicted by neglecting exclusion effects. For the chosen parameters we find $\rho_{\text{ub}}(r) \sim r^{-0.54}$. The power law decay of the density profile can, however, only be found for very small motor concentration. In addition, already for small total number of motors, a 'traffic jam' is obtained in the center of the aster, which is however quite small. Interestingly, the traffic jam does not grow much in length, when the number of motors in the system is increased. In any case, jamming of motors occurs only for small radii ($< 1\mu\text{m}$), for which no experimental data are available.⁷ The main effect of the hard core exclusion is that density profiles get more and more flat with increasing motor concentration in the system, see Fig. 4.7(a).

The average current in the system exhibits again a maximum at an optimal motor concentration. The maximum occurs at a motor concentration, where the bound motor density becomes nearly constant and the power law behaviour is hardly identified.

Motors moving outwards

For motors moving outwards in an aster we obtain profiles as shown in Fig. 4.7(b). For small numbers of motors (and not too close to the boundaries) the bound density follows the power law predicted by the linear equations. Again the profile of the bound density gets flatter with increasing motor concentration.

The new feature compared to the previous case is that the profile of the total motor concentration, which is rather flat for small motor concentration, develops a pronounced maximum in the center of the aster as the number of motors is increased beyond the optimal motor concentration, see Fig. 4.7(b). This can be understood in the following way: If no ATP is added to the system, motors will accumulate in the center of the aster, simply because they bind strongly to the filaments, and in the center the number of binding sites per unit area is maximal. If ATP is added, motors are driven outwards by directed motion. If now the number of motors in the system is increased, so that motion is slowed down by the exclusion effect, the outward drift is suppressed and accumulation in the center is successively restored.

4.6 Summary

In this chapter, we have discussed stationary concentration profiles in closed compartments. The stationary states in these systems are characterized by a balance of directed currents along the filaments and diffusive currents of unbound motors. We have argued that local concentrations of motors can become large even at small overall motor concentration. Therefore exclusion effects play an important role and the concentration profiles depend on the overall motor concentration or the total number of motors in the compartments.

In the case of the tube geometry, our results show that for small overall motor concentrations, motors are exponentially localized at the end of the tube towards which their movement is directed, while for large overall motor concentrations, motors are spread over the whole

⁷If the detachment rate at the filament end, i.e. in the center of the aster, is higher than at other sites, no 'traffic jam' is found. Apart from this, profiles agree perfectly with those for the case of slow detachment at the end.

length of the filament, however, blocking each other by hard core exclusion, so that the average current is small. The maximal current is obtained at an intermediate optimal motor concentration, where motors explore the whole length of the tube, but mutual blocking is still sufficiently small.

In the case of motors moving inwards in an aster-like arrangement of filaments, a profile decaying as a power law is found at low overall motor concentrations. For larger motor concentrations, this profile flattens. Finally, for motors moving outwards in an aster, exclusion effects result in the formation of a concentration peak in the center of the aster, as motors are slowed down by increasing the overall motor concentration.

The predictions for both geometries can be tested experimentally. Let us repeat that recently experimental concentration profiles have been reported for the case of asters [87] and that localization of motors at the tube end has been observed in tube-like compartments *in vivo* [89]. Both observations concern the case of small overall motor concentration and are recovered by our calculations. Similar experiments could be performed to study the case of larger motor concentrations, for which we have made the predictions summarized above.

Chapter 5

Motor traffic through open tube-like compartments

In this chapter, we turn our attention again to tube-like compartments. We consider now stationary states in open tubes which are coupled to reservoirs of motors at both ends. Motors can enter and leave the tube at its ends and the motor traffic through the tube is characterized by a stationary current. The density of filament-bound motors can again become large, so that mutual exclusion from binding sites is important. Under these conditions, our models exhibit boundary-induced phase transitions related to those of the one-dimensional asymmetric simple exclusion process (ASEP). The location of the transition lines depends on the boundary conditions at the two ends of the tubes [58].

In the following, we will discuss three types of boundary conditions: (A) Periodic boundary conditions which correspond to a closed torus-like tube; (B) fixed motor densities at the two tube ends where radial equilibrium holds locally; and (C) diffusive motor injection at one end and diffusive motor extraction at the other end. We will determine the phase diagrams and the profiles for the bound and unbound motor densities using mean field approximations and Monte Carlo simulations.

5.1 Open tube systems

We consider the motion of molecular motors in a cylindrical tube of length L and radius R as shown in Fig. 5.1. The tube contains one filament located along its symmetry axis which is again taken to be the x -axis. The total number of motors in the tube is denoted by N . In the case of open boundaries, N is not fixed, but its stationary value is determined by the motor concentrations in the reservoirs at the tube ends. In general, one cannot expect N or the overall motor concentration in the tube to remain sufficiently small, therefore mutual exclusion between motors cannot be neglected. Remember that hard core exclusion is important even at relatively small overall motor concentrations, since the motors are strongly attracted to the binding sites of the filament, so that a large fraction of them is in the bound state.

As mentioned before, our models are variants of driven lattice gas models and exclusion processes, for which the active processes which drive the particles are localized to the filaments. Studying open tube geometries is motivated by results for the one-dimensional asymmetric simple exclusion process (ASEP), a simple model for biased hopping of particles on a one-dimensional lattice with mutual exclusion from lattice sites. When coupled to open boundaries,

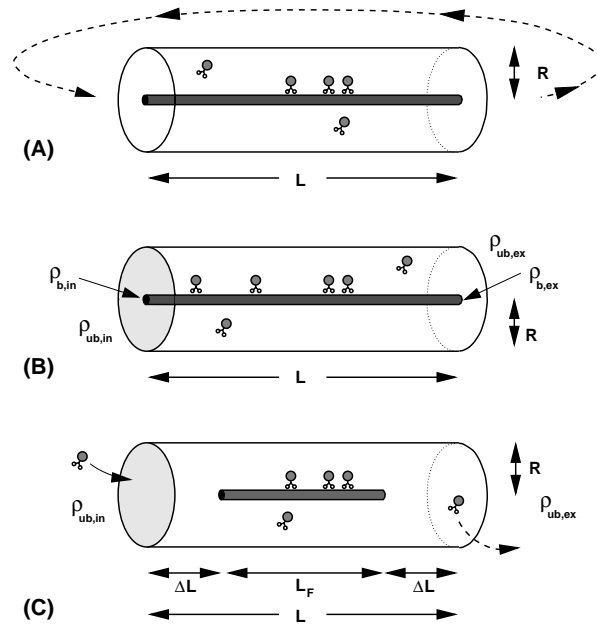


Figure 5.1: Different types of boundary conditions: (A) Periodic boundary conditions which correspond to a closed torus geometry; (B) Open tube with boundaries satisfying radial equilibrium: the bound and unbound motor densities are fixed at the two boundaries and satisfy radial detailed balance at each boundary; and (C) Open tube with diffusive injection and extraction of motors. In all cases, the tube has total length L ; in cases (A) and (B), the filament has the same length as the tube; in case (C), the filament has length $L_F < L$ and there are two boundary compartments of linear size ΔL .

this simple model already exhibits a complex phase diagram, see e.g. [75], which we will review below in some detail. This model was first introduced in 1968 by MacDonald *et al.* [99,100] in the context of protein synthesis by ribosomes on messenger RNA (mRNA). At that time it was solved using a mean field approach and used to explain results of radioactive labeling experiments [101–103] which showed that protein synthesis gets slower as the ribosome moves on the mRNA template. The model of MacDonald *et al.* explained this by the steric hindrance between successive ribosomes along the mRNA track. Since then, the ASEP has become a generic model for non-equilibrium phase transitions [74] and has also been used in other applications such as traffic flow [72]. Many properties of the one-dimensional ASEP are known exactly [104,105].

Let us stress again that the lattice models for the random walks of molecular motors differ from the usual driven lattice gas models in the following way: Walks of molecular motors are only 'driven' as long as the motor is attached to a cytoskeletal filament, hence 'driving' is localized to one or several lines. It can therefore be viewed as an ASEP coupled to a *symmetric* exclusion process via binding to and unbinding from the filament.

Boundary conditions play an important role in driven systems. This becomes apparent, e.g., if one compares a tube-like system with periodic boundary conditions with one with closed boundaries. In the systems with closed boundaries discussed in the previous chapter, a traffic jam of motors arises at one end of the system and the current of motors bound to

the filament is balanced by diffusive currents of unbound motors. With periodic boundary conditions, motors arriving at the right end of the system just restart their walk from the left end and a net current through the systems is obtained.

Compared to the one-dimensional ASEP, the tube geometries considered here, leave more freedom to choose the boundary conditions. In the following, we will discuss three different types of boundary conditions as shown in Fig. 5.1. As we will demonstrate for these three cases, the stationary states depend strongly on the way, in which the motors are inserted and extracted at the boundaries.

Let us finally mention that the stationary states in open tube-like compartments studied in this chapter are accessible to *in vitro* experiments using standard motility assays. In addition, traffic in these open tubes can also be viewed as a strongly simplified model for motor-based transport in an axon [42], if these motors, which are synthesized in the cell body, are at least partly degraded at the axon terminal [92], a situation that can be mimicked by insertion and extraction of motors at the ends of a tube.

5.2 Periodic boundary conditions

First we consider a cylindrical tube with periodic boundary conditions in the longitudinal direction. Because of the translational invariance in the direction parallel to the filament, there are no net radial currents, i.e., there is a bound current j_b on the filament, but both currents of motors binding to and unbinding from the filament *and radial currents of unbound motors* are balanced locally, a situation which we call *radial detailed balance* or *radial equilibrium*. If there is only one unbound channel, $N_{\text{ch}} = 1$, (or N_{ch} equivalent channels) radial equilibrium is equivalent to adsorption equilibrium. It is clear, that this will no longer be true, if translational invariance is broken by boundaries or blocked sites on the filament. Another important property of systems with periodic boundary conditions is that, in this case, the number N of motors in the system is conserved, which does not apply to open systems.

Because of translational invariance along the x -axis, the bound and unbound motor densities, ρ_b and ρ_{ub} , do not depend on x . In addition, it follows from the absence of radial currents, that ρ_{ub} is also independent of the radial coordinate r . Hence, ρ_b and ρ_{ub} are constant, and radial equilibrium implies the relation

$$\frac{\epsilon}{6}\rho_b(1 - \rho_{\text{ub}}) = \frac{\pi_{\text{ad}}}{6}\rho_{\text{ub}}(1 - \rho_b) \quad (5.1)$$

which leads to

$$\rho_b = \frac{\rho_{\text{ub}}}{\epsilon/\pi_{\text{ad}} + (1 - \epsilon/\pi_{\text{ad}})\rho_{\text{ub}}}. \quad (5.2)$$

Since the total number N of motors is conserved, we can use the normalization condition,

$$\rho_b + N_{\text{ch}}\rho_{\text{ub}} = \frac{N}{L}, \quad (5.3)$$

to obtain a quadratic equation for the densities as a function of the system size and the total number of motors. Since one root is always negative, the physically meaningful solution is:

$$\rho_{\text{ub}} = \frac{\frac{N}{L}(1 - \frac{\epsilon}{\pi_{\text{ad}}}) - 1 - N_{\text{ch}}\frac{\epsilon}{\pi_{\text{ad}}} + \sqrt{\left[\frac{N}{L}(1 - \frac{\epsilon}{\pi_{\text{ad}}}) - 1 - N_{\text{ch}}\frac{\epsilon}{\pi_{\text{ad}}}\right]^2 + 4N_{\text{ch}}(1 - \frac{\epsilon}{\pi_{\text{ad}}})\frac{\epsilon}{\pi_{\text{ad}}}\frac{N}{L}}}{2N_{\text{ch}}(1 - \epsilon/\pi_{\text{ad}})}. \quad (5.4)$$

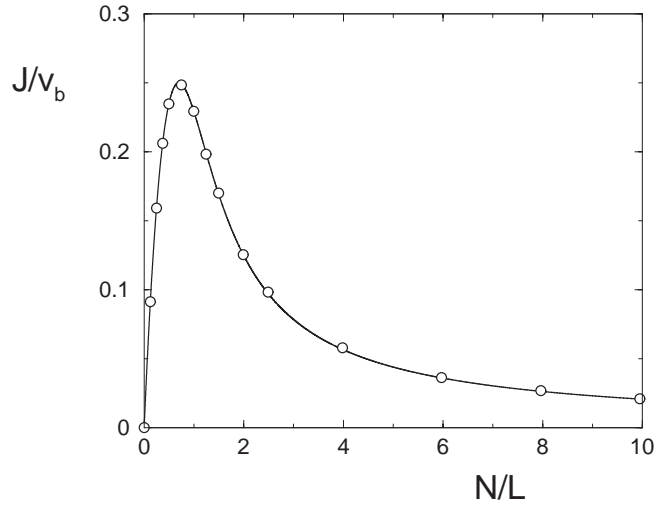


Figure 5.2: Reduced current J/v_b through the tube with periodic boundary conditions as a function of the reduced particle number N/L . The line is calculated from Eq. (5.4), the Monte Carlo data are obtained for a tube of length $L = 200$ and radius $R = 25$ corresponding to channel number $N_{\text{ch}} = 1940$. The random walk probabilities are $\beta = 0$, $\gamma = 99/100$, $\epsilon = 10^{-4}$, $\alpha = 1 - \gamma - 2\epsilon/3$, and $\pi_{\text{ad}} = 1$.

From this expression for the unbound density, the bound density ρ_b follows via Eq. (5.2) and the stationary current is given by $J = j_b = v_b \rho_b (1 - \rho_b)$. The current calculated in this way is shown in Fig. 5.2 as a function of N/L . The data points (circles) are the results of Monte Carlo simulations for a system of length $L = 200$ and radius $R = 25$ and are in very good agreement with the analytical solution.

It follows from the analytical solution that the current $J = j_b$ vanishes at $N/L = 1 + N_{\text{ch}}$, behaves as

$$\frac{J}{v_b} \approx \frac{1}{1 + \frac{\epsilon}{\pi_{\text{ad}}} N_{\text{ch}}} \frac{N}{L} \quad \text{for small } N/L, \quad (5.5)$$

and has the maximal value $\max(J) = v_b/4$ for

$$\rho_b = 1/2, \quad \rho_{\text{ub}} = \frac{\epsilon/\pi_{\text{ad}}}{1 + \epsilon/\pi_{\text{ad}}} \quad \text{and} \quad \frac{N}{L} = \frac{1}{2} + N_{\text{ch}} \frac{\epsilon/\pi_{\text{ad}}}{1 + \epsilon/\pi_{\text{ad}}}. \quad (5.6)$$

Let us add two remarks: (i) Eq. (5.1), as stated here, can be considered as a mean field equation. However, using the quantum Hamiltonian representation of the stochastic process, it can be shown to hold exactly, see appendix D.1.

(ii) Note that in contrast to a homogeneously driven lattice gas such as the asymmetric simple exclusion process, there is no particle hole symmetry here. Particles attempt to leave the filament with rate $\epsilon/6$ to a neighbouring site while holes do so with rate $\pi_{\text{ad}}/6$, i.e., particles are strongly attracted by the filament, while holes are not. However, if one considers only the bound density, the current–density relationship $J = j_b = v_b \rho_b (1 - \rho_b)$ is invariant under the exchange of particles and holes. As we will see in the next section, this can lead to an apparent particle hole symmetry for systems with radial equilibrium, for which the radial currents vanish and the state of the system can be determined by the bound density alone.

5.3 Open boundaries with radial equilibrium

Now, let us consider the more interesting case, where the tube is open and the densities at the left and right boundary are fixed. To be precise, we consider two different sets of boundary conditions, (B) and (C) as shown schematically in Fig. 5.1. In this section, we study case (B) while case (C) will be considered in the following section 5.4.

For case (B), we add two layers of boundary sites at $x = 0$ and $x = L + 1$ with $y_1^2 + y_2^2 \leq R^2$. As before, the filament is located at $y_1 = y_2 = 0$. The filament is taken to extend into the boundary layers and we fix the density on the additional filament sites according to

$$\rho_b(x = 0) \equiv \rho_{b,\text{in}} \quad \text{and} \quad \rho_b(x = L + 1) \equiv \rho_{b,\text{ex}}, \quad (5.7)$$

see Fig. 5.1. Furthermore, the densities on the non-filament boundary sites, $\rho_{\text{ub},\text{in}}$ and $\rho_{\text{ub},\text{ex}}$, are chosen in such a way that radial equilibrium as given by Eq. (5.1) holds at both boundaries.

Motors from within the tube can now leave the tube by hopping to a lattice site of one of the boundary layers. In addition, motors enter the tube from lattice sites of the boundary layers according to the fixed densities, see appendix A for details. Note that the probabilities for hopping attempts at lattice sites of the boundary layers are the same as within the tube and depend on whether the chosen site is a filament or non-filament site. Throughout this section, we take $\beta = \gamma = 0$ to eliminate two parameters from the problem.

5.3.1 Phase diagram

In the limiting case with $N_{\text{ch}} = 0$ and $\epsilon = 0$, our system becomes equivalent to the one-dimensional ASEP, for which the density profiles and the phase diagram are known exactly [104, 105]. Let us therefore summarize some of the known properties of this process, for which we use symbols without the subscript 'b'.

For the one-dimensional ASEP, there are three different phases. If the density ρ_{in} at the left boundary is small and satisfies $\rho_{\text{in}} < 1/2$ and if the density ρ_{ex} at the right boundary is not too large with $\rho_{\text{ex}} < 1 - \rho_{\text{in}}$, the system is in the low density (LD) phase, for which the bulk density ρ^0 is equal to the left boundary density, and the current is given by $J = v\rho_{\text{in}}(1 - \rho_{\text{in}})$. Because of the particle hole symmetry, an analogous situation holds for $\rho_{\text{ex}} > 1/2$ and $\rho_{\text{in}} > 1 - \rho_{\text{ex}}$ [high density (HD) phase]. Now, the bulk density is given by $\rho^0 = \rho_{\text{ex}}$ and the current is $J = v\rho_{\text{ex}}(1 - \rho_{\text{ex}})$. At the line $\rho_{\text{ex}} = 1 - \rho_{\text{in}} < 1/2$, a discontinuous phase transition takes place, and the bulk density jumps from the left boundary value to the right boundary value. Finally, for $\rho_{\text{in}} > 1/2$ and $\rho_{\text{ex}} < 1/2$, the bulk density is $\rho^0 = 1/2$ and the current attains its maximal value $J = v/4$. Therefore, this phase is called maximal current (MC) phase. The phase transition towards the maximal current phase is continuous with a diverging correlation length.

The formation of three different phases can be understood in terms of the underlying dynamics of domain walls and density fluctuations [75]. In the low density and high density phases, the selection of the stationary state is governed by domain wall motion. Thus consider a domain wall, which forms between regions of different densities. If its velocity is positive, the domain wall travels to the right boundary and the bulk density is equal to the left boundary density (low density phase). Likewise, the bulk density is given by the right boundary density, if the domain wall velocity is negative (high density phase). At the transition line with $\rho_{\text{ex}} = 1 - \rho_{\text{in}} < 1/2$ the domain wall velocity is zero, and domain walls diffuse through the system.

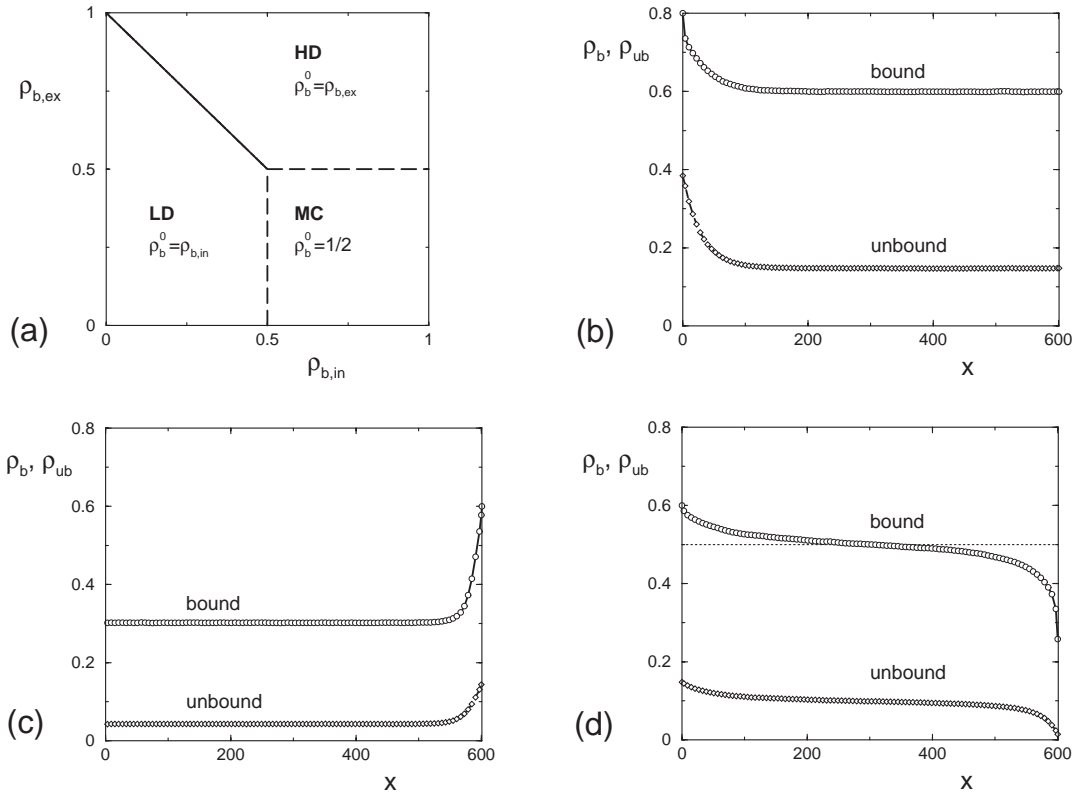


Figure 5.3: (a) Phase diagram for motor traffic in open tubes with boundary condition (B) as a function of the boundary densities $\rho_{b,in}$ and $\rho_{b,ex}$ at the left and right end of the filament, respectively. There are three phases distinguished by the bulk value of the bound density ρ_b^0 : a low density phase (LD), a high density phase (HD), and a maximal current phase (MC). This phase diagram is identical to the phase diagram of the one-dimensional ASEP as explained in the text. (b)–(d) Typical profiles of the bound and unbound densities as functions of the coordinate x parallel to the filament for (b) the high density phase with $\rho_{b,in} = 0.8$ and $\rho_{b,ex} = 0.6$; (c) the low density phase with $\rho_{b,in} = 0.3$ and $\rho_{b,ex} = 0.6$; and (d) the maximal current phase with $\rho_{b,in} = 0.6$ and $\rho_{b,ex} = 0.1$. Data have been obtained by simulations for a tube of length $L = 600$ and radius $R = 10$ and random walk probabilities $\beta = \gamma = 0$, $\epsilon = 10^{-2}$, $\alpha = 1 - 2\epsilon/3$, and $\pi_{ad} = 1$. The shown data points are averages over six lattice sites along the x -axis and the unbound density has been averaged over the tube cross section and multiplied by a scale factor of 10.

The second mechanism is related to density fluctuations. If a small perturbation of the density, corresponding, e.g., to some added particles, enters the system at the left boundary, it can move with positive or negative velocity, i.e., it can spread into the bulk or is driven back towards the boundary. In the maximal current phase the velocity of such density perturbations, is negative and density fluctuations coming from the left boundary are driven back to the boundary. Hence, increasing ρ_{in} does not increase the bulk density, since additional particles cannot enter the system (overfeeding effect). Both the velocities of domain walls and of density fluctuations are governed by the same density–current relation which is $j = v\rho(1 - \rho)$ for the

one-dimensional ASEP [75].

For the filament in a tube as considered here, the velocities of domain walls and density fluctuations are similar to those for the ASEP in one dimension. This can be understood from the fact that the current–density relationship on the filament is the same as for the one-dimensional ASEP provided one rescales all currents by the factor $(1 - 2\epsilon/3)$ which arises from the possibility to unbind from the filament.

Thus, let us first consider the case, where the behaviour on the filament is determined by domain walls, i.e. the low density and high density phases. The domain wall velocity v_s is slowed down compared to the case of the ASEP in one dimension, but changes sign at the same values of the boundary densities. An explicit expression for v_s can be obtained from the general expression for the domain wall velocity as given in Ref. [75] by integrating the density over the tube cross-section, which leads to

$$v_s = \frac{v_b \rho_{b,\text{ex}}(1 - \rho_{b,\text{ex}}) - v_b \rho_{b,\text{in}}(1 - \rho_{b,\text{in}})}{\rho_{b,\text{ex}} - \rho_{b,\text{in}} + N_{\text{ch}} \rho_{\text{ub},\text{ex}} - N_{\text{ch}} \rho_{\text{ub},\text{in}}} \quad (5.8)$$

for the geometry considered here. Remember that the unbound densities are related to the bound densities by radial equilibrium at the boundaries. If a domain wall spreads from the left or right boundary into the system, radial equilibrium will hold approximately in the bulk because of translational invariance, but, in addition, all the way down to the dominating boundary, where we have imposed radial equilibrium via the boundary conditions. Therefore, the current and the bulk density are determined by the bound density at the boundaries.

The drift velocity of fluctuations of the bound density is $v_c = 1 - 2\rho_b$ [75]. If the behaviour on the filament is determined by this velocity, i.e. in the case $\rho_{b,\text{in}} > 1/2$ and $\rho_{b,\text{ex}} < 1/2$, radial equilibrium will not hold up to the boundary and unbound motors can enter the tube. However, after a short distance they will bind to the filament and act like an additional particle in the maximal current phase: The density fluctuation generated by the additional particle moves towards the boundary. Therefore in the bulk, the bound density is $1/2$ and the current is $v_b/4$.

Summarizing these considerations, we predict to find exactly the same phase diagram as for the one-dimensional ASEP; see Fig. 5.3 which also shows typical density profiles for the three phases. In fact, we have chosen our boundary conditions (B) in such a way that we only have to replace the density ρ of the one-dimensional ASEP by the bound density ρ_b and the boundary densities ρ_{in} and ρ_{ex} by the boundary densities on the filament, $\rho_{b,\text{in}}$ and $\rho_{b,\text{ex}}$. The unbound density in the bulk is obtained by radial equilibrium from the bound density. These expectations are confirmed (i) by a detailed analysis of the discrete mean field equations, see appendix D.2, and (ii) by extended Monte Carlo simulations.

A remarkable feature of the phase diagram is that it seems to exhibit particle hole symmetry, while the dynamics does not. The signature of particle hole symmetry in the phase diagram is the symmetry between the high density and low density phase. In both these phases, the bulk density is approximately constant and radial equilibrium holds approximately in the whole system except close to the left or right boundary. Radial equilibrium holds exactly at that boundary which determines the bulk behaviour. Therefore radial currents vanish on average and the phase diagram is determined by the bound density alone, resulting in a phase diagram which gives the impression of particle hole symmetry, although this symmetry is broken. Indeed, even though the substitution of the bound density ρ_b by $1 - \rho_b$ leads to the same bound current j_b , it does not lead to the unbound density $1 - \rho_{\text{ub}}$. Two stationary states with bound densities that are related through exchange of particles and holes are characterized

by two unbound densities which are both smaller than the bound ones and thus break the apparent symmetry.

5.3.2 Density profiles

To discuss the concentration profiles of the bound and unbound motors, we use continuum mean field equations and compare the mean field results with simulations. We use again the two-state approximation introduced in chapter 2.5, i.e., we consider the case of a single unbound channel, so that a motor can be in only two states, bound to the filament or unbound. Remember that the two-state model is exact for an arbitrary number N_{ch} of *equivalent* unbound channels, but can also serve as an approximation for the original tube systems because the unbound density depends only weakly on the radial coordinate. Within this approximation, the bound motors are described by the density $\rho_{\text{b}}(x)$ and the unbound motors by the density $\rho_{\text{ub}}(x)$. The effective diffusion coefficient for the unbound motors is given by $N_{\text{ch}}D_{\text{ub}}$.

Using the mean field approximation, the total current J parallel to the tube axis is now given by

$$J = v_{\text{b}}\rho_{\text{b}}(1 - \rho_{\text{b}}) - D_{\text{b}}\frac{\partial\rho_{\text{b}}}{\partial x} - N_{\text{ch}}D_{\text{ub}}\frac{\partial\rho_{\text{ub}}}{\partial x} \quad (5.9)$$

and the equality between incoming and outgoing currents at any lattice site leads to

$$\frac{\partial}{\partial x}\left[v_{\text{b}}\rho_{\text{b}}(1 - \rho_{\text{b}}) - D_{\text{b}}\frac{\partial\rho_{\text{b}}}{\partial x}\right] = \tilde{\pi}_{\text{ad}}\rho_{\text{ub}}(1 - \rho_{\text{b}}) - \tilde{\epsilon}\rho_{\text{b}}(1 - \rho_{\text{ub}}), \quad (5.10)$$

where we have again introduced the rescaled binding and unbinding rates, $\tilde{\pi}_{\text{ad}} = \frac{2}{3}\pi_{\text{ad}}$ and $\tilde{\epsilon} = \frac{2}{3}\epsilon$.

In order to determine the density profiles far from the boundaries, we first calculate the homogeneous, x -independent solutions, ρ_{b}^0 and ρ_{ub}^0 , of the two mean field equations (5.9) and (5.10). The first equation (5.9) for the total current J then reduces to the current–density relationship

$$J = v_{\text{b}}\rho_{\text{b}}^0(1 - \rho_{\text{b}}^0) \quad (5.11)$$

whereas the second equation (5.10) becomes

$$\tilde{\pi}_{\text{ad}}\rho_{\text{ub}}^0(1 - \rho_{\text{b}}^0) = \tilde{\epsilon}\rho_{\text{b}}^0(1 - \rho_{\text{ub}}^0) \quad (5.12)$$

which implies radial equilibrium for the x -independent solutions.

We then decompose the densities according to

$$\rho_{\text{b}}(x) = \rho_{\text{b}}^0 + \eta_{\text{b}}(x) \quad \text{and} \quad \rho_{\text{ub}}(x) = \rho_{\text{ub}}^0 + \eta_{\text{ub}}(x), \quad (5.13)$$

and expand the mean field equations (5.9) and (5.10) in powers of the density deviations η_{b} and η_{ub} . As a result, we obtain

$$D_{\text{b}}\frac{\partial}{\partial x}\eta_{\text{b}} + N_{\text{ch}}D_{\text{ub}}\frac{\partial}{\partial x}\eta_{\text{ub}} = v_{\text{b}}(1 - 2\rho_{\text{b}}^0)\eta_{\text{b}} - v_{\text{b}}\eta_{\text{b}}^2 \quad (5.14)$$

and

$$v_{\text{b}}(1 - 2\rho_{\text{b}}^0)\frac{\partial}{\partial x}\eta_{\text{b}} - 2v_{\text{b}}\eta_{\text{b}}\frac{\partial}{\partial x}\eta_{\text{b}} - D_{\text{b}}\frac{\partial^2}{\partial x^2}\eta_{\text{b}} = A\eta_{\text{ub}} - B\eta_{\text{b}} + (\tilde{\epsilon} - \tilde{\pi}_{\text{ad}})\eta_{\text{ub}}\eta_{\text{b}}, \quad (5.15)$$

where we have defined

$$A \equiv \tilde{\pi}_{\text{ad}}(1 - \rho_{\text{b}}^0) + \tilde{\epsilon}\rho_{\text{b}}^0 \quad \text{and} \quad B \equiv \tilde{\epsilon}(1 - \rho_{\text{ub}}^0) + \tilde{\pi}_{\text{ad}}\rho_{\text{ub}}^0. \quad (5.16)$$

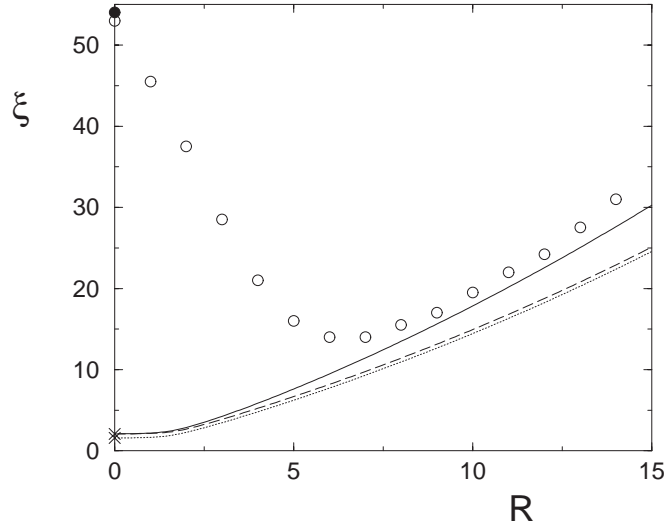


Figure 5.4: Localization length ξ as a function of the tube radius R for boundary conditions (B) with $\rho_{b,\text{in}} = 0.38$ and $\rho_{b,\text{ex}} = 0.6$. Circles are simulation data, obtained for a tube of length $L = 600$ and with random walk probabilities as in Fig. 5.3; lines are the corresponding results of mean field calculations (dotted: discrete two-state approximation, dashed: continuous two-state approximation, solid: full diffusion equation, see text). The two crosses and the filled circle at $R = 0$ represent the mean field results and the exact result for the one-dimensional ASEP, respectively.

Low density and high density phases

For the high and low density phases with $\rho_b^0 \neq 1/2$, Eqs. (5.14) and (5.15) up to first order in η_b and η_{ub} lead to an exponential approach $\sim \exp(x/\xi)$ of the density profiles towards the homogeneous solutions ρ_b^0 and ρ_{ub}^0 . The corresponding decay length ξ satisfies the cubic equation

$$-v_b(1 - 2\rho_b^0)\xi^3 + (D_b + N_{\text{ch}}D_{\text{ub}}g)\xi^2 + N_{\text{ch}}D_{\text{ub}}\frac{v_b(1 - 2\rho_b^0)}{A}\xi - N_{\text{ch}}D_{\text{ub}}\frac{D_b}{A} = 0 \quad (5.17)$$

with $g \equiv B/A$. Eq. (5.17) is solved numerically.

For the ASEP in one dimension, one has $N_{\text{ch}} = 0$ and Eq. (5.17) reduces to $-v_b(1 - 2\rho_b^0)\xi^3 + D_b\xi^2 = -\xi^2(\xi - \xi_0) = 0$ with

$$\xi_0 \equiv \frac{D_b}{v_b(1 - 2\rho_b^0)}. \quad (5.18)$$

Thus, in this limit, mean field theory leads to the correlation length $\xi = \xi_0$. For $N_{\text{ch}} > 0$, we choose the unique solution of (5.17) which approaches (5.18) as N_{ch} vanishes. This solution behaves as $\xi \approx \xi_0(1 + gN_{\text{ch}}D_{\text{ub}}/D_b)$ for small N_{ch} .

In addition to the mean field calculation, we again used Monte Carlo simulations in order to determine the density profiles as shown in Fig. 5.3(b) and (c). As predicted by the mean field calculation, the constant bulk densities for the bound and unbound states are approached exponentially in the low and high density phases. The corresponding decay length ξ is found

to be the same for the bound and the unbound density and to diverge as one approaches the maximal current phase.

Some simulation results for the decay length ξ are displayed in Fig. 5.4. In this case, the radius R of the tube was varied while the boundary densities were kept fixed. The latter densities were chosen to be $\rho_{b,\text{in}} = 0.38$ and $\rho_{b,\text{ex}} = 0.6$ which lies within the low density phase but is close to the phase transition line which separates the low density from the high density phase. One surprising feature of the Monte Carlo data for the decay length ξ is that they exhibit a pronounced *minimum* as a function of tube radius R .

For comparison, we also display in Fig. 5.4 the ξ -values as obtained from several mean field approximations corresponding to the dashed, dotted and solid lines. The dashed line is obtained from the solution of equation (5.17) which we derived from the continuous mean field approximation for the two-state model. We also determined this quantity using a lattice version of this approximation (dotted line, see appendix D.2) and a more elaborate mean field approximation (solid line), in which we solved the diffusion equation in the cylindrical compartment and matched this solution to the directed transport along the filament. In the latter calculation we used the same technique that was used to determine the profile of the depletion zone in chapter 4.3.

Inspection of Fig. 5.4 shows that all three mean field approximations are quite consistent with each other and lead to $\xi \sim R^2$ as follows from (5.17). Such an increase of ξ for large R is in fair agreement with the Monte Carlo data displayed in Fig. 5.4. However, in contrast to the Monte Carlo simulations, all three mean field approximations give a *monotonic* increase of ξ with increasing R .

The largest discrepancy between the mean field results and the Monte Carlo data is found in the limit of small R for which one recovers the one-dimensional ASEP. In this limit, the Monte Carlo data should be quite reliable as one concludes from the value obtained for $R = 0$ which is in very good agreement with the exact solution for the one-dimensional ASEP as given by Ref. [104]. Thus, we conclude that the decay length ξ does indeed exhibit a nonmonotonic dependence on the tube radius R and that this behaviour is not reproduced by the mean field approximation.

Finally, we note that the different behaviour of the decay length ξ for large and for small R is correlated with a qualitatively different behaviour of the corresponding density profiles as observed in the Monte Carlo simulations. As an example, let us consider the density profiles within the low density phase as in Fig. 5.3(c). In this case, the bound and unbound densities exhibit plateau regions which are determined by their values $\rho_{b,\text{in}}$ and $\rho_{ub,\text{in}}$ at the left boundary. As one gets closer to the right boundary where the motors can leave the tube, the densities start to deviate from these constant values, and these deviations grow exponentially as $\sim \exp(x/\xi)$. For small R , the corresponding profiles are convex upwards for all values of x . For large R , on the other hand, the profile exhibits an inflection point close to the right boundary. This inflection point moves towards the interior of the tube as R is further increased.

Maximal current phase

In the maximal current phase, one has $\rho_b^0 = 1/2$, and one has to consider terms up to second order in the density deviations η_b and η_{ub} in Eqs. (5.14) and (5.15). We neglect terms of order $\eta_b \frac{\partial \eta_b}{\partial x}$ and $\frac{\partial^2 \eta_b}{\partial x^2}$ as can be justified *a posteriori* since η_b is found to decay as an inverse power of x . Thus, up to leading order, radial equilibrium holds for the asymptotic decay to

the homogeneous solution and we find

$$\eta_{\text{ub}} = \frac{B\eta_{\text{b}}}{A + (\tilde{\epsilon} - \tilde{\pi}_{\text{ad}})\eta_{\text{b}}} \approx g\eta_{\text{b}} - \frac{B(\tilde{\epsilon} - \tilde{\pi}_{\text{ad}})}{A^2}\eta_{\text{b}}^2 \quad (5.19)$$

for small η_{b} and therefore

$$\frac{\partial\eta_{\text{ub}}}{\partial x} = g\frac{\partial\eta_{\text{b}}}{\partial x} + O(\eta_{\text{b}}\frac{\partial\eta_{\text{b}}}{\partial x}). \quad (5.20)$$

If the latter expression is inserted into Eq. (5.14), one finds that η_{b} satisfies the nonlinear differential equation

$$(D_{\text{b}} + gN_{\text{ch}}D_{\text{ub}})\frac{\partial\eta_{\text{b}}}{\partial x} \approx -v_{\text{b}}\eta_{\text{b}}^2 \quad (5.21)$$

with $g \equiv B/A$. This differential equation can be solved by separation of variables. The solution behaves as

$$\eta_{\text{b}} \approx \frac{D_{\text{b}} + gN_{\text{ch}}D_{\text{ub}}}{v_{\text{b}}x} \quad \text{for large } x, \quad (5.22)$$

i.e., the deviation of the bound density from its asymptotic bulk value $\rho_{\text{b}}^0 = 1/2$ decays as $\sim 1/x$ within the mean field approximation.

For $N_{\text{ch}} = 0$, this becomes identical with the mean field solution for the ASEP in one dimension as discussed in [74]. In this latter case, an exact solution is available [104, 105], which shows that the density profile decays as $\sim 1/x^{1/2}$, i.e., with a different exponent. This is related to the fact that density fluctuations spread superdiffusively in the one-dimensional ASEP [106]. The dispersion $\langle(\Delta x)^2\rangle$ of an ensemble of particles in such a system behaves as $\langle(\Delta x)^2\rangle \sim t^{4/3}$ for large times t . This superdiffusive spreading of density fluctuations in one dimension can be taken into account within a mean field approximation if one considers a scale-dependent diffusion coefficient as shown in Ref. [74]. In the following, we will extend this approach to the tube geometry considered here.

Thus, we now replace D_{b} in the mean field equation (5.21) by a scale-dependent diffusion coefficient $D_{\text{b}}(x)$ and consider the modified mean field equation

$$[D_{\text{b}}(x) + gN_{\text{ch}}D_{\text{ub}}]\frac{\partial\eta_{\text{b}}}{\partial x} \approx -v_{\text{b}}\eta_{\text{b}}^2. \quad (5.23)$$

A convenient choice for $D_{\text{b}}(x)$ which embodies the correct superdiffusive behaviour for the ASEP in one dimension is

$$D_{\text{b}}(x) \equiv D_{\text{sc}} \left(1 + \sqrt{\frac{x - x_0}{x_{\text{sc}}}} \right). \quad (5.24)$$

The left boundary is located at $x = x_0$ ($= 0$ in our simulations), and D_{sc} and x_{sc} represent two scale parameters. With this choice, the modified mean field equation (5.23) can again be solved by separation of variables. As a result, we obtain

$$\eta_{\text{b}}(x) = a \left[\frac{a}{\eta_{\text{b}}(x_0)} + \sqrt{\tilde{x}} - b \ln(1 + \sqrt{\tilde{x}}/b) \right]^{-1}, \quad (5.25)$$

where we have introduced the abbreviations $\tilde{x} \equiv (x - x_0)/x_{\text{sc}}$, $a \equiv D_{\text{sc}}/(2v_{\text{b}}x_{\text{sc}})$, and $b \equiv 1 + gN_{\text{ch}}D_{\text{ub}}/D_{\text{sc}}$. The 'initial' value $\eta_{\text{b}}(x_0) = \rho_{\text{b, in}} - \frac{1}{2}$ denotes the density deviation at the left boundary.

Far from the left boundary, i.e., for very large values of $\tilde{x} \sim x$, the expression (5.25) leads to the asymptotic behaviour

$$\eta_b(x) \approx \frac{a}{\sqrt{\tilde{x}}} \left[1 + b \frac{\ln(\sqrt{\tilde{x}})}{\sqrt{\tilde{x}}} \right] \approx \frac{D_{sc}}{2v_b \sqrt{x x_{sc}}}. \quad (5.26)$$

Thus, the deviation of the bound density from its asymptotic value now decays as $1/\sqrt{\tilde{x}} \sim 1/\sqrt{x}$ as for the ASEP in one dimension. In addition, we also obtain a correction term in Eq. (5.26) which depends on $b = 1 + g N_{ch} D_{ub} / D_{sc}$. For large tube radius R , one has $N_{ch} \sim R^2$ and $b \sim N_{ch} \sim R^2$. Therefore, the correction term becomes large for large R .

For the intermediate range of \tilde{x} -values defined by $a/\eta_b(x_0) \ll \tilde{x} \ll b^2$, the deviation η_b of the bound density from its asymptotic value as given by Eq. (5.25) simplifies and becomes

$$\eta_b \approx \frac{2ab}{\tilde{x}} = \frac{D_{sc} + g N_{ch} D_{ub}}{v_b x_{sc}} \frac{1}{\tilde{x}}. \quad (5.27)$$

Thus, for these intermediate \tilde{x} -values the density deviation decays again as $\sim 1/\tilde{x}$. We can now define a crossover length $\tilde{x} = \tilde{x}_*$ at which the latter two expressions are equal. This leads to

$$\tilde{x}_* = 4b^2 \sim R^4 \quad \text{for large } R. \quad (5.28)$$

Close to the left boundary, i.e., for small values of $\tilde{x} \sim x - x_0$, the expression (5.25) for the deviation of the bound density from its asymptotic value $\rho_b^0 = 1/2$ leads to

$$\eta_b(x) \approx \eta_b(x_0) \left[1 - \frac{1}{2ab} \eta_b(x_0) \tilde{x} \right]. \quad (5.29)$$

We may now define a second crossover length or extrapolation length $\tilde{x} = \tilde{x}_{**}$ at which the two terms in (5.29) cancel. This extrapolation length is given by

$$\tilde{x}_{**} = 2ab/\eta_b(x_0) = 2ab/(\rho_{b,in} - \frac{1}{2}). \quad (5.30)$$

For large tube radius R , the latter length scale grows as $\tilde{x}_{**} \sim b \sim R^2$. In general, the extrapolation length can have both signs but, for the maximal current phase, one always has $\rho_{b,in} > 1/2$ and, thus, $\tilde{x}_{**} > 0$. Note that the same expression is obtained by defining \tilde{x}_{**} as the length at which the intermediate expression (5.27) is equal to the left boundary value $\eta_b(x_0)$.

In summary, the theory described here indicates (i) that the 'initial' value at the left boundary is felt up to an extrapolation length $\tilde{x}_{**} \sim b \sim R^2$, (ii) that the true asymptotic behaviour of the density deviation is obtained for $\tilde{x} > \tilde{x}_* \sim R^4$ as follows from (5.28), and (iii) that the density deviation decays as $1/\tilde{x}$ on intermediate length scales with $\tilde{x}_{**} \ll \tilde{x} \ll \tilde{x}_*$.

These conclusions agree with the results of Monte Carlo simulations. In these simulations, the tube length L is necessarily finite. This implies that the profiles observed in the simulations may not reach the asymptotic behaviour present in a tube of infinite length. Since both the crossover length \tilde{x}_* and the extrapolation length \tilde{x}_{**} increase quickly with increasing tube radius R , we expect to find the true asymptotic behaviour only for sufficiently small values of R . This expectation is confirmed by the simulation results. For sufficiently small R , the density deviation η_b is found to decay as $\sim 1/x^{1/2}$ for large x , as shown in Fig. 5.5(a) for $R = 3$. For sufficiently large values of R , on the other hand, the observed profiles decay as

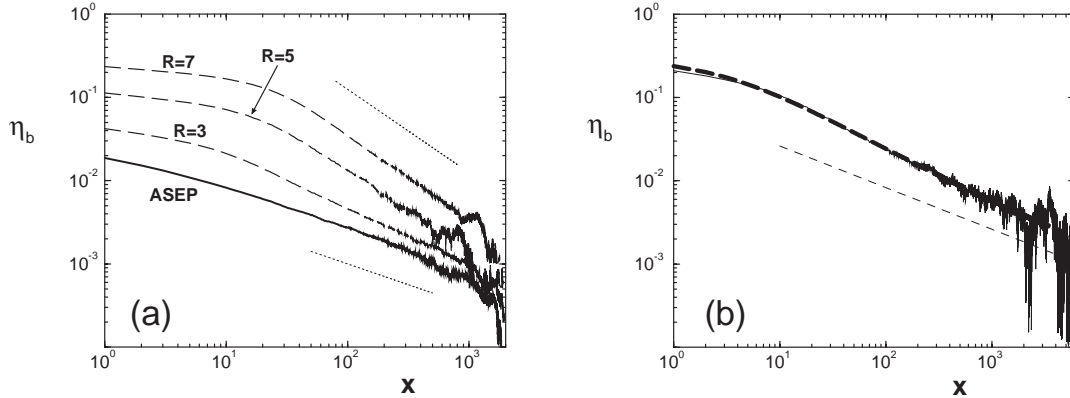


Figure 5.5: Deviation η_b of the bound density from its constant value far from the boundaries as a function of the spatial coordinate x for (a) the one-dimensional ASEP (solid line) and for motor traffic in tubes with radius $R = 3, 5, 7$ (dashed lines), length $L = 2000$; and (b) for a tube with radius $R = 3$ and length $L = 6000$ (thin solid line); boundary conditions (B) with $\rho_{b,\text{in}} = 0.8$ and $\rho_{b,\text{ex}} = 0.5$ and random walk probabilities as in Fig. 5.3. The curves for the one-dimensional ASEP and for the tube radii $R = 3, 5$ in (a) have been multiplied by scale factors 0.1, 0.2, and 0.5, respectively. The thin dotted lines correspond to the decay laws $\sim 1/x$ and $\sim 1/\sqrt{x}$, respectively. The thick dashed line in (b) is a fit to Eq. (5.25) with $D_{sc} \simeq 0.81$ and $x_{sc} \simeq 8.57$. The thin dashed line indicates the power law $\sim 1/\sqrt{x}$. Note that the simulation data decay faster than $\sim 1/\sqrt{x}$ for $10^1 \lesssim x \lesssim 10^2$.

$1/x$, see the Monte Carlo data in Fig. 5.5(a) for $R = 5$ and $R = 7$. In the latter cases, the true asymptotic behaviour is not accessible and is cut off by the finite value of L .

In addition, a more detailed analysis of the Monte Carlo results for small values of R but large values of L explicitly shows that the decay of the bound density deviation behaves as $\sim 1/\sqrt{x}$ for large x but decays faster than $1/\sqrt{x}$ for smaller values of x . This crossover behaviour is shown in Fig. 5.5(b) where the simulation data are compared with the thin dashed line corresponding to the decay law $\sim 1/\sqrt{x}$. Furthermore, the data can be well fitted with a density profile as given by Eq. (5.25) if one makes an appropriate choice for the scale parameters D_{sc} and x_{sc} .

The Monte Carlo data shown in Fig. 5.5(b) correspond to a tube of radius $R = 3$ and length $L = 6000$ with boundary densities $\rho_{b,\text{in}} = 0.8$ and $\rho_{b,\text{ex}} = 0.5$. In this case, a least-squares fit of the data for $x > 20$ leads to the parameter values $D_{sc} \simeq 0.81$ and $x_{sc} \simeq 8.57$. The corresponding fitting curve corresponds to the thick dashed line in Fig. 5.5(b). The fit becomes less reliable close to the left boundary, where the assumption that η_b is small is no longer fulfilled. For fixed boundary densities, both fitting parameters D_{sc} and x_{sc} are found to depend on R and to increase with increasing R . In addition, for $R \geq 4$, it becomes rather difficult to determine these parameters since one would have to simulate rather long systems with $L \gg 6000$ in order to observe the true asymptotic behaviour.

5.4 Diffusive injection and extraction of motors

Finally, we consider the second type of open boundary conditions corresponding to case (C) in Fig. 5.1. The length of the tube is again denoted by L . This tube is now longer than the filament which has length $L_F < L$. The left end of the tube is located at $x = 0$ as before but the left end of the filament is at $x = \Delta L \equiv (L - L_F)/2$. Likewise, the right end of the filament is at $x = \Delta L + L_F$ whereas the right end of the tube is at $x = L = 2\Delta L + L_F$. Thus, a motor particle which enters the tube on the left must diffuse over a distance $\sim \Delta L$ before it can come into contact with the filament, and a motor particle which leaves the filament at its right end must also diffuse over a distance $\sim \Delta L$ before it can leave the tube.

At the left and right end of the tube, we now prescribe constant boundary densities as given by

$$\rho(x = 0, y_1, y_2) = \rho_{\text{ub,in}} \quad \text{and} \quad \rho(x = L + 1, y_1, y_2) = \rho_{\text{ub,ex}} \quad (5.31)$$

for all values of y_1 and y_2 with $y_1^2 + y_2^2 \leq R^2$.

As before, the jump probability β to make backward steps on the filament is taken to be zero. Likewise, the resting probability γ to make no step at all on the filament is also zero with a possible exception at the 'last' filament site with $(x, y_1, y_2) = (\Delta L + L_F, 0, 0)$. Indeed, in order to define the system in a unique way, we still have to specify the probability to make a forward step at this 'last' filament site. Two possible choices appear rather natural: (i) *Active* unbinding from the 'last' filament site, i.e., the motor particle attempts to step forward with probability α and makes a step if the adjacent non-filament site is unoccupied. In this case, the forward step at the last filament site is governed by the same probabilities as all other forward steps along the filament; and (ii) *Thermal* unbinding in which the motor particle unbinds with probability $\epsilon/6$ both in the forward direction and in the four orthogonal directions. In the latter case, one has to choose the resting probability γ to be nonzero and to be given by $\gamma = 1 - 5\epsilon/6$.

The choice (i) is suggested by the results of recent experiments on microtubules and kinesin motors [62] which indicate that these motors unbind quickly at the filament ends. In the following subsections, we will first consider this choice (i) corresponding to active unbinding from the last filament site. In the last section 5.4.3, we will show that the choice (ii) leads to rather similar behaviour.

5.4.1 Diffusive bottlenecks

In order to understand the behaviour found for boundary condition (C), it is instructive to partition the tube into three compartments which are defined as follows: (i) A left compartment with $1 \leq x < \Delta L$ where transport is purely diffusive; (ii) a middle compartment with $\Delta L \leq x \leq \Delta L + L_F$ where all directed (or active) transport occurs; and (iii) a right compartment with $\Delta L + L_F < x \leq L$ where the transport is again purely diffusive.

For a stationary state, the total current through the tube must be constant and, thus, must be the same in all three compartments. The current through the middle compartment is given by the bound current $j_b = v_b \rho_b^0 (1 - \rho_b^0)$ if the filament is sufficiently long. Thus, the diffusive currents $J_{\text{dif,L}}$ and $J_{\text{dif,R}}$ in the left and right tube segment must be equal and must satisfy the simple relation

$$J_{\text{dif,L}} = J_{\text{dif,R}} = v_b \rho_b^0 (1 - \rho_b^0). \quad (5.32)$$

The relation as given by Eq. (5.32) is easily checked in the simulations since the density profile is found to be approximately linear in the left and in the right compartments provided

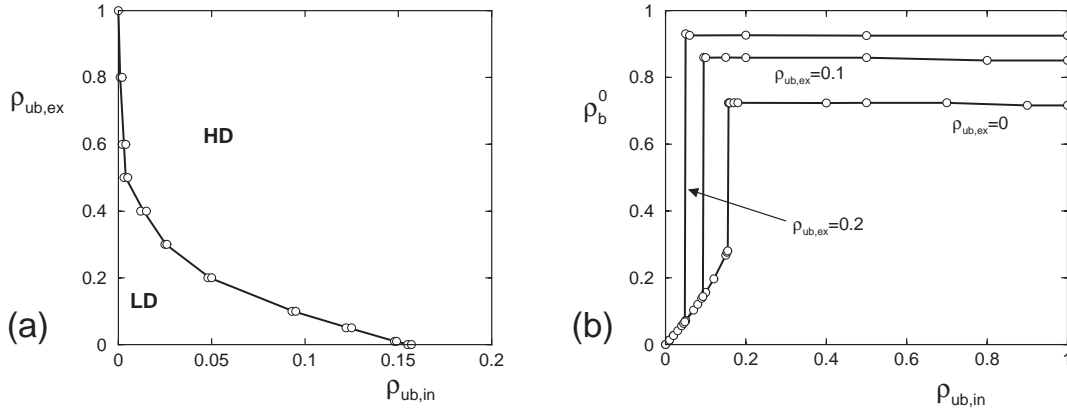


Figure 5.6: (a) Phase diagram as a function of the left and right boundary densities $\rho_{ub,in}$ and $\rho_{ub,ex}$ for tubes with boundary conditions (C) and a set of parameters where no maximal current phase occurs. The tube has length $L = 600$ and radius $R = 5$, the filament length is $L_F = 590$ and the distance between the filament ends and the tube ends is $\Delta L = 5$. The random walk probabilities are the same as in Fig. 5.3. Note the different scales of the axes. (b) Bound density ρ_b^0 as a function of the left boundary density $\rho_{ub,in}$ for the same system. The discontinuity in the functional dependence of ρ_b^0 on $\rho_{ub,in}$ corresponds to the transition from the low to the high density phase.

ΔL is sufficiently large. For such a linear density profile in the right compartment, the diffusive current $J_{dif,R}$ can be estimated as

$$J_{dif,R} \simeq (1 + N_{ch})D_{ub} \frac{|\rho_{ub}(x = \Delta L + L_F) - \rho_{ub,ex}|}{\Delta L}. \quad (5.33)$$

Since the maximal density difference is one (in the units used here), the maximal diffusive current behaves as

$$\max(J_{dif,R}) \sim (1 + N_{ch})D_{ub} \frac{1}{\Delta L} \sim R^2 D_{ub} \frac{1}{\Delta L}. \quad (5.34)$$

This shows that the maximal diffusive current depends on the tube radius R , the lateral size ΔL of the diffusive segments, and the diffusion coefficient D_{ub} of the unbound motors. Since these parameters can be chosen independently from the bound motor velocity v_b , the diffusive current $J_{dif,L}$ can be made smaller than the maximal bound current $v_b/4$ on the filament. In the latter case, the diffusive compartments act as diffusive bottlenecks and the maximal current phase characterized by the current $v_b/4$ is expected to be absent from the phase diagram. This expectation is indeed confirmed by the simulations as discussed next.

5.4.2 Phase diagrams with and without maximal current phase

Phase diagram without maximal current phase

One geometry for which no maximal current phase has been observed in the simulations is provided by a tube with radius $R = 5$, length $L = 600$, and filament length $L_F = 590$. The corresponding phase diagram as determined by the Monte Carlo simulations is shown in Fig. 5.6(a). The largest part of the phase diagram is covered by the high density phase (HD);

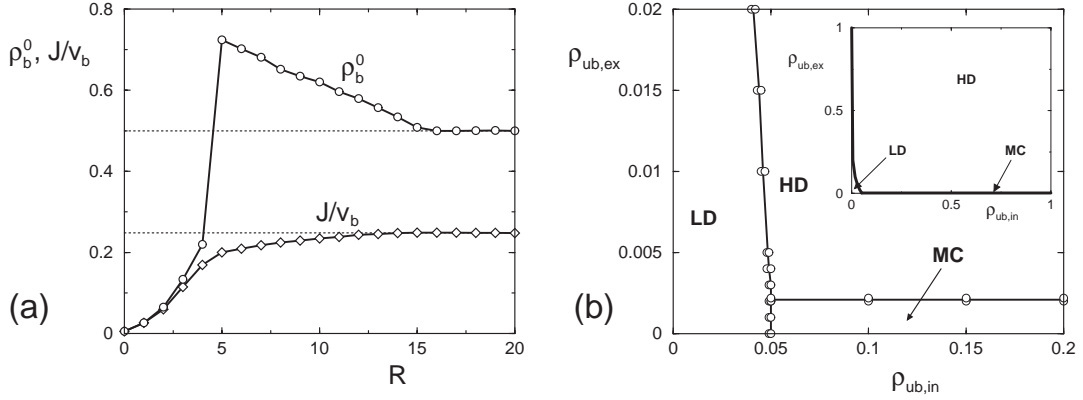


Figure 5.7: (a) Current J/v_b (diamonds) and bound density ρ_b^0 (circles) as a function of the tube radius R for boundary conditions (C) with $\rho_{ub,in} = 0.2$, $\rho_{ub,ex} = 0$. The tube length $L = 600$, the filament length $L_F = 590$, and the distance between the filament ends and the tube ends is $\Delta L = 5$. The random walk probabilities are the same as in Fig. 5.3. The maximal current $J/v_b = 1/4$ is obtained for $R \geq R_* \simeq 16$. (b) Phase diagram for a tube of radius $R = 17$ with boundary conditions (C) and parameters as in (a). In the inset, which shows the complete phase diagram, the maximal current phase can be hardly distinguished from the line $\rho_{ub,ex} = 0$.

in addition, a low density phase (LD) is found for small values of the boundary densities $\rho_{ub,in}$ and $\rho_{ub,ex}$.

The transition line displayed in Fig. 5.6(a) has been determined from the functional dependence of the bound density in the bulk, ρ_b^0 , on the left boundary density $\rho_{ub,in}$ as shown in Fig. 5.6(b). Inspection of this latter figure shows that the bound bulk density ρ_b^0 jumps at a certain value of the left boundary density $\rho_{ub,in}$. Since L is finite, this jump occurs over a small but finite interval of $\rho_{ub,in}$. Thus, the jump can be characterized by two values of $\rho_{ub,in}$, say $\rho_{ub,in}^<$ and $\rho_{ub,in}^>$, which represent the left and the right 'corner' of the numerically determined jump. Both $\rho_{ub,in}$ -values have been included in the phase diagram of Fig. 5.6(a). For $\rho_{ub,in}^< < \rho_{ub,in} < \rho_{ub,in}^>$, the simulations do not reach a stationary state within two days of computation. Simulations also become very slow in the high density phase especially when the overall motor concentration gets so large that the bound density is close to one and the unbound density is no longer small compared to the bound density.

Presence of the maximal current phase

In order to estimate the set of parameters, for which the phase diagram exhibits a maximal current phase, we return to the estimate (5.33) for the diffusive current $J_{dif,R}$ and make the simplifying assumption that the bound and unbound densities in the middle compartment of the tube are essentially constant. Thus, we replace the true unbound density $\rho_{ub}(x = \Delta L + L_F)$ at the right end of the filament by its bulk value ρ_{ub}^0 .

The bulk density ρ_{ub}^0 of the unbound motors is related to the bulk density ρ_b^0 of the bound motors via the radial equilibrium relation (5.1). For the maximal current phase, one has $\rho_b^0 = 1/2$ and Eq. (5.1) leads to $\rho_{ub}^0 = \frac{\epsilon/\pi_{ad}}{1+\epsilon/\pi_{ad}} \approx \epsilon/\pi_{ad}$ for small ϵ . In this way, we arrive at

the estimate

$$J_{\text{dif,R}} \simeq (1 + N_{\text{ch}}) D_{\text{ub}} \frac{\epsilon}{\pi_{\text{ad}} \Delta L} \quad \text{for} \quad \rho_{\text{ub,ex}} = 0. \quad (5.35)$$

The maximal current phase should be present in the phase diagram if the diffusive current $J_{\text{dif,R}}$ exceeds the maximal current $v_{\text{b}}/4$ on the filament. It then follows from (5.35) that, for $\rho_{\text{ub,ex}} = 0$, the maximal current phase should be present if the tube radius R satisfies

$$R^2 > R_*^2 \equiv \frac{v_{\text{b}} \pi_{\text{ad}} \Delta L}{4\pi D_{\text{ub}} \epsilon} \quad (5.36)$$

where $1 + N_{\text{ch}} \approx \pi R^2$ has been used. Using the same line of reasoning, a second, less restrictive condition can be obtained from an estimate for the diffusive current within the left compartment.

The threshold value R_* for the tube radius as given by Eq. (5.36) has been confirmed by Monte Carlo simulations for the jump probabilities $\alpha = 1 - 2\epsilon/3$ with $\epsilon = 1/100$, the sticking probability $\pi_{\text{ad}} = 1$, the compartment size $\Delta L = 5$, and the boundary densities $\rho_{\text{ub,in}} = 0.2$ and $\rho_{\text{ub,ex}} = 0$. The jump probabilities imply the bound motor velocity $v_{\text{b}} = 1 - 2/300$; the diffusion coefficient D_{ub} of the unbound motors has the value $D_{\text{ub}} = 1/6$. When these parameter values are inserted into Eq. (5.36), one obtains the estimate $R_* \simeq 15.4$.

The corresponding Monte Carlo data are displayed in Fig. 5.7(a). Inspection of this figure shows that the current does indeed attain its maximal value $v_{\text{b}}/4$ for $R \geq R_*$ with $R_* \simeq 16$. Fig. 5.7(a) also shows the transition from the low density to the high density phase which occurs for a tube radius R_{**} which satisfies $4 < R_{**} < 5$.

A complete phase diagram for a tube with radius $R = 17$ is shown in Fig. 5.7(b). Again, most of the phase diagram is covered by the high density phase (HD), while a low density phase (LD) is found only for very small values of $\rho_{\text{ub,in}}$. The maximal current phase (MC) is present now but only for very small values of $\rho_{\text{ub,ex}}$.

It is interesting to note that similar effects also occur in the purely one-dimensional system if one considers a driven system which is bounded by two segments which exhibit only diffusive transport. In this one-dimensional case, quantitative predictions can be made using a mean field approximation, see appendix D.3.

5.4.3 Active versus thermal unbinding from the 'last' filament site

The Monte Carlo data displayed so far have been obtained for active unbinding of a motor particle which is bound to the 'last' filament site. As mentioned above, another possibility is that the motor particle gets stuck at the 'last' filament site and unbinds only by thermal excitations, i.e., with unbinding probability $\epsilon/6$. For these two different unbinding mechanisms, one will, in general, obtain different density profiles. However, this difference is not dramatic as one can see from Fig. 5.8 which exhibits density profiles for both cases. Although the probability for a forward step at the 'last' filament site differs by two orders of magnitude for the two cases, the bulk density exhibits a relatively small difference. The bound density, on the other hand, increases and decreases close to the right end of the filament for thermal and active unbinding from the 'last' site, respectively.

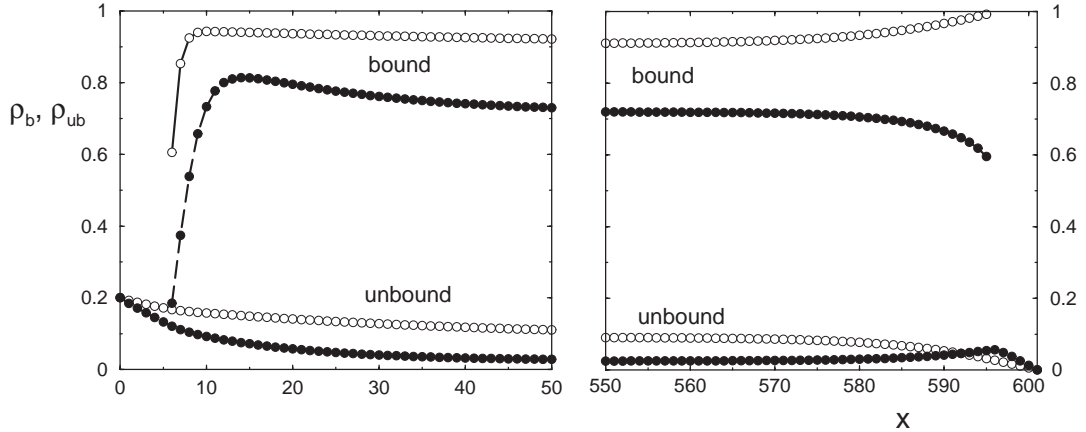


Figure 5.8: Bound and unbound density profiles ρ_b and ρ_{ub} as functions of the spatial coordinate x for boundary conditions (C) with $\rho_{ub,in} = 0.2$ and $\rho_{ub,ex} = 0$. Two different unbinding processes of the motor particles at the 'last' filament site are compared: Active unbinding for which the motor makes one final step in the forward direction (filled circles); and thermal unbinding with probability $\epsilon/6$ in the forward direction (open Circles). The geometric parameters are $L = 600$, $L_F = 590$, $\Delta L = 5$, and $R = 5$; the random walk probabilities are as in Fig. 5.3.

5.5 Summary

In this chapter, we have studied motor traffic through open tubes which contain a single filament. As for the ASEP in one dimension, the motor traffic in open tubes can exhibit three different phases depending on the motor concentrations in the reservoirs to which the tube ends are coupled: high density and low density phases which are characterized by an exponential decay of the density deviations from their bulk values and maximal current phases characterized by an algebraic decay.

In general, the location of the transition lines is found to depend on the precise choice of the boundary conditions. Apart from periodic boundary conditions, case (A), we have studied two different boundary conditions (B) and (C) for an open tube. In case (B), the bound and unbound densities are kept fixed at the boundaries and satisfy radial equilibrium. For this case, the location of the transition lines is independent of the model parameters, and the phase diagram of the one-dimensional ASEP is recovered. In case (C), the active compartment of the tube is bounded by two compartments where the transport is purely diffusive. In this latter case, the phase diagram depends on the geometry of the tube and on the transport properties in the bound and unbound motor states. In many cases, the maximal current phase is completely suppressed by the coupling to the diffusive compartments which act as bottlenecks for the transport.

As tube systems such as those described here are in principle accessible to experiments, the traffic of molecular motor through open tubes is a promising candidate for the experimental observation of boundary-induced phase transitions and might be used as a model system to study these transitions in a systematic way.

Chapter 6

Motors with attractive interactions

In this chapter, we will discuss motors with additional interactions. In the first part of the chapter, we summarize what is known from experiments about the interactions of motors and consider the case of an attractive motor–motor interaction such that binding to the filament is stimulated by motors already bound to it.

In the second part of the chapter, we consider the case of two species of motors moving into opposite directions. While binding to the filament is stimulated by the presence of motors of the same type, it is inhibited by the presence of motors of the other species. This kind of interaction exhibits (i) a state characterized by spontaneously broken symmetry, where one motor species is largely excluded from the filament, (ii) hysteresis of the total current upon varying the relative concentrations of the two motor species, and (iii) the formation of lanes of traffic into opposite directions.

Interactions of motors are still largely unexplored. However, our basic assumptions, which are based on experimental results, are simple and plausible. One may therefore expect that the new type of phase transition between different stationary states should be accessible to experiments with a model system based on biological motor molecules.

6.1 Interactions of motors

As mentioned before, until now only a few experiments have been performed to study interactions of molecular motors. In the following, we summarize the experimental results. Let us repeat that exclusion effects as discussed in the previous chapters are well established and have been observed both for inactive motors in decoration experiments [77] and for active motors in motility assays [78].

Most of the knowledge about other motor–motor interactions has been obtained in microtubule decoration experiments. These experiments are done in the absence of ATP, i.e., motors do not move along the microtubule, but only bind to it. Saturated binding of motors to microtubules is then studied by electron microscopy or X-ray diffraction. For binding of dimeric kinesin motors to microtubules, two observations suggest an attractive interaction between the motors: First, two-dimensional order with 16nm periodicity has been found, and second, there is coexistence of decorated and bare microtubules [107]. The latter observation has also been made for the decoration of actin filaments with muscle myosin [108,109], where the interaction between the motors depends on the internal conformation of the actin filaments [109].

This observation as well as more recent (still unpublished and possibly controversial) ex-

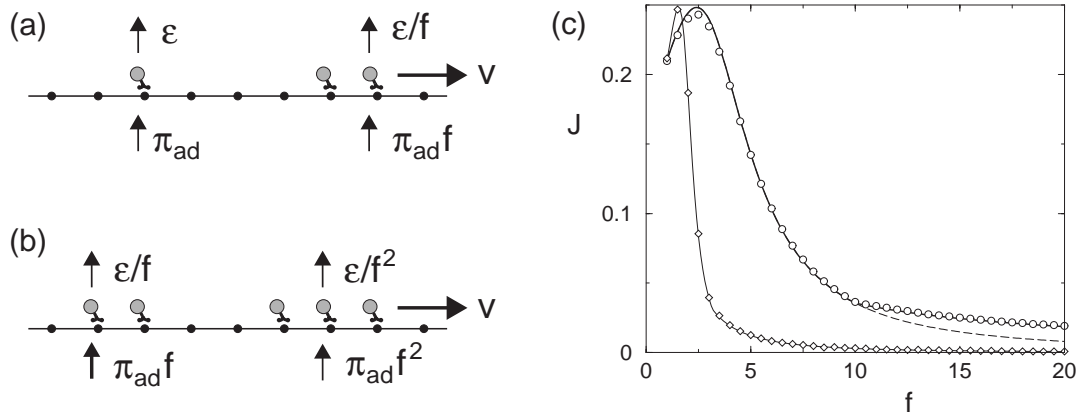


Figure 6.1: Detachment rates and sticking probabilities for the case where binding to the filament is stimulated and unbinding inhibited by the presence of a bound motor: (a) Asymmetric (forward) interaction and (b) symmetric interaction, see text. Note that the situations (a) also apply to the symmetric case. (c) Current J as a function of the interaction parameter f for the cases of asymmetric (thick solid line and circles) and symmetric interaction (thin solid line and diamonds). Symbols are simulation results in a system of length $L = 100$ and radius $R = 5$ (corresponding to $\phi = 88$), lines are from the mean field calculation. The dashed line indicates the mean field result in a case without time discretization, see text. The parameters are $N/L = 4$, $\epsilon = 0.01$, $\pi_{\text{ad}} = 0.1$ and $\beta = \gamma = 0$.

perimental results on kinesin in the presence of ATP [110] suggest that the interaction between motors is probably transmitted via a deformation or a conformational change of the filament upon binding of a motor. This deformation affects the adjacent binding sites and can enhance binding of motors to these sites. Alternatively, interaction could take place directly between motor heads or be mediated by the tail domains. All three possibilities have been argued to be consistent with the experimental findings of Ref. [107].

Similar mechanisms are expected to be at work in the presence of ATP, i.e., if the motors are active and walk along the filaments. However, the interactions of moving motors have not been systematically explored by experiments up to now.

6.2 Attractive interactions

As discussed in the previous section, experiments indicate that there is an attractive interaction between motors or cooperative binding of motors to filaments. As a first step towards a theory of this motor–motor attraction, we discuss the case of a tube-like compartment with, for simplicity, periodic boundary conditions. We consider again the situation of one filament located along the symmetry axis of the tube.

If the interaction is mediated by a deformation of the filament, it is reasonable to assume that mainly the detachment rate and the sticking probability are affected by the presence of a second motor. We assume that binding to a lattice site next to an already bound motor is stronger than binding in the absence of that motor. As both the filament structure and the motor movements possess a favoured direction, the motor–motor interaction might be asymmetric in the sense that the binding rate next to a bound motor might depend on whether

the motor attempts to bind in front of the bound motor or behind it. We will therefore consider two cases in the following: (i) an asymmetric interaction, where binding is stimulated and unbinding is inhibited at lattice sites in front of a bound motor only (seen in its direction of motion); (ii) a symmetric interaction, where bound motors at both (forward and backward) neighbour sites stimulate binding and exhibit unbinding. An interaction of type (i) is suggested by the experimental results mentioned above [110]. However, the qualitative behaviour is found to be the same for both cases.

For both cases (i) and (ii), only nearest neighbour interactions are taken into account. Stimulation of binding and inhibition of unbinding are modeled by multiplying the detachment rate and the sticking probability by factors $1/f$ and f , respectively, if another motor is bound to the neighbour site. The parameter f is related to the motor–motor interaction energy ΔE_{int} by $f \sim \exp(-\Delta E_{\text{int}}/k_{\text{B}}T)$. For an attractive interaction we have $\Delta E_{\text{int}} < 0$ and $f > 1$. In the absence of other motors, the detachment rate and the sticking probability are again given by ϵ and π_{ad} , respectively. In the case (i) of asymmetric (forward) interaction, they are given by ϵ/f and $\pi_{\text{ad}}f$, respectively, at a filament site in front of a site occupied by a bound motor, see Fig. 6.1(a). In the case (ii) of a symmetric interaction, these rates are also used at filament sites behind a bound motor. In addition, in that case, binding to a filament site between two bound motors and unbinding from such a site occur with sticking probability $\pi_{\text{ad}}f^2$ and detachment rate ϵ/f^2 , respectively, see Fig. 6.1(b).¹

In addition, we assume that the rates for forward and backward steps are unaffected by the interaction, which is justified if the energy related to motor–motor interactions is small compared to the energy release from ATP hydrolysis, which is of the order of $20kT$.

In order for the interaction to be attractive, the interaction parameter f must be larger than one. For $f = 1$ we obtain the case discussed in the previous chapters, where motors interact only through hard core exclusion. If we now increase f (keeping the number N of motors in the tube fixed), motors are more strongly attracted by the filament, as there are already motors bound to the filament. Therefore the bound density increases. If it increases beyond the value $1/2$, this implies that the current through the tube decreases, as the filament gets crowded because of the attraction, see Fig. 6.1(c).

We use again a mean field approach to determine the bound density. In the case of an asymmetric interaction, the bound and unbound densities are related by

$$\epsilon\rho_{\text{b}} \left[(1 - \rho_{\text{b}}) + \frac{1}{f}\rho_{\text{b}} \right] = \pi_{\text{ad}}\rho_{\text{ub}}(1 - \rho_{\text{b}}) \left[(1 - \rho_{\text{b}}) + f\rho_{\text{b}} \right]. \quad (6.1)$$

Together with the normalization, which fixes the number N of motors in the tube, this equation yields the bound density and thus the stationary current. The current obtained from this mean field calculation agrees well with the simulation data, see Fig. 6.1, but slight deviations can be seen close to the maximum of the curve.

Finally let us briefly consider the case (ii), i.e. symmetric interactions, where both backward and forward neighbours affect the detachment rate and the sticking probability as shown in Fig. 6.1(a) and (b). As motors can now interact with two neighbours, the attraction is stronger in this case and thus the maximum of the current is shifted to a smaller value of f compared to

¹A slight complication arises because of the time discretization in the simulations, which forces us to modify the expression for the sticking probability at a lattice site adjacent to a bound motor in our simulations: As the sticking probability cannot be larger than one per discrete time step, we use $\pi_{\text{ad}} \times \min\{f, 1/\pi_{\text{ad}}\}$ rather than $\pi_{\text{ad}}f$, compare the solid and dashed lines in Fig. 6.1. As the detachment rate is very small, the corresponding constraint for ϵ only matters for very large f .

case (i) and the current decreases more rapidly, when f is further increased. Both simulation data and mean field results for this case are included in Fig. 6.1(c).

6.3 Two species of motors

Let us now consider the case, where two species of motors move on the same filament, but into opposite directions. If motors of the same type interact via a deformation of the filament, one can expect that an attractive interaction between motors of the same directionality is accompanied by a repulsive interaction of motors of opposite directionality. We will assume such an interaction in the following and discuss effects related to competitive binding of motors of opposite directionality. Let us mention that competition for binding sites has been observed in the case of conventional kinesin and ncd, a kinesin-related motor with opposite directionality [111].

We extend the models used above in the following way: The detachment rate is now multiplied by a factor f if a nearest neighbour site of the motor is occupied by a motor of the other species, see Fig. 6.2. If the site is occupied by a motor of the same species, it is multiplied by $1/f$ as before. The sticking probability is multiplied by f or $1/f$ next to a motor of the same or the other species, respectively. We studied again the two cases discussed above: (i) an asymmetric interaction, where binding and unbinding is only changed at lattice sites in front of a bound motor (seen in the direction of motion of that motor) and (ii) a symmetric interaction, where both forward and backward neighbours are considered. For both cases, the qualitative behaviour is found to be the same, therefore we will focus on case (i) in the following.

Systems with two species of active particles have previously been discussed in the context of driven lattice gases, where various phase transitions have been found such as a blocking transition from a spatially homogeneous state to a state characterized by a single macroscopic blockage in the case of two-dimensional and quasi one-dimensional (two-lane) systems with periodic boundary conditions (but not in one-dimensional systems) [112,113] and spontaneous symmetry breaking in open one-dimensional systems [114]. We therefore want to emphasize again that our system is different from these spatially homogeneous systems, as 'driving' or active motion of the motors is localized to the filament and motors can detach into the unbound state.

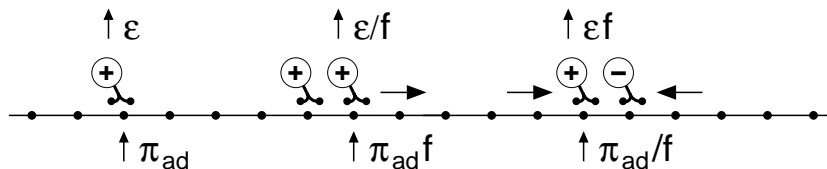


Figure 6.2: Two interacting species of motors, 'plus' and 'minus', with opposite direction of motion. Binding is stimulated and unbinding inhibited next to a bound motor of the same species. Next to a motor of the other species, binding is inhibited and unbinding enhanced, see text.

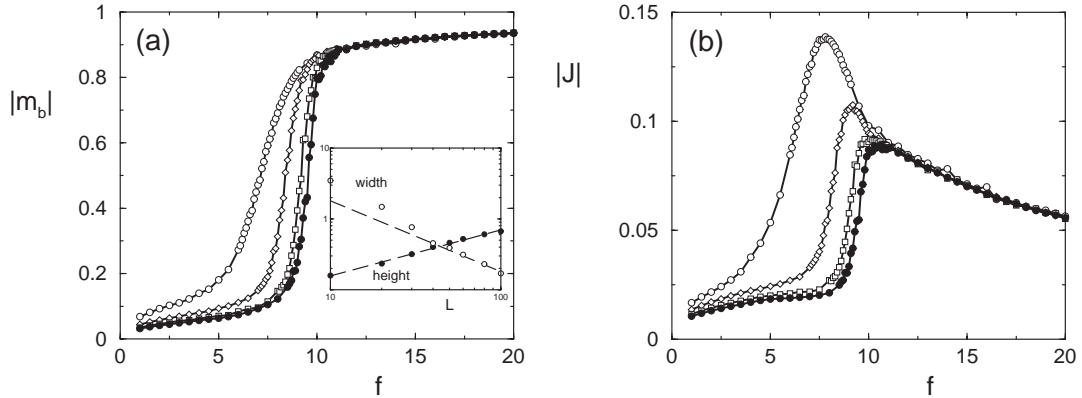


Figure 6.3: Absolute values of (a) the density difference $m_b = \rho_{b,+} - \rho_{b,-}$ and (b) the total current $J = J_+ + J_-$ as functions of the interaction parameter f for $N/L = 5$ and different systems sizes, $L = 40$ (\circ), $L = 100$ (\diamond), $L = 160$ (\square) and $L = 200$ (\bullet). Data points have been obtained by simulating 10^6 Monte Carlo steps per data point using the final configuration of one run as starting configuration for the following one with increased f . The other parameters are the same as in Fig. 6.1. The inset in (a) shows the finite-size scaling of the height (filled circles) and width (open circles) of the peak in $m'_b(f) = \partial|m_b|/\partial f$ as a function of the tube length L , see text; the dashed lines indicate the power laws $\sim L^{-1}$ and $\sim L^{0.65}$.

6.3.1 Two kinds of phase transitions

If the interaction is strong, i.e. for large f , motors bound to the filament strongly attract other motors of the same type to the filament, but repel those of the other type. If the concentration of one species of motors along the filament is much higher than the concentration of the other species, the second species is basically excluded from the binding sites of the filament. On the other hand, the motors of the majority species on the filament are unlikely to unbind, since they are attracted by their neighbours. If the numbers of motors of both species are different, the majority species on the filament can be expected to be the one with the larger overall population. If, however, the numbers are equal, spontaneous symmetry breaking might occur.

In the following, we will denote the two species by 'plus' and 'minus' according to their directions of motion. Their bound and unbound densities are $\rho_{b,\pm}$ and $\rho_{ub,\pm}$, respectively. The total numbers of 'plus' and 'minus' motors are N_+ and N_- , respectively. In addition, we define the total number of motors by $N \equiv N_+ + N_-$. In the following, we will consider the case $N_+ = N_- = N/2$. As order parameters, we choose the difference of the bound densities $m_b \equiv \rho_{b,+} - \rho_{b,-}$ and the total current, which is the sum of the currents of each species, $J = J_+ + J_-$. The density difference is zero in the symmetric state and non-zero for broken symmetry. Note that the difference of unbound motor densities, m_{ub} , would be an equivalent choice, as the numbers of motors in the tube are conserved. In states of broken symmetry, both m_b and m_{ub} are non-zero, but have opposite signs. The current J vanishes in the symmetric state, because the currents of the two species have the same absolute value, but different signs and cancel each other. On the other hand, if the symmetry is broken, the current is non-zero and flows into the direction of motion of the majority species on the filament.

We have performed Monte Carlo simulations to study the behaviour of systems with two species of motors and the simulations confirm the expectations discussed above: For weak

interaction, motors of both species are bound to the filament and the concentrations of bound motors are equal for both types. The total current vanishes as the currents of motors of opposite directionality balance each other. For large f , on the other hand, we observe spontaneous symmetry breaking. Motors of one species are bound to the filament, while those of the other species are largely excluded from it. Correspondingly the total current is different from zero. As the simulated system is relatively small, there are strong finite-size effects. We sometimes observe reversal of the direction of the current, as the system flips from one of the two equivalent states to the other. In addition, in an interval of intermediate values of f , where the transitions from the symmetric state to the state of broken symmetry occurs, the values of the total current J and of the difference of bound densities, m_b fluctuate strongly, indicating that this transition might correspond to a critical point.

To get rid of these fluctuations, we consider $|J| = \langle |J_+ + J_-| \rangle$ instead of J and $|m_b| = \langle |\rho_{b,+} - \rho_{b,-}| \rangle$ instead of m_b . Here $\langle \cdot \rangle$ indicates a time average, while J_+ , J_- , $\rho_{b,+}$ and $\rho_{b,-}$ are determined by averaging over all motors at one time step. In the limit of large system size, these quantities yield the original order parameters, J and m_b . As they are indifferent against flipping from one majority species to the other, these quantities do not exhibit the large fluctuations observed in the data for J and m_b , but in the symmetric state of the systems, we now measure the fluctuations and therefore obtain non-zero values for the total current, in particular for small systems [115].

Both quantities are shown in Fig. 6.3 as functions of f for different system sizes L and a relatively high total number of motors, $N/L = 10$. For small f , they yield non-zero values, but these values get smaller with increasing tube length L . A sharp increase of both quantities occurs at the critical value f_c of the interaction strength. f_c is shifted to larger values with increasing tube length L . For the largest system sizes used here, we find $f_c \simeq 9.6$ for the chosen parameters. Note that the current decreases for large f , which corresponds to the decrease in current discussed in the previous section for a single motor species.

Continuous transition upon varying the interaction strength

Let us consider again Fig. 6.3. As the curves for the order parameter $|m_b(f)|$ exhibit strong finite-size effects, it is hard to judge whether the transition is continuous or discontinuous. However, as mentioned before, the observation of strong fluctuations close to the transition suggests that the transition corresponds to a critical point and is continuous. In the following, we will give two arguments which support this idea: (i) We will show below that a mean field calculation predicts a continuous transition, and (ii) in this section, we analyze the finite-size scaling of the derivative of the order parameter.

To test the idea that the transition is continuous, we performed simulations for different system sizes L and determined the derivative of the order parameter, $m'_b \equiv \frac{\partial}{\partial f} |m_b|$, which exhibits a peak. If the transition is discontinuous, the height of this peak can be expected to grow linearly with the system size L (at least for large L), as there is no other large length scale such as the diverging correlation length in the case of a second-order transition [115]. At the same time, the width of the peak should decrease as $\sim L^{-1}$, so that a delta function is obtained in the limit of infinite L . We determined both quantities by fitting a Gaussian to the simulation data for m'_b and find that the height increases as $L^{0.65}$ and the width decreases as L^{-1} , see the inset in Fig. 6.3(a), indicating that the density difference is continuous at the transition. The result is, on the other hand, consistent with a divergence of m'_b in the large L limit. Let us assume that close to the transition point $f = f_c$, m'_b is given by $m'_b \sim (f - f_c)^{-\eta}$

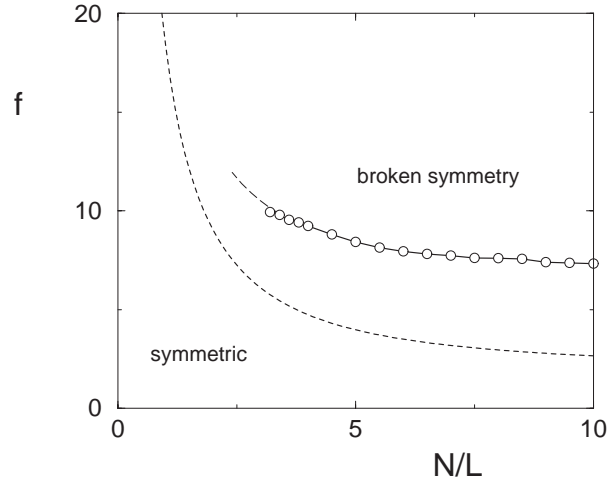


Figure 6.4: Phase diagram. The critical interaction strength f_c as a function of the total number N of motors as obtained from Monte Carlo simulations (circles) and mean field calculation (dashed line). Simulations have been performed for a system of length $L = 100$. For $N/L \lesssim 3.2$, values for f_c could not be determined because of the limited resolution of the simulations, see text. The parameters are as in Fig. 6.1.

and that the maximum of m'_b in the case of a finite systems size L occurs at $f = f_{\max}$ with $(f_{\max} - f_c) \sim L^{-\delta}$, hence the height of the peak scales like $(f_{\max} - f_c)^{-\eta} \sim L^{\eta\delta}$. The width of the peak, on the other hand, scales also like $(f_{\max} - f_c) \sim L^{-\delta}$ and, thus, the area, the product of width and height is given by $L^{\delta(\eta-1)}$. If m_b is finite and m'_b has a peak at the transition, η is restricted to $0 \leq \eta < 1$ and thus the integral or the area approaches zero for large L , as observed in our data.

Phase diagram

Varying the total number of motors in the tube, $N = N_+ + N_-$, we can determine the critical value of the interaction parameter, f_c as a function of N , shown in Fig. 6.4. As an estimate for f_c , we plotted the value of f for which m'_b attains its maximum. This value is obtained by fitting a Gaussian to the simulation data for m'_b as before. The data shown in Fig. 6.4 have been obtained for a tube of length $L = 100$. For larger systems the critical interaction parameter f_c can be expected to be shifted towards a slightly larger value, compare Fig. 6.3. The figure also shows the corresponding result from a mean field calculation, which will be discussed below.

For small N ($N/L \lesssim 3.2$ for the chosen parameters), however, fitting a Gaussian to m'_b becomes poor and no clear-cut maximum can be identified. In this case, the value of $|m_b|$ in the state of broken symmetry is comparable to the value in the symmetric state, which results from measuring fluctuations about zero. Thus one would need simulations for larger systems to determine f_c for small N/L . The corresponding mean field result indicates a strong increase in $f_c(N/L)$ for small N/L ; however, the quantitative predictions of the mean field calculation are not very good.

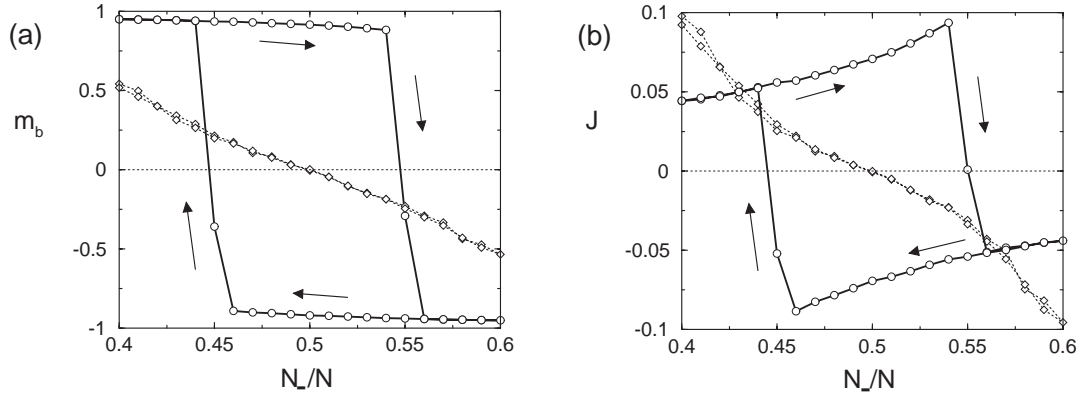


Figure 6.5: Hysteresis of (a) the density difference $m_b = \rho_{b,+} - \rho_{b,-}$ and (b) the total current $J = J_+ + J_-$ for $f = 15$ (\circ) varying the fraction of 'minus' motors, N_-/N . The total number of motors, $N = N_+ + N_-$, is kept fixed, $N/L = 5$ with $L = 100$. For $f = 6 < f_c$ (\diamond), no hysteresis is observed. The other parameters are as in Fig. 6.1. Data points have been obtained by simulating 10^6 Monte Carlo steps per value of N_-/N and using the final configuration of a run as starting configuration for the following one, scanning N_-/N from 0.4 to 0.6 and back.

Discontinuous transition upon varying the difference of motor numbers

A discontinuous transition with hysteresis is found upon varying the difference of the total numbers of motor particles of each type, $N_+ - N_-$, see Fig. 6.5. While doing this, we keep the total number of motors, $N = N_+ + N_-$, constant. Interestingly, the total current, $J = J_+ + J_-$, increases as the number of minority motors is increased, because these are excluded from the filament and so the density of bound motors decreases. The current thus adopts its maximal value in the metastable region.

Let us mention that, provided that such transitions occur in systems of biological motors, this is the type of experiment that could in principle be done easily. Probably, one would, however, simply add molecules of one type, increasing the total number of motors.

We can summarize these two phase transitions by noting the analogy with magnetic Ising-like phase transitions: For small interaction strength (corresponding to high temperature in the magnetic case), a symmetric state is found, while for strong interaction (low temperature), the symmetry is spontaneously broken. The transition from the symmetric to the asymmetric state is continuous and occurs at a critical point. A difference of the numbers of motors of each species acts as an external (magnetic) field. If this field is non-zero, it selects one of the two states of broken symmetry, which are equivalent at zero field. Varying this field, a first-order transition, accompanied by hysteresis, is obtained when the sign of the external field changes.

Finally, we want to mention that both transitions are also observed in the case of a symmetric interaction, where forward and backward neighbour sites have the same effect on the detachment rate and the sticking probability. As the interaction is stronger in this case, the critical value of f is smaller than for the asymmetric interaction.

6.3.2 Mean field theory

The phase transitions discussed in the previous section can be further studied using again continuum mean field equations. The equations of motion for bound and unbound densities of the two motor species, $\rho_{b,\pm}$ and $\rho_{ub,\pm}$ are:

$$\frac{\partial}{\partial t}\rho_{b,\pm} = \mp v_b \frac{\partial}{\partial x}\rho_{b,\pm}(1 - \rho_b) + D_b \frac{\partial^2}{\partial x^2}\rho_{b,\pm} + D_b \rho_{b,\pm} \frac{\partial^2}{\partial x^2}\rho_{b,\mp} - D_b \rho_{b,\mp} \frac{\partial^2}{\partial x^2}\rho_{b,\pm} + g_{\pm}(f) \quad (6.2)$$

$$\phi \frac{\partial}{\partial t}\rho_{ub,\pm} = D_{ub} \phi \frac{\partial^2}{\partial x^2}\rho_{ub,\pm} - g_{\pm}(f), \quad (6.3)$$

where $\rho_b \equiv \rho_{b,+} + \rho_{b,-}$. Note that, in contrast to the case of a single species, bound diffusion is affected by hard core exclusion [68], resulting in two additional terms proportional to D_b . The attachment/detachment terms g_{\pm} , which contain the interaction, are defined by

$$g_{\pm}(f) \equiv -\epsilon \rho_{b,\pm} \left[(1 - \rho_b) + f \rho_{b,\mp} + \frac{1}{f} \rho_{b,\pm} \right] + \pi_{ad} \rho_{ub,\pm} (1 - \rho_b) \left[(1 - \rho_b) + \frac{1}{f} \rho_{b,\mp} + f \rho_{b,\pm} \right]. \quad (6.4)$$

In this expression, we have used the simplest possible way to include the interactions in a mean field approximation. The detachment rate and the sticking probability are given by sums of three contributions, which are proportional to the local densities of empty sites, 'plus' motors and 'minus' motors, respectively. The relative weights of these contributions are given by factors f and $1/f$, such that adsorption is enhanced by the interaction between motors of the same species and inhibited by the interaction between motors of different species.

We rewrite these equations using the bound and unbound total motor densities, $\rho_b \equiv \rho_{b,+} + \rho_{b,-}$ and $\rho_{ub} \equiv \rho_{ub,+} + \rho_{ub,-}$, and the corresponding density difference between the species, $m_b \equiv \rho_{b,+} - \rho_{b,-}$ and $m_{ub} \equiv \rho_{ub,+} - \rho_{ub,-}$, as our new variables. With these definitions, we obtain

$$\frac{\partial}{\partial t}\rho_b = -v_b \frac{\partial}{\partial x}m_b(1 - \rho_b) + D_b \frac{\partial^2 \rho_b}{\partial x^2} + g_+(f) + g_-(f) \quad (6.5)$$

$$\begin{aligned} \frac{\partial}{\partial t}m_b &= -v_b \frac{\partial}{\partial x}\rho_b(1 - \rho_b) + D_b \frac{\partial^2 m_b}{\partial x^2} - D_b \rho_b \frac{\partial^2 m_b}{\partial x^2} + D_b m_b \frac{\partial^2 \rho_b}{\partial x^2} \\ &\quad + g_+(f) - g_-(f) \end{aligned} \quad (6.6)$$

$$\phi \frac{\partial}{\partial t}\rho_{ub} = D_{ub} \phi \frac{\partial^2 \rho_{ub}}{\partial x^2} - g_+(f) - g_-(f) \quad (6.7)$$

$$\phi \frac{\partial}{\partial t}m_{ub} = D_{ub} \phi \frac{\partial^2 m_{ub}}{\partial x^2} - g_+(f) + g_-(f). \quad (6.8)$$

With periodic boundary conditions, the stationary solutions are homogeneous and do not depend on the spatial coordinate x . They are given by the conditions

$$g_+(f) = g_-(f) = 0. \quad (6.9)$$

The bound and unbound densities are related by the normalization conditions,

$$\rho_b + \phi \rho_{ub} = \frac{N_+ + N_-}{L} \quad \text{and} \quad m_b + \phi m_{ub} = \frac{N_+ - N_-}{L}, \quad (6.10)$$

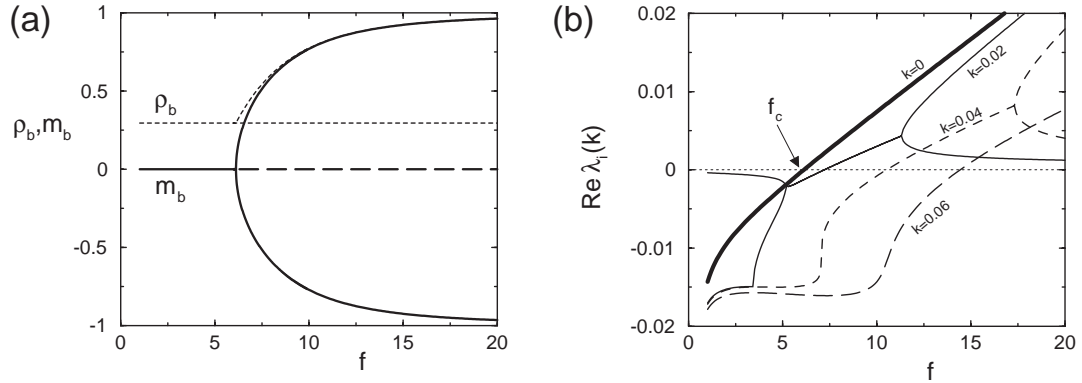


Figure 6.6: (a) Stationary solutions for the total bound density ρ_b and the density difference m_b as functions of the interaction parameter f for $N_+/L = N_-/L = 2$. Solid lines indicate the stable solutions for m_b , dashed lines unstable solutions. Thin dotted lines are the corresponding values for ρ_b . (b) Real parts of the eigenvalues $\lambda_i(k)$ of the operator \mathcal{L} governing the linearized dynamics, Eq. (6.11), as functions of the interaction strength f for homogeneous perturbations ($k = 0$) and spatially varying perturbations with wave vector k , see text. The parameters are as in Fig. 6.3.

where N_+ and N_- are the numbers of motors of the two species. With the normalization conditions, we can eliminate the unbound densities ρ_{ub} and m_{ub} from Eq. (6.9). The bound densities ρ_b and m_b are then determined by the conditions (6.9), which yield two polynomial equations of the third order in the bound densities.

Let us now consider the case $N_+ = N_-$. An obvious solution is the symmetric state, $\rho_{b,+} = \rho_{b,-} = \rho_b/2$ and $m_b = m_{ub} = 0$. Remarkably, this solution is independent of the interaction strength f , as the interaction terms drop out in the balance of attachment and detachment. The total motor density ρ_b is equal to the density of a single motor species interacting only through hard core exclusion as discussed in chapter 5.2.

The numerical solution of Eqs. (6.9)–(6.10) shows, however, that there are two additional solutions for sufficiently large interaction parameters $f > f_c$. These solutions have $m_b \neq 0$ corresponding to states, where the filament is populated mainly by one species. The solutions are plotted as a function of f in Fig. 6.6(a). In the vicinity of f_c , these solutions behave as $m_b \sim \pm(f - f_c)^{1/2}$. The latter result further supports the idea that the transition from the symmetric state to a state of broken symmetry observed in our simulations is a continuous transition.

To examine the stability of these solutions, we perform linear stability analysis, see, e.g., Ref. [116]. Linearizing Eqs. (6.5)–(6.8) about one of their solutions, we obtain

$$\frac{\partial}{\partial t} \eta = \mathcal{L} \eta, \quad (6.11)$$

where η is a vector containing the small perturbations of the four density variables. To examine the stability of the solutions, we have to determine the eigenvalues of the linear operator \mathcal{L} . First, we perform a Fourier transform to decouple the different spatial modes. Then we have to distinguish homogeneous perturbations and spatially varying perturbations of the stationary densities, i.e. Fourier modes with wave vectors $k = 0$ and $k \neq 0$, respectively. For the case

$k \neq 0$, the normalization condition (6.10) is automatically fulfilled and perturbations of the bound and unbound densities can be imposed independently. On the other hand, for $k = 0$ (where the total bound or unbound density or density difference is changed), a perturbation of ρ_b or m_b must be accompanied by one of the corresponding unbound variable and vice versa. This means that $\mathcal{L}(k)$ is a 4×4 matrix for $k \neq 0$, but a 2×2 matrix for $k = 0$. The eigenvalues of these matrices are determined numerically as functions of f , keeping the other parameters fixed, see Fig. 6.6(b).

Let us first consider homogeneous perturbations of the symmetric solution. In this case, both eigenvalues are real. They correspond to changing ρ_b or m_b without a change of the other variable. The first eigenvalue (which corresponds to a change of ρ_b) is negative for all values of f and thus the symmetric solution is stable against the first kind of perturbation. The second eigenvalue is negative for $f < f_c$ and positive for $f > f_c$, see Fig. 6.6(b). I.e., when increasing f beyond f_c , a pitchfork bifurcation occurs, where two new stable stationary solutions with broken symmetry appear, while at the same time the symmetric solution becomes unstable.

Next, we consider perturbations with $k \neq 0$. In this case, we observe for small k that two eigenvalues $\lambda_i(k)$ have the same real part (while their imaginary parts differ in sign) in a certain range of interaction parameters. At a certain value of the interaction strength, the real parts of these eigenvalues become larger than zero, see Fig. 6.6(b). This value approaches f_c if the absolute value of k is decreased. The other two eigenvalues, which are not shown in Fig. 6.6(b), are negative for the range of f studied.

Finally, the solutions with broken symmetry are stable against arbitrary perturbations in the whole range of f , where they exist. However, eigenvalues can become very small if one of the diffusion coefficients D_b or D_{ub} is small, indicating that diffusion is an important mechanism to suppress such perturbations.

We repeated the solution of Eqs. (6.5)–(6.10) for different values of the total number of motors per filament length, $N/L = (N_+ + N_-)/L$, to determine the critical value f_c of the interaction parameter as a function of N/L . The result has been included in Fig. 6.4. Increasing N/L , f_c is shifted to smaller values and at the same time, the branches with broken symmetry approach the maximal values of m_b , $m_b = \pm 1$, more quickly. On the other hand, for $N/L < 2$, the maximal value of $|m_b|$, approached for large f , is smaller than one, as the maximal density achievable with one species is $\min\{1, N/(2L)\}$. The mean field equations yield symmetry breaking for arbitrarily small values of N/L with $f_c(N/L) \sim (N/L)^{-1}$ for small N/L . For large numbers of motors, a constant value is approached exponentially. However, for very large N/L our analysis is no longer valid since we neglected exclusion effects of the unbound motors.

While the *qualitative* behaviour of the mean field solution agrees well with our simulations, a comparison of the phase diagrams from mean field theory and simulations shows that *quantitative* agreement is quite poor. On the one hand, this is due to the simplified interaction used in the mean field calculation. But in addition, there are discrepancies even for $f = 1$, where, apart from simple exclusion, interactions are absent. Our mean field approach predicts that the stationary density ρ_b is independent of the velocity v_b , while we observe ρ_b to decrease with increasing velocity in our simulations.² The reason for this discrepancy is that motors moving into opposite direction temporarily form local blockages, which locally act like a reflective wall. The density is homogeneous only on average over longer times. These blockages

²The correction to the equilibrium density is quadratic in the velocity, similar to the case of one species of motors in the closed tube of chapter 4.

are clearly a correlation effect and are not covered by the mean field description.

6.3.3 General remarks and extensions

We have mentioned before that the assumption of an asymmetric interaction can be dropped and that the phase behaviour remains qualitatively the same. The second assumption we have made, namely that the interaction affects only detachment and attachment (and not movement along the filament), however, is crucial for the observations discussed in the previous sections. If the rate of forward steps is also decreased by a factor $1/f$ in the case the target site is a neighbour to a motor of the other species, no symmetry breaking is observed in our simulations.

The difference between these two cases can be understood by considering the following simple situation. Imagine a 'plus' motor and a 'minus' motor separated by a single empty site. For the moment, we assume that no other motors of either species are around.

The rate for detachment of one motor in this situation can be estimated by $\epsilon_{\text{eff}} \simeq 2[\epsilon + 2\alpha(f)\epsilon(f)]$. The first term is spontaneous detachment, unaffected by the presence of the second motor, the second term describes enhanced detachment due to the interaction after a forward step by one of the motors. If the interaction affects only detachment and not the forward rate, one has $\epsilon(f) = f\epsilon$ and $\alpha(f) = \alpha = \text{const.}$, and thus $\epsilon_{\text{eff}} \simeq 2\epsilon(1 + 2f\alpha)$. By contrast, if the forward rate, which drives the motors into the unfavourable state, is reduced by a factor $1/f$, the two factors cancel each other, so that $\epsilon_{\text{eff}} \simeq 2\epsilon(1 + 2\alpha)$ and the effect of the interaction is shielded. Thus, the active step drives the motors into the unfavourable state, from where it is likely that one of them detaches, inducing the transitions discussed above. Let us mention that it is actually not necessary that the active motion is directed. In our simulations, we also observe symmetry breaking if forward and backward steps are equally likely, provided both are active in the sense that they are driven by a source of energy which overcomes the interaction.

Note that this dynamical effect is not covered by the mean field stability analysis, since the instability induced by homogeneous perturbations is completely independent of the dynamics.

Let us add a few remarks concerning extensions of the theory discussed so far. First, in the simulations the densities of bound motors are usually quite high in the states of broken symmetry. This is due to the fact that we have considered nearest neighbour interactions. Two of the experiments cited above indicate that filament-mediated interactions between motors might have a longer range [109, 110]. In that case, broken symmetry should be observed at smaller densities of bound motors.

Second, remember that in the closed tube systems studied in chapter 4, we have found the density profile to be approximately constant for large numbers of motors in the tube. In that case, the density profiles in the closed tube are thus very similar to those found for periodic boundary conditions (except for the regions close to the tube ends). From this similarity, we expect that symmetry breaking as shown above for the system with periodic boundary conditions can also be found in closed tube systems, at least for large overall motor concentrations.

Finally, imagine a tube system in the state of broken symmetry. Let us assume that the 'plus' motors move along the filament. If now a second filament is introduced into the tube, the unbound motors of the species 'minus' will be in excess of the 'plus' motors and the second filament will become populated by motors of the 'minus' type. In this way, the filaments form lanes of traffic of opposite directionality. We have confirmed this expectation by Monte Carlo simulations for a tube system with two parallel filaments as shown in Fig. 6.7. For $f < f_c$ the currents are the same for both filaments and the current of 'plus' motors has the same absolute

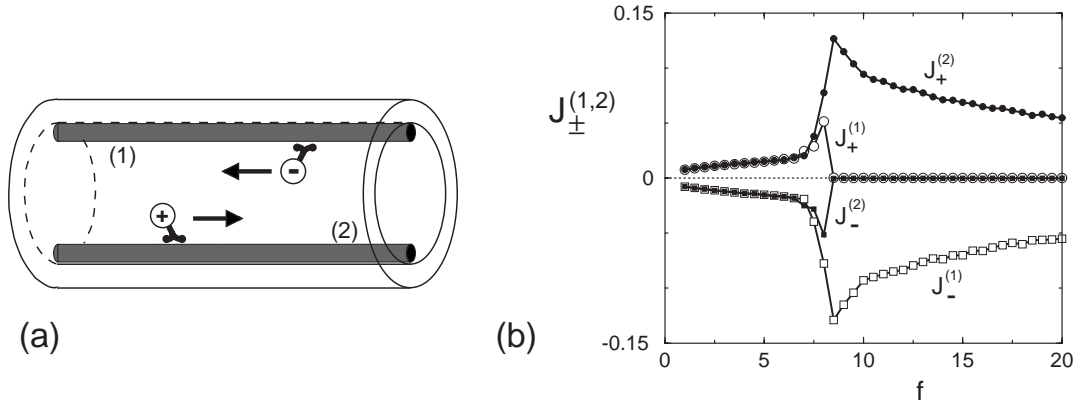


Figure 6.7: Spontaneous formation of lanes for traffic into opposite direction: (a) Two filaments within a tube located at the tube walls. 'Plus' motors move along filament (1) and 'minus' motors along filament (2). Note that both filaments have the same polarity with the plus ends to the right. (b) Currents $J_{\pm}^{(1,2)}$ of bound motors of the species 'plus' and 'minus' along filaments (1) and (2) as functions of the interaction parameter f . The parameters are as in Fig. 6.3.

value as the current of 'minus' motors, but opposite sign. For $f > f_c$, on the other hand, 'minus' motors are found to move along filament (1) and plus motors move along filament (2), while the currents of 'minus' motors along filament (2) and of 'plus' motors along filament (1) are approximately zero.

6.4 Summary

In this chapter, we have considered systems of motors with attractive interactions. We have argued that binding of motors to filaments is a cooperative process and that experimental results suggest the existence of an attractive interaction between the motors, probably mediated by a deformation of the filament. We have modeled this interaction by taking it to change the detachment rate and the sticking probability at the binding sites next to a bound motor. Increasing the strength of the interaction therefore increases the bound density and, in consequence, an optimal interaction strength is observed, where the current is maximal.

We then studied the case of two species of motors moving into opposite directions and competing for the binding sites of the filament. In this case, binding of a motor to the filament is again enhanced if another motor of the same species is already bound to the filament, but it is inhibited by bound motors of the other species. In this case, spontaneous symmetry breaking is observed for sufficiently high interaction strength and the filament is then populated by only one species of motors. In systems with many filaments, this symmetry breaking results in the formation of separated lanes for traffic of different directionality.

Chapter 7

Conclusions and outlook

In the preceding chapters, we have discussed several transport phenomena related to large-scale movements of processive molecular motors. Observed over sufficiently long times, molecular motors perform peculiar random walks arising from the interplay of directed motion along filaments and diffusion. If such a motor is bound to a filament, it moves along this filament in a directed manner. This directed motion along the filament is interrupted after a certain walking time by the unbinding of the motor from the filament, when the motor–filament binding energy is overcome by thermal fluctuations. The unbound motor can then diffuse freely, until it rebinds to the same or another filament.

To study these random walks and transport processes arising from them, we have introduced a class of models which describe these walks as random walks on a lattice. The filaments correspond to lines on this lattice, and motors at lattice sites belonging to a filament perform biased random walks, while motors at non-filament sites undergo symmetric random walks. Movements from a filament site to a non-filament site and vice versa are governed by the detachment rate and the sticking probability, respectively. All the rates can be determined from experimentally obtained values for the transport properties for bound and unbound motors. In this way, the parameters of our models can be adapted to describe specific motor molecules such as conventional kinesin or myosin V. On the other hand, the model is also suited for studying generic behaviour, since it does not make any specific assumptions about the mechanisms by which the motors work, nor the dynamics on scales smaller than the filament repeat distance.

The second topic we have discussed are motor–motor interactions. These become important, as soon as local motor concentrations are large. Because motors are strongly attracted by the filaments, and motors therefore accumulate on the filaments, this occurs already for relatively small overall motor concentrations. The importance of motor–motor interactions is further increased, if, e.g., bound motors accumulate again close to the end of the filament. Arbitrary motor–motor interactions can easily be included in our lattice models via hopping rates, which depend on whether neighbour sites are occupied or not. The most important interaction of this kind is mutual steric exclusion from binding sites of the filament, for which there is clear experimental evidence both from microtubule decoration experiments, e.g. [77], and motility assays [78]. Mutual exclusion hinders the binding of motors to filaments and reduces the velocity of the motors in regions of high motor density along the filament. We have studied several systems with motors interacting through mutual exclusion in chapters 4 and 5. In addition, there are some indications for cooperative binding of motors to filaments which

corresponds to an attractive interaction between motors mediated by the filaments [107–110]. This case, as well as the case of competitive motor–filament binding of two species of motors, has been discussed in chapter 6.

In detail, we have studied four transport phenomena related to the random walks of molecular motors. First, we discussed *walks of single motors in open compartments* (chapter 3). In open compartments with a single filament, these walks exhibit geometry-dependent anomalous drift behaviour if motors can make arbitrarily large excursions away from the filament, e.g. in the half space and slab geometries. Similar behaviour is obtained in the case of a finite number of parallel filaments. In tube geometries and periodic arrays of filaments, where the size of excursions is restricted, normal drift behaviour results from the interplay of walks along filaments and diffusion. In addition, in most cases diffusion is strongly enhanced by the repeated binding to and unbinding from filaments.

We have then studied *stationary states in closed compartments* (chapter 4), where filaments end in front of a confining wall and motors accumulate at the end of these filaments. In the stationary state, the currents along the filaments are balanced by diffusive currents of unbound motors generated by the concentration gradients which build up due to the accumulation of motors at the filament ends. Because of this accumulation of the motors, which are strongly attracted by the filaments, motor–motor interactions in general and mutual exclusion from binding sites in particular have a strong effect on the cooperative behaviour in these systems. Exclusion results in ‘traffic jams’ of motors at the filament ends and reduces the average current in such systems as soon as the overall motor concentration exceeds an optimal value, for which the current takes on its maximal value. We have determined concentration profiles for two simple geometries, uniaxial arrangements of filaments or a single filament within a closed tube and aster-like arrangements of filaments within a thin disk. Both geometries are accessible to *in vitro* experiments and mimic filament structures in biological cells. The two cases exhibit different concentration profiles. For small overall motor concentrations, the profiles are exponential in the tube geometry and algebraic in aster-like arrangements except for the crowded region close to the filament ends. Increasing the overall motor concentration, the crowded region grows within the tube geometry, while it remains small in asters, where larger overall motor concentrations lead to a flattening of the profile if the motors move inwards, and to the build-up of a concentration maximum in the center of the aster if motors move outwards.

The third transport phenomenon we discussed is the occurrence of *boundary-induced phase transitions* (chapter 5). In open tubes which are coupled to reservoirs of motors at both ends, the stationary state undergoes phase transitions upon varying the motor concentrations in these reservoirs. Exclusion interactions are again crucial. These phase transitions are of the type known from the one-dimensional asymmetric simple exclusion process, but as directed motion is localized to the filaments, there is a larger variety of possible boundary conditions. In some cases, the location of transition lines depends on the model parameters.

Finally, we studied systems of *motors with attractive interactions*, where the binding to the filament is stimulated or inhibited by the presence of other motors already bound to the filament (chapter 6). An attractive interaction between motors enhances the motor–filament attraction, as a motor is more strongly attracted to the filament if another motor is already bound at an adjacent binding site. Therefore, for fixed geometry and overall motor concentration, there is an optimal interaction strength at which the current is maximal, because a more attractive interaction further increases the bound density, so that mutual hindrance decreases the current.

In the case of two species of motors competing for the binding sites on the filament, with mutual attraction between motors of the same species and repulsion between motors of different species, we observed spontaneous symmetry breaking for sufficiently strong interactions. In the state of broken symmetry, the filament is primarily populated by motors of one of the two species. A discontinuous transition with hysteresis is found upon varying the relative concentrations of the two species. In systems with several parallel filaments, lanes of traffic of opposite directionality are formed.

Extensions and open questions

Our present work can be extended into several directions. First, the random walks discussed in chapter 3 could be studied for different geometries. From an experimental point of view, networks and random arrays of filaments are particularly interesting. In a network of filaments, motors should again exhibit effective diffusion with a large diffusion coefficient.

Secondly, in our present work we have assumed that filaments are immobilized. *In vivo*, and also in many *in vitro* experiments, however, filaments undergo Brownian motion and bending fluctuations, polymerize and depolymerize and are even transported along each other by motors [60]. One particularly interesting question in this context is about the formation of structures such as asters in mixtures of filaments and motor complexes moving the filaments. As we have seen, mutual exclusion of motors from binding sites can substantially change the concentration profiles of the motors in aster geometries. One might therefore expect that if these motors are able to move filaments along each other and thus to reorganize the filament pattern, these concentration profiles result in different filament patterns. So far, the influence of exclusion effects on the structure formation has not been explored, neither from the theoretical nor from the experimental point of view.

Third, there are still open questions related to the phase transitions in systems with two competing species of motors. In the future, these transitions should also be studied in different geometries, in particular in closed compartments as in chapter 4. In addition, it should be interesting to study how the observed symmetry breaking might be used for the regulation of transport, e.g. for traffic in lanes of different directionality.

Finally, it might be necessary to refine our models for a detailed comparison with experiments. We have outlined some possible modifications in chapter 4.4.

Experimental realizations

As emphasized before, the transport phenomena discussed here theoretically are accessible to experiments. Compartments with the geometries studied in the previous chapters can be realized in artificial systems, but similar compartments also exist in cells.

A suitable tool to measure concentration profiles is fluorescence microscopy. This technique could be used to determine both the time-dependent concentration profiles in open geometries and the stationary concentration profiles in closed compartments. In the first case, the long-range transport properties of the motors can be extracted from the time-dependence of these profiles.

Fluorescence microscopy has recently been used to determine motor concentration profiles in microtubule asters *in vitro* [87]. In addition, localization of motors has been observed in fungal hyphae, long tube-like protrusions of fungal cells [89]. Both experiments correspond to the case of low overall motor concentration and are in agreement with our theoretical

description. Profiles with higher overall motor concentration may be measured in the same way.

In addition, molecular motors could be used as a model system to study boundary-induced phase transitions. Despite the enormous amount of theoretical work dedicated to this topic, experimental evidence for these transitions is rare (as far as we know, the only direct observation of such a transition has been made for highway traffic [72]).

Likewise, model systems based on molecular motors could also be used to further study motor-motor interactions. One particularly appealing system, which should also be accessible to experiments, consists of immobilized filaments with two types of motors. For this case, our theoretical work predicts a new type of phase transition between two different patterns of motor concentrations.

In summary, the movements of molecular motors over large length scales (many μm), which we have studied theoretically, exhibit several new and interesting transport phenomena that are accessible to experimental research. We hope that this work will stimulate such experiments.

Appendix

Appendix A

Details of the computer simulations

In this appendix, we describe the methods used for the computer simulations of the lattice models. The simulations are based on the usual Monte Carlo algorithm, see, e.g., Ref. [117], but in contrast to the more common case of Monte Carlo simulations in equilibrium statistical mechanics, the Markov chain of states of the system is generated with the *true dynamics* of the system.

Updating

One Monte carlo step corresponds to the basic time scale $\tau = \ell^2/D_{\text{ub}}$. At each Monte Carlo step, each motor particle is moved according to the hopping probabilities defined in chapter 2. Before each movement, it is checked whether the current position of the motor is a filament site or a non-filament site to choose the appropriate set of hopping probabilities. In addition, the state of the adjacent lattice sites is checked when simulating models with attractive motor–motor interactions (chapter 6) to adapt the rates, which, in that case, depend on whether these sites are occupied or free (and by which type of motor these sites are occupied in the case of two motor species). If the target site is occupied by another motor in the case of mutual exclusion, the move is rejected and the motor remains at the site from where it started. In all simulations of interacting motors (chapters 4–6), the updating order is random to prevent correlation effects due to the updating scheme.¹

In the modified lattice model, where bound motors perform a random walk in discrete time with a time scale τ_b , each motor carries its internal 'clock', i.e. it is checked at each step τ for each bound motor whether an integer multiple of τ_b has passed since the last hopping of this motor. Only in that case, the motor is moved according to the hopping probabilities for bound movements. The internal 'clock' of a motor is reset to zero each time the motor attaches to a filament. Zero is also used as initial value for all bound motors. This synchronization is subsequently lost as motors unbind from and bind to filaments.

¹In the case of the one-dimensional asymmetric simple exclusion process, different updating procedures have been studied, see Ref. [118] for a comparison. Which one is used, depends on the kind of system that is modeled. For example parallel update is used in models for traffic flow [71]. In our case, motors hop independently of each other, therefore random update is used.

Compartment boundaries

If the move of a motor crosses one of the the confining walls of the compartment, i.e. a *reflecting boundary*, it is rejected and the motor remains at the lattice site from where it started. The tube geometry, where one filament is oriented along the x-axis (or parallel to it) and the other two Cartesian coordinates are denoted by y_1 and y_2 , is discretized by taking the interior of a tube with radius R to consist of all lattice sites (x, y_1, y_2) with $y_1^2 + y_2^2 \leq R^2$. The tube thus consists of a number N_{ch} of unbound 'channels', i.e. lines of lattice sites parallel to the filament and the cross section ϕ of the tube is given by $\phi = (1 + N_{\text{ch}})\ell^2$. For sufficiently large radii, one has $\phi \approx \pi R^2$, while for small radii, there are corrections due to the underlying lattice.

The *open boundaries* at the left and right end of the open tubes discussed in chapter 5 are implemented by adding two boundary layers at $x = 0$ and $x = L + 1$ with fixed densities. If a motor hops from a lattice site at $x = 1$ or $x = L$, i.e. from within the tube, to a lattice site \vec{y}_{BL} of the boundary layer, the motor leaves the tube with probability $1 - \rho(\vec{y}_{\text{BL}})$, where $\rho(\vec{y}_{\text{BL}})$ is the fixed density at the target site \vec{y}_{BL} in the boundary layer. With probability $\rho(\vec{y}_{\text{BL}})$ the target site is taken to be occupied and the move is rejected.

In addition, motors can enter the tube from the boundary layers. During each Monte Carlo step we thus perform additional updating steps for all lattice site within the boundary layers. Updating a lattice site $\vec{y}_{\text{BL}} = (0, y_1, y_2)$ or $\vec{y}_{\text{BL}} = (L + 1, y_1, y_2)$ of the left or right boundary layer, respectively, consists of two substeps: (i) We first draw a random number ζ which is uniformly distributed over the interval $0 \leq \zeta < 1$. The chosen boundary site is taken to be occupied if $\zeta \leq \rho(\vec{y}_{\text{BL}})$. (ii) If the chosen lattice site is located in the left boundary layer, i.e. $\vec{y}_{\text{BL}} = (0, y_1, y_2)$, and occupied by a motor particle, this motor particle attempts to enter the tube at $(1, y_1, y_2)$ with probability $1/6$ if \vec{y}_{BL} is a non-filament site and with probability α if \vec{y}_{BL} is a filament site. Analogously, if the chosen lattice site is located in the right boundary layer, $\vec{y}_{\text{BL}} = (L + 1, y_1, y_2)$, and occupied by a motor particle, this motor particle attempts to enter the tube at (L, y_1, y_2) with probability $1/6$ or β if \vec{y}_{BL} is a non-filament site or a filament site, respectively. In our simulation, we have, however, taken β to be zero in all cases with open boundaries, so that no particles enter the tube from filament sites within the right boundary layer. Note that these probabilities are chosen in such a way that the parameters of motion at filament and non-filament sites of the boundary layers are the same as within the tube. In all cases, the insertion of a motor is rejected if the target site within the tube is already occupied by a motor.

Random numbers

Finally, we want to mention that the simulations 'consume' enormous amounts of random numbers. For example, the data for Fig. 3.2 have been obtained by simulating 10^9 Monte Carlo steps for 2000 motors, resulting in need for about 10^{12} random numbers. In addition, equipartition of random numbers should be very accurate to study the large-time behaviour, which relies on rare events. This is particularly important in the case of non-interacting motors, where we are effectively using a very large vector of random numbers (the size of which is the number of motors) per Monte Carlo step, as equipartition gets worse with increasing size of a vector [95]. Both requirements make it necessary to use a very good random number generator to prevent artefacts in the long-time behaviour. We used the 'Mersenne Twister', a random number generator with equipartition of accuracy $\sim 10^{-9}$ for vectors of length 623 and an extremely large period of $2^{19937} - 1$ [119].

Appendix B

Theory of random walks

In this appendix, we summarize some methods and results of the theory of random walks [66] which are used in chapter 3 for the analytical solution of the random walks of molecular motors.

B.1 Random walks on homogeneous cubic lattices

In the simplest case, a random walker moves on a d -dimensional cubic lattice and hops to each of the neighbour sites with equal probability $1/(2d)$ per unit time. In discrete time, the master equation for this simple random walk is

$$p(\mathbf{x}, t + 1) = \frac{1}{2d} \sum_{\mathbf{i}} p(\mathbf{x} + \mathbf{i}, t), \quad (\text{B.1})$$

where $p(\mathbf{x}, t)$ is the probability that the motor is at site \mathbf{x} at time t and the summation variable \mathbf{i} runs over the $2d$ nearest neighbours of the origin. A standard method of solution uses Fourier transforms for the spatial coordinates and a (discrete) Laplace transform for the time variable. Defining

$$p(\mathbf{q}, s) = \sum_{t=0}^{\infty} \sum_{\mathbf{x}} \frac{p(\mathbf{x}, t)}{(1+s)^{t+1}} e^{i\mathbf{q}\mathbf{x}} \quad (\text{B.2})$$

and fixing the initial condition by $p(\mathbf{x}, t = 0) = \delta_{\mathbf{x}, \mathbf{0}}$, the master equation yields immediately

$$p(\mathbf{q}, s) = \frac{1}{1 + s - \frac{1}{d} \sum_{i=1}^d \cos q_i} = \frac{1}{1 + s - \mathcal{P}(q)}, \quad (\text{B.3})$$

where the q_i are the components of the vector \mathbf{q} . In the last expression, we have introduced a function $\mathcal{P}(q)$, which is the Fourier transform of the distribution of single steps. In the case of the simple symmetric random walk, $\mathcal{P}(q) = (\sum_{i=1}^d \cos q_i)/d$. The last expression of Eq. (B.3) holds in general, i.e. also for random walks with a bias or steps of different sizes. In these cases, $\mathcal{P}(\mathbf{q})$ has a more complicated form. Corresponding equations are derived in chapter 3 for the random walks of molecular motors.

Inverting the Fourier–Laplace transform yields the full solution. But a lot of useful information can already be obtained from the results for $p(\mathbf{q}, s)$, since (i) expanding the solution in \mathbf{q} generates the Laplace transforms of the moments of the distribution $p(\mathbf{x}, t)$ and (ii) the long-time behaviour of the distribution and its moments can be obtained from the asymptotics of $p(\mathbf{q}, s)$ for small s . This method is generally applicable and is also used in chapter 3 for the

analytical solution of the random walks of molecular motors, where things are more complicated, as the dynamics is different at filament sites and non-filament sites. Let us also mention, that the case of random walks in continuous space and/or time is completely analogous. In that case, the continuous variants of Fourier and Laplace transforms are used.

A generalization of the simple random walk is a continuous-time random walk with a distribution $\psi(\tau_w)$ of waiting times between subsequent steps [120]. In that case, the Laplace transform of the waiting time distribution is needed as well,

$$\psi(s) \equiv \int_{t=0}^{\infty} dt \psi(t) e^{-st}, \quad (\text{B.4})$$

but again an expression for the Fourier–Laplace transform of the probability distribution can be derived, see Ref. [120] and chapter 2 of Ref. [66],

$$p(\mathbf{q}, s) = \frac{1 - \psi(s)}{s[1 - \mathcal{P}(\mathbf{q})\psi(s)]}. \quad (\text{B.5})$$

Expanding to first order in \mathbf{q} and assuming that $\mathcal{P}(\mathbf{q}) \approx 1 + i\mathbf{x}_s\mathbf{q}$ for small \mathbf{q} , i.e., assuming that the random walk is biased and that the mean displacement in a single step is \mathbf{x}_s , the following expression [83] for the average position $\bar{\mathbf{x}}$ of the walker is obtained from Eq. (B.5):

$$\bar{\mathbf{x}}(s) \approx \frac{\mathbf{x}_s\psi(s)}{s[1 - \psi(s)]}. \quad (\text{B.6})$$

The one-dimensional version of this relation is used in chapter 3.3.

B.2 Return to the origin

Let us briefly consider the classical problem of the return to the origin discussed by Polya in 1921 [82] and derive the distribution of return times used in chapter 3.3. We shall restrict us to the simplest case, the symmetric random walk with equally probable nearest-neighbour jumps. Defining $f(\mathbf{x}, t)$ as the probability that the walker is at site \mathbf{x} for *the first time* at time t , the recursion

$$p(\mathbf{x}, t) = \sum_{\tau=1}^t f(\mathbf{x}, \tau)p(\mathbf{0}, t - \tau) + \delta_{t,0}\delta_{\mathbf{x},\mathbf{0}} \quad (\text{B.7})$$

holds, stating that the walker is at site \mathbf{x} at time t , if it had been there at any time $\tau < t$ for the first time and returned there in time $t - \tau$. The term with the Kronecker deltas states that the walker started at $t = 0$ at the origin. Taking the Fourier–Laplace transform of the probability distributions, an expression can be derived for the Laplace transform of $f(\mathbf{0}, t)$, the probability that the walker returns to the origin at time t [66, 82],

$$f(\mathbf{0}, s) = \frac{1}{1+s} - \frac{1}{(1+s)^2 J^{(d)}(s)} \quad \text{with} \quad J^{(d)}(s) = \frac{1}{(2\pi)^d} \int_0^{2\pi} d^d q p(\mathbf{q}, s). \quad (\text{B.8})$$

$p(\mathbf{q}, s)$ is given by Eq. (B.3). As we are finally interested in the return to a filament (chapter 3.3), we use $\mathcal{P}(q) = (1 + \sum_{i=1}^d \cos q_i)/(d+1)$. The integrals $J^{(d)}(s)$ are related to the integrals summarized in appendix B.4 by $J^{(d)}(s) = (d+1) I_1^{(d)}(s + d + sd)$.

In one dimension, we thus obtain

$$J^{(1)}(s) = \frac{1}{2\pi} \int_0^{2\pi} \frac{dq}{s + \frac{1}{2}(1 - \cos q)} = \frac{1}{\sqrt{s + s^2}} \quad (\text{B.9})$$

and hence $f(\mathbf{0}, s) \approx 1 - \sqrt{s}$ for small s . The Tauberian theorem then yields the long-time tail of the return time distribution,

$$f(\mathbf{0}, t) \approx \frac{1}{2\sqrt{\pi}t^{3/2}}. \quad (\text{B.10})$$

Analogously, in the two-dimensional case, the integral is

$$J^{(2)}(s) = \frac{1}{(2\pi)^2} \int_0^{2\pi} \int_0^{2\pi} \frac{dq_1 dq_2}{1 + s - \frac{1}{3}(1 + \cos q_1 + \cos q_2)} = \frac{3\sqrt{m}}{\pi} K(m), \quad (\text{B.11})$$

where $K(m)$ is a complete elliptic integral of the first kind and $m \equiv 4/(2 + 3s)^2$. As $K(m)$ behaves as $K(m) \approx \frac{1}{2} \ln \frac{16}{1-m}$ for m close to one [81], the return time distribution is asymptotically given by $f(\mathbf{0}, s) \approx 1 - 2\pi/(3 \ln s^{-1})$ for small s or

$$f(\mathbf{0}, t) \approx \frac{2\pi}{3t \ln^2 t} \quad (\text{B.12})$$

for large t . Remember that the waiting time distributions $\psi(\tau_w)$ used in chapter 3.3 for the d -dimensional case are given by the return time distribution $f(0, t)$ for $d - 1$ dimensions by identifying the return time t with the waiting time τ_w .

For completeness, let us add two main results of Polya's classical work [82]: (i) The total return probability is given by $f(\mathbf{0}, s = 0) = 1 - 1/J^{(d)}(s = 0)$. It is one and return is certain only if the integral $J^{(d)}(s = 0)$ diverges near $\mathbf{q} = \mathbf{0}$. For small \mathbf{q} , this integral behaves as

$$J^{(d)}(s = 0) \sim \int_0^\infty \frac{q^{d-1} dq}{q^2} \quad (\text{B.13})$$

and thus diverges for $d = 1$ and $d = 2$, but not for $d = 3$, leading to the famous result that the return to the origin is certain in $d = 1$ and $d = 2$, but not in $d = 3$. The return to the filament in the case of random walk of molecular motors, which corresponds to the return to the origin in the $(d - 1)$ -dimensional projection perpendicular to the filament, is thus certain in all realistic situations. This justifies the description of these random walks as consisting of alternating periods of bound movements and diffusion.

(ii) Let us also mention, that even in the cases $d = 1$ and $d = 2$, the mean return time diverges because of the long-time tails of the return time distribution $f(0, t)$. This is the reason for the anomalous drift of the molecular motors in compartments which are open in one or two directions perpendicular to the filament, as it implies that the largest excursions away from the filament dominate (and these are the larger, the longer the motor is observed).

B.3 Tauberian theorems

To invert the Laplace transforms asymptotically, i.e., to obtain the large-time behaviour of a quantity from the behaviour of its Laplace transform for small s , we often use the Tauberian

theorems. These theorems state in general, that if the Laplace transform $f(s)$ of a function $f(t)$ behaves as

$$f(s) \approx \frac{1}{s^\alpha} L(s^{-1}) \quad \text{for small } s, \quad (\text{B.14})$$

where L is a 'slowly varying function', i.e. $L(cx)/L(x) \approx 1$ for large x and every constant c , then $f(t)$ behaves as

$$f(t) \approx \frac{\alpha t^{\alpha-1} L(t) + t^\alpha \frac{\partial}{\partial t} L(t)}{\Gamma(\alpha + 1)} \quad \text{for large } t, \quad (\text{B.15})$$

where, to be precise, one has to assume that $f(t)$ is a monotonous function for large t . The Tauberian theorems hold in the case of continuous Laplace transforms as well as in the case of the discrete ones. For a more detailed discussion, see Refs. [66, 121]. In the solution of the random walks of molecular motors, we use the Tauberian theorems basically as a collection of rules for the asymptotic inversion of Laplace transforms. These rules are summarized in the following:

$$\begin{aligned} s^{-\alpha} &\longrightarrow \frac{t^{\alpha-1}}{\Gamma(\alpha)} \\ s^{-\alpha} \ln s^{-1} &\longrightarrow \frac{t^{\alpha-1}}{\Gamma(\alpha + 1)} (\alpha \ln t + 1) \\ s^{-\alpha} \ln^2 s^{-1} &\longrightarrow \frac{t^{\alpha-1}}{\Gamma(\alpha + 1)} (\alpha \ln^2 t + 2 \ln t). \end{aligned} \quad (\text{B.16})$$

B.4 Integrals for the random walks of molecular motors

The following integrals [81, 122] are necessary for the analytical solution of the random walks of molecular motors:

$$I_1^{(1)}(a) = \frac{1}{2\pi} \int_0^{2\pi} \frac{dq}{a - \cos q} = \frac{1}{\sqrt{a^2 - 1}} \quad (\text{B.17})$$

$$I_2^{(1)}(a) = \frac{1}{2\pi} \int_0^{2\pi} dq \frac{\cos q}{a - \cos q} = a I_1^{(1)}(a) - 1 \quad (\text{B.18})$$

$$I_1^{(2)}(a) = \frac{1}{(2\pi)^2} \int_0^{2\pi} \int_0^{2\pi} \frac{dq_1 dq_2}{a - \cos q_1 - \cos q_2} = \frac{\sqrt{m}}{\pi} K(m) \quad (\text{B.19})$$

$$I_2^{(2)}(a) = \frac{1}{(2\pi)^2} \int_0^{2\pi} \int_0^{2\pi} dq_1 dq_2 \frac{\cos q_1 + \cos q_2}{a - \cos q_1 - \cos q_2} = a I_1^{(2)}(a) - 1. \quad (\text{B.20})$$

In Eq. (B.19), m is defined by $m \equiv 4/a^2$ and $K(m)$ is a complete elliptic integral of the first kind,

$$K(m) = \int_0^{2\pi} \frac{d\phi}{\sqrt{1 - m \sin^2 \phi}}. \quad (\text{B.21})$$

Appendix C

Several motors transporting one cargo

Both *in vivo* and *in vitro*, cargoes are often transported by several motors rather than by a single motor. In this case, complete detachment from the filament is much more unlikely than in the case of a single motor. For example in fast axonal transport, organelles move over distances of centimeters or even meters with velocities comparable to the velocities of a single bound motor [42]. In this appendix, we briefly discuss this case and derive effective detachment rates and velocities which can be used to describe movements of larger motor complexes or cargoes driven by more than one motor using the models introduced in chapter 2.

Effective detachment rate. We consider the scheme shown in Fig. C.1, where ϵ_k is the rate with which one of the motors detaches from the filament, if the cargo is linked to the filament by k motors, and π_k is the rate with which a additional motor binds to the filament. We denote by P_k the probability that k motors are bound to the filament in equilibrium. An effective detachment rate ϵ_{eff} can be defined by $\epsilon_{\text{eff}} \equiv \pi_0 P_0 / (1 - P_0)$. It can be determined by successively expressing all P_k in terms of P_0 . In the general case, we obtain

$$\epsilon_{\text{eff}} = \frac{\epsilon_1}{1 + \sum_{i=1}^{N-1} \prod_{k=1}^i \frac{\pi_k}{\epsilon_{k+1}}} \approx \frac{\epsilon_1 \epsilon_2 \dots \epsilon_N}{\pi_1 \pi_2 \dots \pi_{N-1}}, \quad (\text{C.1})$$

where the last expression holds for small ϵ_k . In the case of two motors, $N = 2$, Eq. (C.1) reduces to $\epsilon_{\text{eff}} = \epsilon_1 / (1 + \pi_1 / \epsilon_2) \approx \epsilon_1 \epsilon_2 / \pi_1$.

The attachment and detachment rates should be proportional to the number of unbound and bound motors, respectively. In addition, a motor pulling at the common cargo may pull

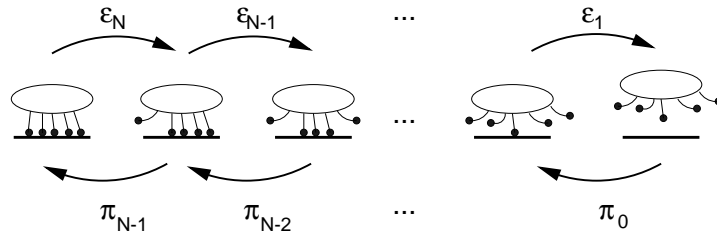


Figure C.1: Binding and unbinding rates for the case of N motors transporting one cargo.

off other motors if the cargo is sufficiently rigid. We thus make the ansatz $\epsilon_k = k\epsilon \exp[\kappa(k-1)]$ for all k , where κ is a measure of the force one motor exerts upon another bound motor, and $\pi_k = (N-k) \pi_{N-1} \times [1 - k/N_s]$ for $k > 0$. Here we assume that the reattachment rates are unaffected by the force exerted by the other motors, as motors can reattach at binding sites, where no stress is present. N_s is the number of binding sites within reach, to which unbound motors can bind (k/N_s is thus the fraction of occupied binding sites). The attachment rate for the first motor, π_0 , is given by the probability of a diffusive encounter with the filament and is therefore independent of the other π_k . It is related to the binding rate $\tilde{\pi}_{\text{ad}}$ of a single motor by $\pi_0 = N\tilde{\pi}_{\text{ad}}$.

For large N_s and $\kappa = 0$, i.e. for the case where attachment and detachment of one motor are completely unaffected by the other motors, Eq. (C.1) can be evaluated analytically and yields

$$\epsilon_{\text{eff}} = \frac{N\epsilon}{\frac{\epsilon}{\pi_{N-1}} \left[\left(1 + \frac{\pi_{N-1}}{\epsilon}\right)^N - 1 \right]} \approx \frac{N\epsilon^N}{\pi_{N-1}^{N-1}}, \quad (\text{C.2})$$

where again the last expression holds in the case of small ϵ . For $\kappa > 0$ and arbitrary N_s , Eq. (C.1) is evaluated numerically.

Average number of bound motors. The average number N_b of motors linking the cargo to the filament (provided the cargo is bound to the filament by at least one motor) is given by

$$N_b \equiv \frac{\sum_{k=1}^N k P_k}{\sum_{k=1}^N P_k} = \frac{1 + \sum_{i=1}^{N-1} (i+1) \prod_{k=1}^i \frac{\pi_k}{\epsilon_{k+1}}}{1 + \sum_{i=1}^{N-1} \prod_{k=1}^i \frac{\pi_k}{\epsilon_{k+1}}}. \quad (\text{C.3})$$

If all ϵ_k are sufficiently small, we obtain $N_b \approx N - \epsilon_N/\pi_{N-1}$, provided $N > 1$. However, if $\kappa > 0$, the condition that all ϵ_k are small cannot be fulfilled for large N . Evaluating Eq. (C.3) numerically, one finds that for $\kappa > 0$, N_b depends approximately logarithmically on the number N of motors.

Velocity. Finally, cargoes transported by many motors are experimentally found to move at approximately the same velocity as single motors [3]. A weak reduction of the velocity due to mutual exclusion has been measured in microtubule gliding assays [78] and bead assays [123] at high surface coverage with kinesin motors. Provided that simple exclusion is the main interaction of the bound motors, the velocity should be given by $v(N) = v_b[1 - N_b(N)/N_s]$. For $\kappa > 0$, i.e. if motors pull upon each other, our approach yields $N_b \sim \ln N$ and thus $v(N) - v_b \sim \ln N$, in agreement with experimental data both from microtubule gliding assays [78] and bead assays [123].

Summarizing, one may use Eq. (C.1) for the effective detachment rate, $N\pi_{\text{ad}}$ for the sticking probability and the velocity v_b of a single motor (neglecting the weak dependence of v on N) to apply the models for random walks of molecular motors to larger motor complexes or cargoes driven by several motors. The number of motors should, however, still be sufficiently small, so that complete detachment from the filament still occurs on experimentally accessible time and length scales.

Appendix D

More about motor traffic in tube-like compartments

In this appendix, we extend the discussion of motor traffic through tube-like compartment and present some more technical results referred to in chapter 5.

D.1 Radial equilibrium for periodic boundary conditions

In the following, we show that Eq. (5.1), the condition for radial equilibrium, holds exactly in the case of periodic boundary conditions using the quantum Hamiltonian formalism [69]. The exact stationary master equation can be written in the form

$$H|\rho\rangle = 0, \quad (\text{D.1})$$

where H is the 'quantum Hamiltonian' of the stochastic process and $|\rho\rangle$ is a vector in a product Hilbert space; each lattice site is represented by a two-state system with the orthogonal vectors $|1\rangle$ for an occupied lattice site ("spin down") and $|0\rangle$ for a vacancy ("spin up"). Because of translational invariance in the direction parallel to the filament, there cannot be any radial currents in our system, and the unbound density is independent of the radial coordinate; thus we can restrict the analysis to the case of one unbound channel. We denote by $|\rho\rangle_{k,b}$ and $|\rho\rangle_{k,ub}$ the state of site k of the bound and unbound channel, respectively.

Using the general recipe given in chapter 2 of Ref. [69] we construct the 'quantum Hamiltonian' H of our system, $H = H_1 + H_2 + H_3$, where H_1 represents the dynamics of the asymmetric exclusion process in the bound channel, H_2 the symmetric exclusion process in the unbound channel and H_3 the coupling of the two channels. Each term can be written as a sum $H_i = \sum_k h_k^{(i)}$ with

$$h_k^{(1)} = v_b \left(n_{k,b} v_{k+1,b} - s_{k,b}^+ s_{k+1,b}^- \right) \quad (\text{D.2})$$

$$h_k^{(2)} = D_{ub} \left(n_{k,ub} v_{k+1,ub} - s_{k,ub}^+ s_{k+1,ub}^- + v_{k,ub} n_{k+1,ub} - s_{k,ub}^- s_{k+1,ub}^+ \right) \quad (\text{D.3})$$

$$h_k^{(3)} = \frac{\epsilon}{6} \left(n_{k,b} v_{k,ub} - s_{k,b}^+ s_{k,ub}^- \right) + \frac{\pi_{ad}}{6} \left(v_{k,b} n_{k,ub} - s_{k,b}^- s_{k,ub}^+ \right). \quad (\text{D.4})$$

$s_{k,b}^-$ is a creation operator for a particle at site k of the bound channel, and $s_{k,b}^+$ is the corresponding annihilation operator. $n_{k,b}$ is the particle number operator at site k of the bound

channel and $v_{k,b} = 1 - n_{k,b}$. Operators for the unbound channel are defined in an analogous manner. The off-diagonal parts of the operators $h_k^{(i)}$ represent hopping of particles, while the diagonal parts are determined by conservation of probability, see chapter 2 of Ref. [69].

We now show that the product measure

$$|\rho\rangle = \bigotimes_k \left([(1 - \rho_b)|0\rangle_{k,b} + \rho_b|1\rangle_{k,b}] \otimes [(1 - \rho_{ub})|0\rangle_{k,ub} + \rho_{ub}|1\rangle_{k,ub}] \right), \quad (\text{D.5})$$

is a stationary state, if Eq. (5.1) holds, i.e. that the radial equilibrium condition implies $H|\rho\rangle = 0$. The product measure $|\rho\rangle$ defines a state where the density is ρ_b at each lattice site of the bound channel and ρ_{ub} at each site of the unbound channel and where spatial correlations vanish.

H_1 and H_2 do not couple the bound and unbound channel, therefore we can consider them separately and refer to the known result, that for the symmetric as well as for the asymmetric exclusion process, the product measure $|\rho\rangle$ is stationary in the case of periodic boundary conditions [124].¹ Hence $H_1|\rho\rangle = 0$ and $H_2|\rho\rangle = 0$.

Concerning H_3 , it is sufficient to consider a single site k in both channels. Doing some steps, we find

$$\left(n_{k,b}v_{k,ub} - s_{k,b}^+s_{k,ub}^- \right) |\rho\rangle_{k,b}|\rho\rangle_{k,ub} = \rho_b(1 - \rho_{ub}) \left(|1\rangle_{k,b}|0\rangle_{k,ub} - |0\rangle_{k,b}|1\rangle_{k,ub} \right) \quad (\text{D.6})$$

and

$$\left(v_{k,b}n_{k,ub} - s_{k,b}^-s_{k,ub}^+ \right) |\rho\rangle_{k,b}|\rho\rangle_{k,ub} = \rho_{ub}(1 - \rho_b) \left(|0\rangle_{k,b}|1\rangle_{k,ub} - |1\rangle_{k,b}|0\rangle_{k,ub} \right) \quad (\text{D.7})$$

for the product measure (D.5). Hence from

$$h_k^{(3)}|\rho\rangle_{k,b}|\rho\rangle_{k,ub} = \left[\frac{\epsilon}{6}\rho_b(1 - \rho_{ub}) - \frac{\pi_{ad}}{6}\rho_{ub}(1 - \rho_b) \right] \left(|1\rangle_{k,b}|0\rangle_{k,ub} - |0\rangle_{k,b}|1\rangle_{k,ub} \right) = 0, \quad (\text{D.8})$$

we obtain Eq. (5.1), which is the condition for radial equilibrium.

D.2 Discrete mean field theory for open boundaries with radial equilibrium

In this section, we derive the phase diagram using a mean field approximation for the discrete two-state model with boundaries satisfying radial equilibrium. The discrete mean field equations are

$$J = v_b\rho_b(x)[1 - \rho_b(x+1)] - D_{ub}[\rho_{ub}(x+1) - \rho_{ub}(x)] \quad (\text{D.9})$$

and

$$v_b\rho_b(x)[1 - \rho_b(x+1)] - v_b\rho_b(x-1)[1 - \rho_b(x)] = \tilde{\pi}\rho_{ub}(x)[1 - \rho_b(x)] - \tilde{\epsilon}\rho_b(x)[1 - \rho_{ub}(x)]. \quad (\text{D.10})$$

¹For a proof using the quantum Hamiltonian formalism, see chapter 7.1.2 of Ref. [69]: In the case of the ASEP in one dimension, for example, one can easily check that $h_k^{(1)}|\rho\rangle = v_b(n_{k,b} - n_{k+1,b})|\rho\rangle$, therefore the summation over k gives zero for periodic boundary conditions.

Introducing the local bound current $j_b(x) = v_b \rho_b(x)[1 - \rho_b(x+1)]$ as a third variable, we write these mean field equations as a recursion,

$$\rho_b(x+1) = 1 - \frac{j_b(x)}{v_b \rho_b(x)} \quad (\text{D.11})$$

$$\rho_{ub}(x+1) = \rho_{ub}(x) + \frac{1}{D_{ub}} j_b(x) - \frac{J}{D_{ub}} \quad (\text{D.12})$$

$$\begin{aligned} j_b(x+1) &= j_b(x) + \tilde{\pi} \rho_{ub}(x+1)[1 - \rho_b(x+1)] - \tilde{\epsilon} \rho_b(x+1)[1 - \rho_{ub}(x+1)] \\ &= j_b(x) + \tilde{\pi} \left[\rho_{ub}(x) + \frac{1}{D_{ub}} j_b(x) - \frac{J}{D_{ub}} \right] \frac{j_b(x)}{v_b \rho_b(x)} \\ &\quad - \tilde{\epsilon} \left[1 - \frac{j_b(x)}{v_b \rho_b(x)} \right] \left[1 - \rho_{ub}(x) - \frac{1}{D_{ub}} j_b(x) + \frac{J}{D_{ub}} \right]. \end{aligned} \quad (\text{D.13})$$

At the boundaries, we have four additional conditions fixing the boundary values of ρ_b and ρ_{ub} . In the particular case, where radial equilibrium is imposed at the boundaries, two conditions fix the bound density to $\rho_{b,\text{in}}$ and $\rho_{b,\text{ex}}$ at the left and right boundary, respectively, while the remaining two conditions are the radial equilibrium conditions, which adapt the unbound density.

We have determined the density profiles numerically by solving the system of non-linear equations (D.9) and (D.10) in the same way as for the closed tube in chapter 4. An alternative method would be to iterate the recursion (D.11)–(D.13).² In the following, we will discuss an analytical way to determine the phase diagram.

Fixed points of the recursion, homogeneous solutions

We first look for fixed points of the recursion relations (D.11)–(D.13). These correspond to solutions with homogeneous density. At the fixed points, Eqs. (D.12) and (D.13) become very simple:

$$j_b = J \quad \text{and} \quad \tilde{\pi} \rho_{ub}(1 - \rho_b) = \tilde{\epsilon} \rho_b(1 - \rho_{ub}), \quad (\text{D.14})$$

i.e., the local bound current is equal to the global current and adsorption equilibrium holds. The remaining condition for ρ_b is the same as the recursion condition for the one-dimensional ASEP [125]. For $J/v_b < 1/4$, it has two solutions,

$$\rho_{b,\pm}(J) = \frac{1}{2} \left[1 \pm \sqrt{1 - 4 \frac{J}{v_b}} \right]. \quad (\text{D.15})$$

Note that $\rho_{b,+} > 1/2$ and $\rho_{b,-} < 1/2$. There are no real solutions for $J/v_b > 1/4$ and there is a single fixed point for $J/v_b = 1/4$.

Stability of the fixed points. We decompose the densities and the current according to $\rho_b = \rho_b^0 + \eta_b$, $\rho_{ub} = \rho_{ub}^0 + \eta_{ub}$ and $j_b = j_b^0 + \eta_j$, where ρ_b^0 , ρ_{ub}^0 and j_b^0 are given by a homogeneous solution, i.e., by one of the fixed points of the recursion. Linearizing the recursion relations (D.11)–(D.13) about this fixed point, we obtain

$$\eta(x+1) = A\eta(x), \quad (\text{D.16})$$

²In the latter case, one has to do the iteration many times to adapt the initial condition for j_b and the parameter J in such a way that one reaches the correct final conditions for ρ_b and ρ_{ub} .

where A is a 3×3 matrix and η is a vector with components η_b , η_{ub} and η_j . We determined numerically the eigenvalues of the matrix $T = A - I$, where I is the identity matrix. As a result, we find that for all chosen sets of parameters, one eigenvalue is positive and one is negative. The sign of the third eigenvalue depends on the value of ρ_b^0 . If $\rho_b^0 < 1/2$ corresponding to a low density fixed point $\rho_{b,-}$, it is positive and if $\rho_b^0 > 1/2$ (high density fixed point), it is negative. For $\rho_b^0 = 1/2$, the third eigenvalue is zero.

However, some of the eigenvectors corresponding to these eigenvalues cannot be realized in our system because of the chosen boundary condition. Our choice of boundary conditions with radial equilibrium implies several conditions for the density profiles. (I) *There are no local maxima or minima of the bound and unbound densities as functions of x except close to the boundaries.* These would disappear through diffusion. This condition holds in general, as long as the particle number is locally conserved in the interior of the tube. Together with our boundary conditions which exclude local maxima or minima close to the boundaries, condition (I) implies that (II) *the unbound density increases (decreases) if the bound density increases (decreases).* It also follows that (III) *the profiles of the bound and unbound density are monotonic functions of x* if radial equilibrium is imposed at the boundaries. Note that conditions (II) and (III) are not necessarily fulfilled if different boundary conditions are chosen.

From the numerical solution for the eigenvectors of $T = A - I$, we find that condition (II) is violated by two eigenvectors. The only eigenvector which satisfies condition (II) is the one corresponding to the eigenvalue which changes sign as a function of ρ_b^0 . We thus recover the situation found for the one-dimensional ASEP [125]: The low density fixed point is unstable and the high density fixed point is stable. In addition, we obtain a *unique* solution for the approach to the fixed point. The inverse of the remaining eigenvalue yields the length scale ξ discussed in chapter 5 and displayed in Fig. 5.4.³

Phase diagram

The phase diagram can now be derived by considering the different cases, where one of the fixed points is approached in the tube. The bulk densities, ρ_b^0 and ρ_{ub}^0 , are then given by that fixed point and related through Eq. (D.14). The current through the tube is $J = j_b = v_b \rho_b^0 (1 - \rho_b^0)$, since the total current is independent of x in the stationary state.

Low density phase. Let us first assume, that ρ_b , ρ_{ub} and j_b are infinitesimally close to the unstable (low density) fixed point at the first lattice sites, $x = 1$. The densities will then stay close to this fixed point for many iterations of the recursion, but finally deviate close to the right boundary. In this case we obtain from the boundary conditions for the left boundary

$$\rho_{b,in} = \rho_b(1), \quad \text{and} \quad J = j_{b,in} = v_b \rho_{b,in} (1 - \rho_{b,in}). \quad (\text{D.17})$$

Obviously such a solution can only exist, if $\rho_{b,in} < 1/2$, as the unstable fixed point has $\rho_{b,-} < 1/2$.

A second condition can be obtained by considering the right boundary: A solution of this type can only exist if the recursion does not reach the stable high density fixed point before reaching the right boundary. We have to distinguish two cases: (a) If $\rho_{b,ex} > \rho_{b,in}$, both the bound and unbound densities are monotonically increasing functions of x . Therefore the

³Remember that the radius enters the two-state approach via the effective unbound diffusion coefficient.

unbound current is negative and the bound current must be larger than J , $j_b(x) \geq J$ for all x . This implies that

$$\rho_b(L) \geq \frac{J/v_b}{1 - \rho_{b,\text{ex}}}. \quad (\text{D.18})$$

A sufficient condition not to reach the high density fixed point is

$$\rho_b(L) < \rho_{b,+}(J). \quad (\text{D.19})$$

With J given by the left boundary, these two inequalities imply $\rho_{b,\text{in}} < 1 - \rho_{b,\text{ex}}$ as a second condition for the range of boundary densities, which allows for a solution governed by the low density fixed point. (b) If $\rho_{b,\text{ex}} < \rho_{b,\text{in}}$, the densities decrease and the high density fixed point cannot be reached. Since $\rho_{b,\text{in}} < 1/2$, we have $1 - \rho_{b,\text{ex}} > 1/2$, and hence the condition $\rho_{b,\text{in}} < 1 - \rho_{b,\text{ex}}$ holds for this case as well.

High density phase. Now we consider the case where we start in the range of attraction of the stable high density fixed point and assume that ρ_b , ρ_{ub} and j_b are infinitesimally close to the stable fixed point at $x = L$. In this case the current is $J = j_b(L) = v_b \rho_{b,\text{ex}}(1 - \rho_{b,\text{ex}})$ and $\rho_{b,\text{ex}} = \rho_b(L)$. The density profiles will relax quickly to the high density fixed point and be nearly constant except close to the left boundary. We can then repeat the above analysis. The first condition is $\rho_{b,\text{ex}} > 1/2$, because at the high density fixed point the bound density is larger than $1/2$.

A sufficient condition for reaching the high density fixed point is

$$\rho_b(1) = 1 - \frac{J}{v_b \rho_{b,\text{in}}} - \frac{D_{\text{ub}}[\rho_{\text{ub}}(1) - \rho_{\text{ub},\text{in}}]}{v_b \rho_{b,\text{in}}} > \rho_{b,-}(J). \quad (\text{D.20})$$

Again two cases have to be distinguished: (a) If $\rho_{\text{ub}}(1) > \rho_{\text{ub},\text{in}}$ the last term is negative, hence $1 - J/(v_b \rho_{b,\text{in}}) > \rho_{b,-}(J)$, which yields the condition $\rho_{b,\text{in}} > 1 - \rho_{b,\text{ex}}$. (b) If on the other hand $\rho_{\text{ub}}(1) < \rho_{\text{ub},\text{in}}$, the profiles are monotonically decreasing and $\rho_b(1) > \rho_{b,-}(J)$ is necessarily fulfilled. Since $\rho_{b,\text{ex}} > 1/2$, the condition $\rho_{b,\text{in}} > 1 - \rho_{b,\text{ex}}$ follows for this case as well.

Maximal current phase. Finally let us consider the remaining case $\rho_{b,\text{in}} > 1/2$ and $\rho_{b,\text{ex}} < 1/2$. In this case the density profiles decrease with x and the bound density crosses at some point from $\rho_b > 1/2$ to $\rho_b < 1/2$. For an infinitely long tube the density variation between a lattice site on the filament and its neighbour will be small, and diffusive contributions to the current vanish except close to the boundaries resulting in the maximal current $J = j_b = v_b/4$ with $\rho_b^0 = 1/2$ and radial equilibrium in the bulk. The profiles are thus governed by the single fixed point with $J = v_b/4$.

Summarizing these results, the phase diagram obtained by the two-state mean field theory for the case of radial equilibrium at the boundaries is the same as the one of the one-dimensional ASEP upon replacing the boundary densities of the ASEP by the corresponding boundary densities on the filament, see Fig. 5.3(a). It exhibits (i) a low density phase for $\rho_{b,\text{in}} < 1/2$ and $\rho_{b,\text{in}} < 1 - \rho_{b,\text{ex}}$, (ii) a high density phase for $\rho_{b,\text{ex}} > 1/2$ and $\rho_{b,\text{in}} > 1 - \rho_{b,\text{ex}}$, and (iii) a maximal current phase for $\rho_{b,\text{in}} > 1/2$ and $\rho_{b,\text{ex}} < 1/2$. This result is in agreement with the dynamical considerations and Monte Carlo simulations presented in chapter 5.

D.3 Diffusive injection and extraction of motor particles: The one-dimensional case

As mentioned in chapter 5, a one-dimensional ASEP coupled to diffusive compartments at both ends exhibits similar behaviour as our tube systems with boundary conditions (C), where the filament ends inside the tube. In this case, the phase diagram can be obtained analytically within a mean field calculation, which we will sketch briefly in the following.

We consider a one-dimensional lattice of length $L+2$ which consists of three compartments. In the first one, $0 \leq x \leq \Delta L$, and the third one, $L - \Delta L \leq x \leq L+1$, transport is diffusive, i.e. particles hop with probability $1/2$ to either direction, in the middle one, transport is driven and particles hop with probability α to the right. For simplicity, we take the probability for backward steps to be zero in the middle compartment and we also assume that particles cannot enter the middle compartment from the right. The densities at the 'external' sites $x = 0$ and $x = L+1$ are fixed to ρ_{in} and ρ_{ex} , respectively.

In the left and right compartments, the density is given by $\rho(x) = \rho_{\text{in}} - 2xJ$ and $\rho(x) = \rho_{\text{ex}} + 2(L+1-x)J$, respectively, where J is the stationary current. The middle compartment can thus be considered as the usual one-dimensional ASEP with effective boundary densities

$$\rho_{\text{in,eff}}(J) = \frac{\rho_{\text{in}}}{2\alpha} - \frac{\Delta L J}{\alpha} \quad \text{and} \quad \rho_{\text{ex,eff}}(J) = \rho_{\text{ex}} + 2\Delta L J. \quad (\text{D.21})$$

Note that the effective boundary densities depend on the current J . The phase diagram can now be determined in a self-consistent way. For example, the transition from a low density to a maximal current phase occurs for $\rho_{\text{in,eff}}(J) = 1/2$ and $\rho_{\text{ex,eff}}(J) < 1/2$. At the transition, we have $J = \alpha/4$, thus the first condition yields $\rho_{\text{in}} = \alpha(1 + \Delta L/2)$ and the second $\rho_{\text{ex}} < \frac{1}{2}(1 - \alpha\Delta L)$. In the same way the location of the transition lines between the maximal current and the high density phase and between the low and high density phases are obtained. Expressions for the current in the high and low density phases are obtained from the self-consistency condition $J = \alpha\rho_{\text{ex,eff}}(J)[1 - \rho_{\text{ex,eff}}(J)]$ and $J = \alpha\rho_{\text{in,eff}}(J)[1 - \rho_{\text{in,eff}}(J)]$, respectively, which lead to quadratic equations for J .

Let us finally consider the maximal current phase. A maximal current phase is found for

$$\rho_{\text{in}} > \alpha\left(1 + \frac{\Delta L}{2}\right) \quad \text{and} \quad \rho_{\text{ex}} < \frac{1}{2}(1 - \alpha\Delta L), \quad (\text{D.22})$$

which can be shifted out of the physical parameter space $0 \leq \rho_{\text{in,ex}} \leq 1$ by tuning the parameters α and ΔL . With the second condition, we recover our estimate of chapter 5 (taking $N_{\text{ch}} = 0$), where we simply compared the currents in the driven and diffusive compartments. The first condition is slightly more restrictive than our simple estimate which would yield $\rho_{\text{in}} > \alpha\Delta L/2$ for this case.

List of symbols

a	abbreviation for $D_{sc}/(2v_b x_{sc})$ used in subsection 5.3.2
A	see Eq. (5.16)
(A)	periodic boundary conditions, see Fig. 5.1
b	abbreviation for $1 + g N_{ch} D_{ub}/D_{sc}$ used in subsection 5.3.2
B	see Eq. (5.16)
(B)	open tube, radial equilibrium at the boundaries, see Fig. 5.1
(C)	open tube, diffusive injection and extraction of motors, see Fig. 5.1
d	spatial dimension
d_f	distance of parallel filaments
D	effective (large-scale) diffusion coefficient in a tube
D_b	(one-dimensional) diffusion coefficient of bound motor
D_{sc}	scale parameter for the scale-dependent diffusion coefficient (5.24)
D_{ub}	diffusion coefficient of unbound motor
f	motor–motor interaction strength, chapter 6
f_c	critical interaction strength
$f(r)$	radial part of the concentration profile in a tube (chapter 4.3)
g	$g \equiv B/A$, see Eq. (5.16)
$I_{1,2}^{(1,2)}$	integrals, see appendix B.4
j_b	local current of bound motors
j_{ub}	local current of unbound motors
J	current through a tube
\bar{J}	spatially averaged current of bound motors in a closed tube
$J_{\text{dif,L}}$	diffusive current in the left diffusive compartment for boundary conditions (C)
$J_{\text{dif,R}}$	diffusive current in the right diffusive compartment for boundary conditions (C)
J_{\pm}	currents of motors of the 'plus' and 'minus' species
k	momentum (Fourier variable) parallel to the filament
ℓ	filament repeat distance and lattice constant
L	length of the tube
L_{diff}	diffusive length scale, $L_{\text{diff}} = \sqrt{D_{ub}t}$
L_F	length of the filament
L_{\perp}	linear size of open compartments (height of a slab or radius of a tube)
L_*	length of crowded region ('traffic jam')
\mathcal{L}	operator governing the linearized dynamics (6.11)

$\mathbf{m} = (m_1, m_2)$	discrete spatial coordinates perpendicular to the filament, $\mathbf{y} = (y_1, y_2) = (m_1\ell, m_2\ell) = \mathbf{m}\ell$
m_b	difference of the bound densities of the motor species 'plus' and 'minus'
m_{ub}	difference of the unbound densities of the motor species 'plus' and 'minus'
$m'_b(f)$	derivative of the absolute value of m_b with respect to f (chapter 6.3.1)
n	discrete spatial coordinate along the filament, $n = x/\ell$
n_{ad}	number of non-filament sites adjacent to a filament site ($n_{ad} = 4$ for a filament in solution, $n_{ad} = 3$ for a filament attached to a wall)
\bar{n}_b	average position of bound motors
N	number of motors
N_{ch}	number of unbound 'channels', $N_{ch} = \phi/\ell^2 - N_f$
N_f	number of filaments
N_{\pm}	numbers of motors of the species 'plus' and 'minus'
$p(x, y_1, y_2, t) = p_{n, m_1, m_2}(t)$	probability that the motor is at lattice site $(x, y_1, y_2) = (n\ell, m_1\ell, m_2\ell)$ at time t
$p_{ub}(x, y_1, y_2, t)$	probability that the motor is unbound at site (x, y_1, y_2) and time t , $p_{ub}(x, y_1, y_2, t) = p(x, y_1, y_2, t) - P(x, t)$
$p_{ub,0}(x, t)$	probability that the motor is unbound in the close vicinity of the filament in the case of the continuum equations, $p_{ub,0}(x, t) = \ell^2 p(x, \mathbf{y} = \mathbf{0}, t)$, see chapter 2.4
$p_1(x, t)$	probability that the motor is at a site next to the filament (chapter 3.2.3)
$P(x, t) = P_n(t)$	probability that the motor is bound to the filament (located along the x axis) at lattice site $x = n\ell$ at time t , $P_n(t) = p_{n,0,0}(t)$
$P_b(t)$	total probability that the motor is bound to the filament
$P_{ub}(t)$	total probability that the motor is not bound to the filament
$\mathbf{q} = (q_1, q_2)$	continuous momentum (Fourier variable) perpendicular to the filament
q_c	momentum cutoff
r	radial coordinate in tube or aster geometries
R	radius of closed tube
R_*	minimal tube radius for which a maximal current phase is found for boundary conditions (C), see chapter 5.4.2
s	Laplace variable corresponding to time
t	time variable
t_*, t_{**}	crossover times
v	average (large-scale) velocity
v_b	velocity of bound motor
v_c	velocity of density fluctuations
v_s	domain wall velocity
$x = n\ell$	spatial coordinate parallel to the filament
\tilde{x}	rescaled and shifted spatial coordinate, $\tilde{x} \equiv (x - x_0)/x_{sc}$ (chapter 5.3.2)
x_s	size of effective 'steps' (chapter 3.3)
x_{sc}	scale parameter for the scale-dependent diffusion coefficient (5.24)
x_*, x_{**}	crossover lengths
$\tilde{x}_*, \tilde{x}_{**}$	rescaled and shifted crossover lengths, defined analogously to \tilde{x}
$\mathbf{y} = (y_1, y_2)$	spatial coordinate perpendicular to the filament

α	probability for a forward step of a bound motor per unit time τ
β	probability for a backward step of a bound motor per unit time τ
γ	dwell probability of a bound motor per unit time τ
ΔL	distance between filament end and tube end for boundary conditions (C)
Δn_b^2	positional variance of bound motors
Δt_b	average walking time before unbinding from the filament
Δt_\perp	time after which the motor movement is geometry-dependent
Δx_b	average walking distance before unbinding from the filament
ϵ	detachment parameter, $\epsilon/(2d)$ is the detachment probability per non-filament neighbour site per unit time τ
$\tilde{\epsilon}$	rescaled detachment probability, $\tilde{\epsilon} = 2\epsilon/3$ in three dimensions, in general $\tilde{\epsilon} = \epsilon(d-1)/d$
η	vector of the density deviations from one of the solutions (chapter 6.3.2)
$\eta_b(x)$	deviation of the bound density from the constant bulk value
η_j	deviation of the bound current from the value corresponding to a homogeneous bound density
$\eta_{ub}(x)$	deviation of the unbound density from the constant bulk value
$\lambda_i(k)$	eigenvalues of the linear operator \mathcal{L}
ξ	localization length or decay length of the density profiles
ξ_0	localization length for the one-dimensional ASEP
π_{ad}	sticking probability for a motor hopping to the filament
$\tilde{\pi}_{ad}$	rescaled sticking probability, $\tilde{\pi}_{ad} = 2\pi_{ad}/3$ in three dimensions, in general $\tilde{\pi}_{ad} = \pi_{ad}(d-1)/d$
$\bar{\rho}(x)$	average motor density (bound and unbound motors)
$\rho_b(x)$	density of motors bound to the filament
$\rho_{b,ex}$	right boundary density on the filament for open tubes
$\rho_{b,in}$	left boundary density on the filament for open tubes
ρ_b^0	constant bulk density on the filament in an open tube
ρ_{ex}	right boundary density for the one-dimensional ASEP
ρ_{in}	left boundary density for the one-dimensional ASEP
ρ^0	constant bulk density for the one-dimensional ASEP
$\rho_{ub}(x, \mathbf{y})$	density of unbound motors
$\rho_{ub,ex}$	density of unbound motors at the right boundary of open tubes
$\rho_{ub,in}$	density of unbound motors at the left boundary of open tubes
ρ_{ub}^0	unbound constant bulk density in open tubes
$\rho_{b,\pm}$	bound densities of motors of the species 'plus' and 'minus'
$\rho_{ub,\pm}$	unbound densities of motors of the species 'plus' and 'minus'
$\rho_{ub,0}$	unbound motor density in the close vicinity of the filament in the case of the continuum equations, $\rho_{ub,0}(x, t) = \ell^2 \rho_{ub}(x, \mathbf{y} = \mathbf{0}, t)$, see chapter 2.4
τ	basic time unit, defined by $\tau = \ell^2/D_{ub}$
τ_b	time unit for bound walks in the modified lattice model, see chapter 2.1.4
τ_{dw}	dwell time
τ_s	step time
τ_w	waiting time between effective steps (chapter 3.3)
ϕ	cross-section of tube, $\phi = N_{ch} + N_f$

ϕ_0	parameter for the ratio of bound to unbound channels in the case of asters, see Eq. (4.46)
$\psi(\tau_w)$	waiting time distribution (chapter 3.3)
$(\omega_{1,i}\omega_{2,j})$	discrete momentum (Fourier variable) perpendicular to the filament in the case of restricted geometries (slab, tube)
ω_c	momentum cutoff

All hopping probabilities are per unit time τ (or per time τ_b in the case of bound movements in the modified lattice model, see chapter 2.1.4). In the case of continuous time, the same symbols denote the corresponding hopping rates. Times and rates are usually measured in units of τ and τ^{-1} , respectively.

Lengths are usually measured in units of the filament repeat distance ℓ . We specify the dependence on ℓ explicitly, when presenting numerical results for specific motors. The discrete variables n and $\mathbf{m} = (m_1, m_2)$ are used in the analytical solution of the lattice model, while we use the continuous analogues x and $\mathbf{y} = (y_1, y_2)$ in most other cases.

In the continuum models, the same symbols as for probabilities in the lattice models, denote the corresponding probability densities. Fourier and Laplace transforms of the probabilities and concentrations are denoted by the same symbols as these quantities themselves and can be distinguished by their arguments.

Bibliography

- [1] H. C. Berg. *Random walks in biology*. Princeton University Press, Princeton/Chichester, second edition, 1993.
- [2] B. Alberts, D. Bray, A. Johnson, J. Lewis, M. Raff, K. Roberts, and P. Walter. *Essential Cell Biology. An Introduction to the Molecular Biology of the Cell*. Garland, New York and London, 1998.
- [3] J. Howard. *Mechanics of Motor Proteins and the Cytoskeleton*. Sinauer Associates, Sunderland (Mass.), 2001.
- [4] R. Brown. A brief account of microscopical observations made in the months of june, july and august 1827, on the particles contained in the pollen of plants; and on the general existence of active molecules in organic and inorganic bodies. *Edinburgh New Phil. J.*, 5:358–371, 1828. A german translation appeared in the same year in *Ann. Physik [II]*, 14:294–313, 1828.
- [5] S. G. Brush. *The kind of motion we call heat*, volume 2, chapter 15: *Brownian movement*, pages 655–701. North-Holland, Amsterdam, 1976.
- [6] A. Einstein. Über die von der molekularkinetischen Theorie der Wärme geforderte Bewegung von in ruhenden Flüssigkeiten suspendierten Teilchen. *Ann. Physik [IV]*, 17:891–921, 1905.
- [7] M. v. Smoluchowsky. Zur kinetischen Theorie der Brownschen Molekularbewegung und der Suspensionen. *Ann. Physik [IV]*, 21:756–780, 1906.
- [8] G. Adam and M. Delbrück. Reduction of dimensionality in biological diffusion processes. In A. Rich and N. Davidson, editors, *Structural Chemistry and Molecular Biology*, pages 198–215. Freeman, San Francisco, 1968.
- [9] P. H. Richter and M. Eigen. Diffusion controlled reaction rates in spheroidal geometry. Application to repressor–operator association and membrane bound enzymes. *Biophys. Chem.*, 2:255–263, 1974.
- [10] O. G. Berg, R. B. Winter, and P. H. von Hippel. Diffusion-driven mechanisms of protein translocation on nucleic acids. 1. Models and theory. *Biochemistry*, 20:6929–6948, 1981.
- [11] M. Guthold, X. Zhu, C. Rivetti, G. Yang, N. H. Thomson, S. Kasas, H. G. Hansma, B. Smith, P. K. Hansma, and C. Bustamante. Direct observation of one-dimensional diffusion and transcription by *Escherichia coli* RNA polymerase. *Biophys. J.*, 77:2284–2294, 1999.

- [12] R. D. Vale, D. R. Soll, and I. R. Gibbons. One-dimensional diffusion of microtubules bound to flagellar dynein. *Cell*, 59:915–925, 1989.
- [13] P. Reimann. Brownian motors: Noisy transport far from equilibrium. *Phys. Rep.*, 361:57–265, 2002.
- [14] J. Rousselet, L. Salome, A. Ajdari, and J. Prost. Directional motion of brownian particles induced by a periodic asymmetric potential. *Nature*, 370:446–448, 1994.
- [15] Y. Okada and N. Hirokawa. A processive single-headed motor: Kinesin superfamily protein KIF1A. *Science*, 283:1152–1157, 1999.
- [16] M. Tomishige, D. R. Klopfenstein, and R. D. Vale. Conversion of Unc104/KIF1A kinesin into a processive motor after dimerization. *Science*, 297:2263–2267, 2002.
- [17] J. A. Spudich. How molecular motors work. *Nature*, 372:515–518, 1994.
- [18] R. D. Vale and R. A. Milligan. The way things move: Looking under the hood of molecular motor proteins. *Science*, 288:88–95, 2000.
- [19] G. Woehlke and M. Schliwa. Walking on two heads: The many talents of kinesin. *Nature Reviews Molec. Cell Biol.*, 1:50–59, 2000.
- [20] D. D. Hackney. Evidence for alternating head catalysis by kinesin during microtubule-stimulated ATP hydrolysis. *Proc. Natl. Acad. Sci. USA*, 91:6865–6869, 1994.
- [21] W. O. Hancock and J. Howard. Processivity of the motor protein kinesin requires two heads. *J. Cell Biol.*, 140:1395–1405, 1998.
- [22] W. O. Hancock and J. Howard. Kinesin’s processivity results from mechanical and chemical coordination between the ATP hydrolysis cycles of the two motor domains. *Proc. Natl. Acad. Sci. USA*, 96:13147–13152, 1999.
- [23] W. Hua, J. Chung, and J. Gelles. Distinguishing inchworm and hand-over-hand processive movement by neck rotation measurements. *Science*, 295:844–848, 2002.
- [24] A. D. Mehta, M. Rief, J. A. Spudich, D. A. Smith, and R. M. Simmons. Single-molecule biomechanics with optical methods. *Science*, 283:1689–1695, 2000.
- [25] J. Howard, A. J. Hudspeth, and R. D. Vale. Movement of microtubules by single kinesin molecules. *Nature*, 342:154–158, 1989.
- [26] S. M. Block, L. S. B. Goldstein, and B. J. Schnapp. Bead movement by single kinesin molecules studied with optical tweezers. *Nature*, 348:348–352, 1990.
- [27] K. Svoboda, Ch. F. Schmidt, B. J. Schnapp, and S. M. Block. Direct observation of kinesin stepping by optical trapping interferometry. *Nature*, 365:721–727, 1993.
- [28] R. D. Vale, T. Funatsu, D. W. Pierce, L. Romberg, Y. Harada, and T. Yanagida. Direct observation of single kinesin molecules moving along microtubules. *Nature*, 380:451–453, 1996.

- [29] M. J. Schnitzer and S. M. Block. Kinesin hydrolyses one ATP per 8-nm step. *Nature*, 388:386–390, 1997.
- [30] K. Visscher, M. J. Schnitzer, and S. M. Block. Single kinesin molecules studied with a molecular force clamp. *Nature*, 400:184–189, 1999.
- [31] A. D. Mehta, R. S. Rock, M. Rief, J. A. Spudich, M. S. Mooseker, and R. E. Cheney. Myosin-V is a processive actin-based motor. *Nature*, 400:590–593, 1999.
- [32] M. Rief, R. S. Rock, A. D. Mehta, M. S. Mooseker, R. E. Cheney, and J. A. Spudich. Myosin-V stepping kinetics: A molecular model for processivity. *Proc. Natl. Acad. Sci. USA*, 97:9482–9486, 2000.
- [33] S. J. King and T. A. Schroer. Dynactin increases the processivity of the cytoplasmic dynein motor. *Nature Cell Biol.*, 2:20–24, 2000.
- [34] Z. Wang and M. P. Sheetz. The C-terminus of tubulin increases cytoplasmic dynein and kinesin processivity. *Biophys. J.*, 78:1955–1964, 2000.
- [35] E. Hirakawa, H. Higuchi, and Y. Y. Toyoshima. Processive movement of single 22S dynein molecules occurs only at low ATP concentrations. *Proc. Natl. Acad. Sci. USA*, 97:2533–2537, 2000.
- [36] J. R. Dennis, J. Howard, and V. Vogel. Molecular shuttles: Directed motion of microtubules along nanoscale kinesin tracks. *Nanotechnology*, 10:232–236, 1999.
- [37] H. Hess, J. Clemmens, D. Qin, J. Howard, and V. Vogel. Light-controlled molecular shuttles made from motor proteins carrying cargo on engineered surfaces. *Nano Lett.*, 1:235–239, 2001.
- [38] L. Limberis and R. J. Stewart. Toward kinesin-powered microdevices. *Nanotechnology*, 11:47–51, 2000.
- [39] R. Stracke, K. J. Böhm, J. Burghold, H.-J. Schacht, and E. Unger. Physical and technical parameters determining the functioning of a kinesin-based cell-free motor system. *Nanotechnology*, 11:52–56, 2000.
- [40] K. J. Böhm, R. Stracke, P. Mühlig, and E. Unger. Motor protein-driven unidirectional transport of micrometer-sized cargoes across isopolar microtubule arrays. *Nanotechnology*, 12:238–244, 2001.
- [41] R. Lipowsky. Movements of molecular motors. In V. Sayakanit, L. Matsson, and H. Frauenfelder, editors, *Biological physics 2000*, pages 41–56. World Scientific, Singapore, 2001.
- [42] L. S. B. Goldstein and Z. Yang. Microtubule-based transport systems in neurons: The roles of kinesins and dyneins. *Annu. Rev. Neurosci.*, 23:39–71, 2000.
- [43] N. J. Córdoba, B. Ermentrout, and G. F. Oster. Dynamics of single-motor molecules: The thermal ratchet model. *Proc. Natl. Acad. Sci. USA*, 89:339–343, 1992.
- [44] S. Leibler and D. A. Huse. Porters versus rowers: A unified stochastic model of motor proteins. *J. Cell Biol.*, 121:1357–1368, 1993.

- [45] J. Prost, J.-F. Chauwin, L. Peliti, and A. Ajdari. Asymmetric pumping of particles. *Phys. Rev. Lett.*, 72:2652–2655, 1994.
- [46] R. D. Astumian. Thermodynamics and kinetics of a Brownian motor. *Science*, 276:917–922, 1997.
- [47] F. Jülicher, A. Ajdari, and J. Prost. Modeling molecular motors. *Rev. Mod. Phys.*, 69:1269–1281, 1997.
- [48] M. E. Fisher and A. B. Kolomeisky. The force exerted by a molecular motor. *Proc. Natl. Acad. Sci. USA*, 96:6597–6602, 1999.
- [49] R. Lipowsky and Th. Harms. Molecular motors and nonuniform ratchets. *Eur. Biophys. J.*, 29:542–548, 2000.
- [50] A. Parmeggiani, F. Jülicher, L. Peliti, and J. Prost. Detachment of molecular motors under tangential loading. *Europhys. Lett.*, 56:603–609, 2001.
- [51] M. E. Fisher and A. B. Kolomeisky. Simple mechanochemistry describes the dynamics of kinesin molecules. *Proc. Natl. Acad. Sci. USA*, 98:7748–7753, 2001.
- [52] G. Lattanzi and A. Maritan. Force dependent transition rates in chemical kinetics models for motor proteins. *J. Chem. Phys.*, 117:10339–10349, 2002.
- [53] R. Lipowsky. Universal aspects of the chemomechanical coupling for molecular motors. *Phys. Rev. Lett.*, 85:4401–4405, 2000.
- [54] R. Lipowsky and N. Jaster. Molecular motor cycles: From ratchets to networks. *J. Stat. Phys.*, 110:1141–1167, 2003.
- [55] A. Ajdari. Transport by active filaments. *Europhys. Lett.*, 31:69–74, 1995.
- [56] R. Lipowsky, S. Klumpp, and Th. M. Nieuwenhuizen. Random walks of cytoskeletal motors in open and closed compartments. *Phys. Rev. Lett.*, 87:108101.1–4, 2001.
- [57] Th. M. Nieuwenhuizen, S. Klumpp, and R. Lipowsky. Walks of molecular motors in two and three dimensions. *Europhys. Lett.*, 58:468–474, 2002.
- [58] S. Klumpp and R. Lipowsky. Traffic of molecular motors through tube-like compartments. Submitted to *J. Stat. Phys.*, 2003.
- [59] R. Urrutia, M. A. McNiven, J. P. Albanesi, D. B. Murphy, and B. Kachar. Purified kinesin promotes vesicle motility and induces active sliding between microtubules *in vitro*. *Proc. Natl. Acad. Sci. USA*, 88:6701–6705, 1991.
- [60] F. Nédélec, T. Surrey, A. C. Maggs, and S. Leibler. Self-organization of microtubules and motors. *Nature*, 389:305–308, 1997.
- [61] F. Nédélec. *Auto-organisation d'un mélange de microtubules et de moteurs*. PhD thesis, Université Paris XI, 1998.
- [62] T. Surrey, F. Nédélec, S. Leibler, and E. Karsenti. Physical properties determining self-organization of motors and microtubules. *Science*, 292:1167–1171, 2001.

- [63] H. Y. Lee and M. Kardar. Macroscopic equations for pattern formation in mixtures of microtubules and molecular motors. *Phys. Rev. E*, 64:056113.1–8, 2001.
- [64] K. S. Thorn, J. A. Ubersax, and R. D. Vale. Engineering the processive run length of the kinesin motor. *J. Cell Biol.*, 151:1093–1100, 2000.
- [65] K. Luby-Phelps. Cytoarchitecture and physical properties of cytoplasm: volume, viscosity, diffusion, intracellular surface area. *Int. Rev. Cytol. – Survey Cell Biol.*, 192:189–221, 2000.
- [66] G. H. Weiss. *Aspects and Applications of the Random Walk*. North-Holland, Amsterdam, 1994.
- [67] J. W. Haus and K. W. Kehr. Diffusion in regular and disordered lattices. *Phys. Rep.*, 150:263–406, 1986.
- [68] B. Schmittmann and R. K. P. Zia. Statistical mechanics of driven diffusive systems. In C. Domb and J. L. Lebowitz, editors, *Phase transitions and critical phenomena*, volume 17. Academic Press, London/San Diego, 1995.
- [69] G. M. Schütz. Exactly solvable models for many-body systems far from equilibrium. In C. Domb and J. L. Lebowitz, editors, *Phase Transitions and Critical Phenomena*, volume 19, pages 1–251. Academic Press, San Diego, 2001.
- [70] S. Katz, J. L. Lebowitz, and H. Spohn. Nonequilibrium steady states of stochastic lattice gas models of fast ionic conductors. *J. Stat. Phys.*, 34:497–537, 1984.
- [71] K. Nagel and M. Schreckenberg. A cellular automaton model for freeway traffic. *J. Phys. I France*, 2:2221–2229, 1992.
- [72] V. Popkov, L. Santen, A. Schadschneider, and G. M. Schütz. Empirical evidence for a boundary-induced nonequilibrium phase transition. *J. Phys. A: Math. Gen.*, 34:L45–L52, 2001.
- [73] R. K. P. Zia, L. B. Shaw, B. Schmittmann, and R. J. Aastalos. Contrasts between equilibrium and non-equilibrium steady states: Computer aided discoveries in simple lattice gases. *Computer Physics Communications*, 127:23–31, 2000.
- [74] J. Krug. Boundary-induced phase transitions in driven diffusive systems. *Phys. Rev. Lett.*, 67:1882–1885, 1991.
- [75] A. B. Kolomeisky, G. M. Schütz, E. B. Kolomeisky, and J. P. Straley. Phase diagram of one-dimensional driven lattice gases with open boundaries. *J. Phys. A: Math. Gen.*, 31:6911–6919, 1998.
- [76] B. Derrida and M. R. Evans. The asymmetric exclusion model: Exact results through a matrix approach. In V. Privman, editor, *Nonequilibrium Statistical Mechanics in One Dimension*, pages 277–304. Cambridge University Press, Cambridge, 1997.
- [77] Y.-H. Song and E. Mandelkow. Recombinant kinesin motor domain binds to β -tubulin and decorates microtubules with a B surface lattice. *Proc. Natl. Acad. Sci. USA*, 90:1671–1675, 1993.

- [78] K. J. Böhm, R. Stracke, and E. Unger. Speeding up kinesin-driven microtubule gliding *in vitro* by variation of cofactor composition and physicochemical parameters. *Cell Biol. Int.*, 24:335–341, 2000.
- [79] H. Gau, S. Herminghaus, P. Lenz, and R. Lipowsky. Liquid morphologies on structured surfaces: From microchannels to microchips. *Science*, 283:46–49, 1999.
- [80] Th. M. Nieuwenhuizen, S. Klumpp, and R. Lipowsky. In preparation.
- [81] M. Abramowitz and I. Stegun, editors. *Pocketbook of Mathematical Functions*. Harri Deutsch, Thun and Frankfurt/Main, 1984.
- [82] G. Polya. Über eine Aufgabe der Wahrscheinlichkeitsrechnung betreffend die Irrfahrt im Straßennetz. *Math. Ann.*, 84:149–160, 1921. See also chapter 4 of Ref. [66].
- [83] M. F. Shlesinger. Asymptotic solutions of continuous-time random walks. *J. Stat. Phys.*, 10:421–434, 1974.
- [84] J. Crank. *The Mathematics of Diffusion*. Oxford University Press, Oxford, 2nd edition, 1975.
- [85] G. H. Weiss. The two-state random walk. *J. Stat. Phys.*, 15:157–165, 1976.
- [86] C. Van den Broeck. Taylor dispersion revisited. *Physica A*, 168:677–696, 1990.
- [87] F. Nédélec, T. Surrey, and A. C. Maggs. Dynamic concentration of motors in microtubule arrays. *Phys. Rev. Lett.*, 86:3192–3195, 2001.
- [88] B. Mulder. Private communication.
- [89] S. Seiler, J. Kirchner, Ch. Horn, A. Kallipolitou, G. Woehlke, and M. Schliwa. Cargo binding and regulatory sites in the tail of fungal conventional kinesin. *Nature Cell Biol.*, 2:333–338, 2000.
- [90] K. J. Verhey, D. L. Lizotte, T. Abramson, L. Barenboim, B. J. Schnapp, and T. A. Rapoport. Light-chain dependent regulation of kinesin’s interaction with microtubules. *J. Cell Biol.*, 143:1053–1066, 1998.
- [91] D. L. Coy, W. O. Hancock, M. Wagenbach, and J. Howard. Kinesin’s tail domain is an inhibitory regulator of the motor domain. *Nature Cell Biol.*, 1:288–292, 1999.
- [92] A. B. Dahlström, K. K. Pfister, and S. T. Brady. The axonal transport motor ‘kinesin’ is bound to anterogradely transported organelles: Quantitative cytofluorimetric studies of fast axonal transport in the rat. *Acta Physiol. Scand.*, 141:469–476, 1991.
- [93] N. Hirokawa, R. Sato-Yoshitake, T. Yoshida, and T. Kawashima. Brain dynein (MAP1C) localizes on both anterogradely and retrogradely transported membranous organelles *in vivo*. *J. Cell Biol.*, 111:1027–1037, 1990.
- [94] N. Hirokawa, R. Sato-Yoshitake, N. Kobayashi, K. K. Pfister, G. S. Bloom, and S. T. Brady. Kinesin associates with anterogradely transported membranous organelles *in vivo*. *J. Cell Biol.*, 114:295–302, 1991.

- [95] W. H. Press, S. A. Teukolsky, W. T. Vetterling, and B. P. Flannery. *Numerical Recipes in C*. Cambridge University Press, Cambridge, second edition, 1992.
- [96] A. A. Hyman and E. Karsenti. Morphogenetic properties of microtubules and mitotic spindle assembly. *Cell*, 84:401–410, 1996.
- [97] A. B. Verkhovskiy, T. M. Svitkina, and G. G. Borisy. Polarity sorting of actin filaments in cytochalasin-treated fibroblasts. *J. Cell Sci.*, 110:1693–1704, 1997.
- [98] D. Smith, J. Käs *et al.* (unpublished).
- [99] C. T. MacDonald, J. H. Gibbs, and A. C. Pipkin. Kinetics of biopolymerization on nucleic acid templates. *Biopolymers*, 6:1–25, 1968.
- [100] C. T. MacDonald and J. H. Gibbs. Concerning the kinetics of polypeptide synthesis on polyribosomes. *Biopolymers*, 7:707–725, 1969.
- [101] H. M. Dintzis. Assembly of the peptide chains of hemoglobin. *Proc. Natl. Acad. Sci. USA*, 47:247–261, 1961.
- [102] M. A. Naughton and H. M. Dintzis. Sequential biosynthesis of the peptide chains of hemoglobin. *Proc. Natl. Acad. Sci. USA*, 48:1822–1830, 1962.
- [103] R. M. Winslow and V. M. Ingram. Peptide chain synthesis of human hemoglobin A and A₂*. *J. Biol. Chem.*, 241:1144–1149, 1966.
- [104] G. Schütz and E. Domany. Phase transitions in an exactly soluble one-dimensional exclusion process. *J. Stat. Phys.*, 72:277–296, 1993.
- [105] B. Derrida, M. R. Evans, V. Hakim, and V. Pasquier. Exact solution of a 1D asymmetric exclusion model using a matrix formulation. *J. Phys. A: Math. Gen.*, 26:1493–1517, 1993.
- [106] H. van Beijeren, R. Kutner, and H. Spohn. Excess noise for driven diffusive systems. *Phys. Rev. Lett.*, 54:2026–2029, 1985.
- [107] A. Vilfan, E. Frey, F. Schwabl, M. Thormählen, Y.-H. Song, and E. Mandelkow. Dynamics and cooperativity of microtubule decoration by the motor protein kinesin. *J. Mol. Biol.*, 312:1011–1026, 2001.
- [108] D. T. Woodrum, S. A. Rich, and T. D. Pollard. Evidence for biased bidirectional polymerization of actin filaments using heavy meromyosin prepared by an improved method. *J. Cell Biol.*, 67:231–237, 1975.
- [109] A. Orlova and E. H. Egelman. Cooperative rigor binding of myosin to actin is a function of F-actin structure. *J. Mol. Biol.*, 265:469–474, 1997.
- [110] E. Muto. Is microtubule an active participant in the mechanism of motility? *Biophys. J. (Ann. Meeting Abstr.)*, 80:513a, 2001.

I am grateful to Prof. M. Schliwa for providing another meeting abstract of the same author and with the same title which contains some additional information.

- [111] A. Lockhard, I. M.-T. C. Crevel, and R. A. Cross. Kinesin and *ncd* bind through a single head to microtubules and compete for a shared MT binding site. *J. Mol. Biol.*, 249:763–771, 1995.
- [112] B. Schmittmann, K. Hwang, and R. K. P. Zia. Onset of spatial structures in biased diffusion of two species. *Europhys. Lett.*, 19:19–25, 1992.
- [113] G. Korniss, B. Schmittmann, and R. K. P. Zia. Long-range order in a quasi one-dimensional non-equilibrium three-state lattice gas. *Europhys. Lett.*, 45:431–436, 1999.
- [114] M. R. Evans, D. P. Forster, C. Godrèche, and D. Mukamel. Spontaneous symmetry breaking in a one dimensional driven diffusive system. *Phys. Rev. Lett.*, 74:208–211, 1995.
- [115] K. Binder and D. W. Heermann. *Monte Carlo Simulation in Statistical Physics*. Springer, Berlin, Heidelberg, second edition, 1992.
- [116] G. Nicolis. *Introduction to Nonlinear Science*. Cambridge University Press, Cambridge, 1995.
- [117] D. W. Heermann. *Computer Simulation Methods in Theoretical Physics*. Springer, Berlin, Heidelberg, second edition, 1990.
- [118] N. Rajewsky, L. Santen, A. Schadschneider, and M. Schreckenberg. The asymmetric exclusion process: Comparison of update procedures. *J. Stat. Phys.*, 92:151–194, 1998.
- [119] M. Matsumoto and T. Nishimura. Mersenne twister: A 623-dimensionally equidistributed uniform pseudorandom number generator. *ACM Transactions on Modeling and Computer Simulation*, 8:3–30, 1998. The source code is available at <http://www.math.keio.ac.jp/~matumoto/emt.html>.
- [120] E. W. Montroll and G. H. Weiss. Random walks on lattices. II. *J. Math. Phys.*, 6:167–181, 1965.
- [121] W. Feller. *An Introduction to Probability Theory and its Applications*, volume 2. Wiley, New York, second edition, 1971.
- [122] I. S. Gradshteyn and I. M. Ryzhik. *Table of Integrals, Series, and Products*. Academic Press, San Diego, 5th edition, 1994.
- [123] J. Beeg. Private communication.
- [124] F. Spitzer. Interaction of Markov processes. *Adv. Math.*, 5:246–290, 1970.
- [125] B. Derrida, E. Domany, and D. Mukamel. An exact solution of a one-dimensional asymmetric exclusion model with open boundaries. *J. Stat. Phys.*, 69:667–687, 1992.

Acknowledgments

Zum Schluß möchte ich allen meinen Dank aussprechen, die mich unterstützt und in irgendeiner Form zu dieser Arbeit beigetragen haben.

An erster Stelle gilt mein Dank Prof. Reinhard Lipowsky für die Betreuung und Unterstützung sowie wertvolle Diskussionen und Anregungen, welche der Arbeit wichtige Impulse gegeben haben.

Theo Nieuwenhuizen danke ich für die fruchtbare und nette Zusammenarbeit während seiner Besuche in Golm, bei der ich von seiner Erfahrung mit Random Walks profitieren konnte.

Schließlich möchte ich allen Kollegen am Max-Planck-Institut für Kolloid- und Grenzflächenforschung in Golm danken, die das Institut zu einem sowohl produktiven als auch angenehmen Platz machen, an dem zu arbeiten ich sehr genossen habe. Ganz besonders bedanken möchte ich mich bei Jan Kierfeld für hilfreiche Diskussionen und bei Nicole Jaster für das kritische Lesen der Arbeit. Außerdem gilt mein besonderer Dank Martin Brinkmann, Antonio Valencia, Ulrich Schwarz, Alberto Imparato, Ilka Bischofs und Thorsten Erdmann. Julian Shillcock hat geduldig alle meine sprachlichen Fragen geklärt und Teile der Arbeit korrigiert; ebenfalls vielen Dank. Vielen Dank schließlich auch an Thomas Baumann und die anderen Mitglieder des IT-Teams des Instituts, die dafür gesorgt haben, daß die Rechner immer zuverlässig gearbeitet haben.

Zuletzt möchte ich noch meiner Freundin Irene danken für ihren Rat und ihre Unterstützung und für die schöne Zeit, die wir in Berlin hatten und haben.